May 2022

Simulating the Common Envelope Phase Using Moving-Mesh Hydrodynamics

Logan James Prust
University of Wisconsin-Milwaukee

Recommended Citation

Prust, Logan James, "Simulating the Common Envelope Phase Using Moving-Mesh Hydrodynamics" (2022). *Theses and Dissertations*. 2932.
https://dc.uwm.edu/etd/2932

SIMULATING THE COMMON ENVELOPE PHASE USING MOVING-MESH HYDRODYNAMICS

by

Logan James Prust

A Dissertation Submitted in
Partial Fulfillment of the
Requirements for the Degree of

Doctor of Philosophy
in Physics

at

The University of Wisconsin-Milwaukee
May 2022

ABSTRACT

SIMULATING THE COMMON ENVELOPE PHASE USING MOVING-MESH HYDRODYNAMICS

by

Logan James Prust

The University of Wisconsin-Milwaukee, 2022
Under the Supervision of Professor Philip Chang, PhD

Common envelope evolution (CEE) is a phase in the evolution of a binary system where a giant star and a smaller companion share a gaseous envelope, and is responsible for the formation of many systems of astrophysical interest. Despite its importance, CEE is not well understood due to the diverse physics involved. Astronomers have roughly modeled CEE using conserved quantities such as energy, but progress has been limited by uncertainties in the contributions of various energy sources. Thus, 3-D numerical simulations must be brought to bear. Here two methodologies are commonly employed, each of which comes with its own set of advantages: smoothed-particle hydrodynamics and Eulerian grid codes. A hybrid of these methods known as the moving-mesh code has been developed in an attempt to capture the best characteristics of each. We use the moving-mesh solver MANGA, which has recently been improved with the inclusion of physics modules relevant to CEE.

We begin this work with an introduction to CEE in Chapter 1. We go through a step-by-step description of its four stages and summarize observations of transients that are thought to result from binary interactions. We then present an overview of simulation techniques in Chapter 2, showing how aspects of smoothed-particle hydrodynamics and Eulerian methods are implemented into moving-mesh schemes. We begin our numerical studies of CEE using MANGA in Chapter 3 and show that the ejection of the envelope is

aided by the inclusion of hydrogen recombination and tidal forces.

CEE simulations to date have neglected hydrodynamic interactions at the surface of the companion. As such, we discuss our development of moving boundary conditions in Chapter 4 and show how they can be used to model the companion object. We show that the orbital eccentricity is affected by the size of the companion through hydrodynamic torques. Finally, we describe our implementation of magnetohydrodynamics in Chapter 5. We find rapid amplification of a toroidal magnetic field at the onset of CEE, which is thought to assist in the formation of nebulae.

Publications Connected to this Dissertation

The work presented in **Chapters 2, 3, and 4** has been published in the following papers:

> Prust, L. (2020). *Moving and Reactive Boundary Conditions in Moving-Mesh Hydrodynamics*. Monthly Notices of the Royal Astronomical Society.
>
> → https://doi.org/10.1093/mnras/staa1031
>
> → https://arxiv.org/abs/2002.04287
>
> Prust, L., & Chang, P. (2019). *Common Envelope Evolution on a Moving Mesh*. Monthly Notices of the Royal Astronomical Society.
>
> → https://doi.org/10.1093/mnras/stz1219
>
> → https://arxiv.org/abs/1904.09256

At the time of finishing and submitting this dissertation, the work in **Chapters 3, 4, and 5** was being prepared in multiple manuscripts to submit for publication.

TABLE OF CONTENTS

LIST OF FIGURES

LIST OF TABLES

LIST OF ABBREVIATIONS

ALE	arbitrary Lagrangian-Eulerian
AMR	adaptive mesh refinement
BH	black hole
BPS	binary population synthesis
CEE	common envelope evolution
CFL	Courant-Friedrichs-Levy
ChaNGa	Charm N-body GrAvity solver
CM	center of mass
CT	constrained transport
EOS	equation of state
GLM	generalized Lagrange multiplier
GRB	gamma-ray burst
GR	general relativity
GRHD	general relativistic hydrodynamics
GW	gravitational wave
HMXB	high-mass X-ray binary
HPC	high-performance computing
ILOT	intermediate-luminosity optical transient
IMF	initial mass function
ISM	interstellar medium
LIGO	Laser Interferometer Gravitational-Wave Observatory
LISA	Laser Interferometer Space Antenna
LMXB	low-mass X-ray binary
$M_\odot$	solar mass

MANGA	moving-mesh ChaNGa
MESA	Modules for Experiments in Stellar Astrophysics
MHD	magnetohydrodynamics
MM	moving-mesh
MSP	millisecond pulsar
NS	neutron star
PCEB	post-common envelope binary
PNe	planetary nebulae
pWD	pseudo-white dwarf
$R_\odot$	solar radius
RG	red giant
RHD	radiation hydrodynamics
RLOF	Roche lobe overflow
SMBH	supermassive black hole
SMT	stable mass transfer
SN	supernovae
SPH	smoothed-particle hydrodynamics
TOV	Tolman-Oppenheimer-Volkoff
TVD	total variation diminishing
TZlO	Thorne-Zytkow-like object
UMT	unstable mass transfer
UV	ultraviolet
WD	white dwarf
ZAMS	zero-age main sequence

ACKNOWLEDGMENTS

I am grateful to my family, who have fostered my curiosity from a young age and have supported me throughout my academic career. I am also grateful for the many graduate students, postdocs, and faculty at UWM who have made my experience living and working in Milwaukee a positive one.

My PhD advisor, Philip Chang, has been very helpful in setting me on the path to success in astrophysics and in guiding me to projects which matched my interests and skill set. The rest of my PhD committee has also been helpful in keeping me on the right track and in challenging me academically: Daniel Agterberg, John Friedman, David Kaplan, and Sarah Vigeland. I have also received valuable support from Heidi Matera, Tonia Klein, and others within the department.

I thank the authors of several plots which I have reprinted in this work. Figures 1.1, 2.1, 2.2, 3.9, and 5.9 were obtained with permission from the corresponding authors Natalia Ivanova, James Stone, Volker Springel, Philip Chang, and Alexandra Spaulding, respectively.

I am supported by the R1 Distinguished Dissertation Fellowship at UWM and by the NASA Astrophysics Theory Program through NASA grant NNH17ZDA001N-ATP. I have used the YT software platform for the analysis of the data and generation of plots in this work (Turk et al., 2011). I use the Extreme Science and Engineering Discovery Environment (XSEDE), which is supported by National Science Foundation (NSF) grant No. ACI-1053575. I acknowledge the Texas Advanced Computing Center (TACC) at The University of Texas at Austin (URL: http://www.tacc.utexas.edu) as well as the UWM HPC Service (URL: https://uwm.edu/hpc/) for providing HPC resources that have contributed to the research results reported within this paper.

Computational resources supporting this work were also provided by the NASA High-

End Computing (HEC) Program through the NASA Advanced Supercomputing (NAS) Division at the Ames Research Center. This material is based upon work supported by NASA under Award No. RFP19_7.0, RFP20_6.1, and RFP21_7.0 issued through the Wisconsin Space Grant Consortium and the National Space Grant College and Fellowship Program. Any opinions, findings and conclusions or recommendations expressed in this material are those of the author and do not necessarily reflect the views of the National Aeronautics and Space Administration.

CHAPTER 1

Physics of Common Envelope Evolution

1.1 FORMATION CHANNELS

CEE is thought to be responsible for the formation of many binary systems containing at least one compact object. These include double white dwarfs, X-ray binaries, millisecond pulsars (MSPs), and the progenitors of type Ia supernovae (Ivanova et al., 2013; Belczynski et al., 2016). Several of the formation channels for these binaries are shown in Fig. 1.1. Recent years have seen an increase in the study of CEE due to the recent detections of merging black holes and neutron stars by Advanced LIGO. In particular, the high masses of merging binaries such as GW170729 (80 $M_\odot$), GW170823 (66 $M_\odot$) (Abbott et al., 2019), and GW150914 (63 $M_\odot$) (Abbott et al., 2016) have triggered a flurry of activity focusing on their origins. Though the formation of single black holes through stellar evolution is well-understood, the mechanism by which these binaries tighten to the point where the emission of gravitational radiation results in a merger is unknown. Indeed, two 10 $M_\odot$ black holes in a circular orbit would need to be separated by only 20 $R_\odot$ to merge within the age of the universe (Mandel & Farmer, 2018). Several candidate theories have surfaced to explain the formation of these binaries, including CEE (Belczynski et al., 2016; Kruckow et al., 2016), dynamical processes (Rodriguez et al., 2016; Antonini & Rasio, 2016; Chatterjee et al., 2017), and chemically homogeneous evolution (de Mink & Mandel, 2016; Marchant et al., 2016), but so far it is unclear which of these make significant contributions to the merger rate.

CEE is also believed to be involved in the progenitors of both types of gamma-ray bursts (GRBs). Short-period GRBs are thought to result from binary neutron star mergers, and CEE facilitates the tightening of these binaries prior to merger. On the other hand, long-period GRBs are thought to result from core-collapse supernovae in massive stars which are rapidly rotating and have been stripped of their outer envelopes. CEE provides a mechanism by which both the rapid rotation and the stripping of the envelope can be accomplished (Fryer et al., 1999, 2007; Podsiadlowski et al., 2010).

Type Ia supernovae could also involve CEE through the merger of carbon-oxygen white dwarfs (Webbink, 1984; Iben & Tutukov, 1984). In order to generate a type Ia supernova, these WDs need to be fairly massive, indicating that they were formed inside stars that had ample time for the core to evolve. This, in turn, indicates that the initial binary must have had a large separation to accommodate the large radii of these stars. However, at some point the orbital separation must have decreased dramatically to allow for a merger between the WDs to be mediated by gravitational waves. Again, CEE provides a mechanism by which this can occur by quickly tightening the binary.

Because CEE is a very brief process in the lifetime of a star and is much dimmer than other transients such as supernovae, it is very difficult for astronomers to directly observe. Furthermore, theoretical studies of CEE are hampered by the diverse physics thought to be involved as well as the dynamic range of time-scales (Webbink, 2008; Ivanova et al., 2013). For example, considerations such as hydrodynamics, convection, turbulence, accretion, nuclear burning, radiation, self-gravity, hydrogen recombination, jets, and magnetism are all thought to play a role in CEE. As a result, our understanding of the formation of compact binaries stems mostly from binary population synthesis (BPS). Population synthesis uses simple physical models to simulate the evolution of many systems ($\sim 10^8$ or more) at once. BPS is the application of population synthesis to binary systems, and allows us to convert an initial population of stars with a given initial mass function (IMF) and separation distribution into a population of compact binaries and other post-common envelope systems. To avoid large computational costs, BPS uses simplified descriptions

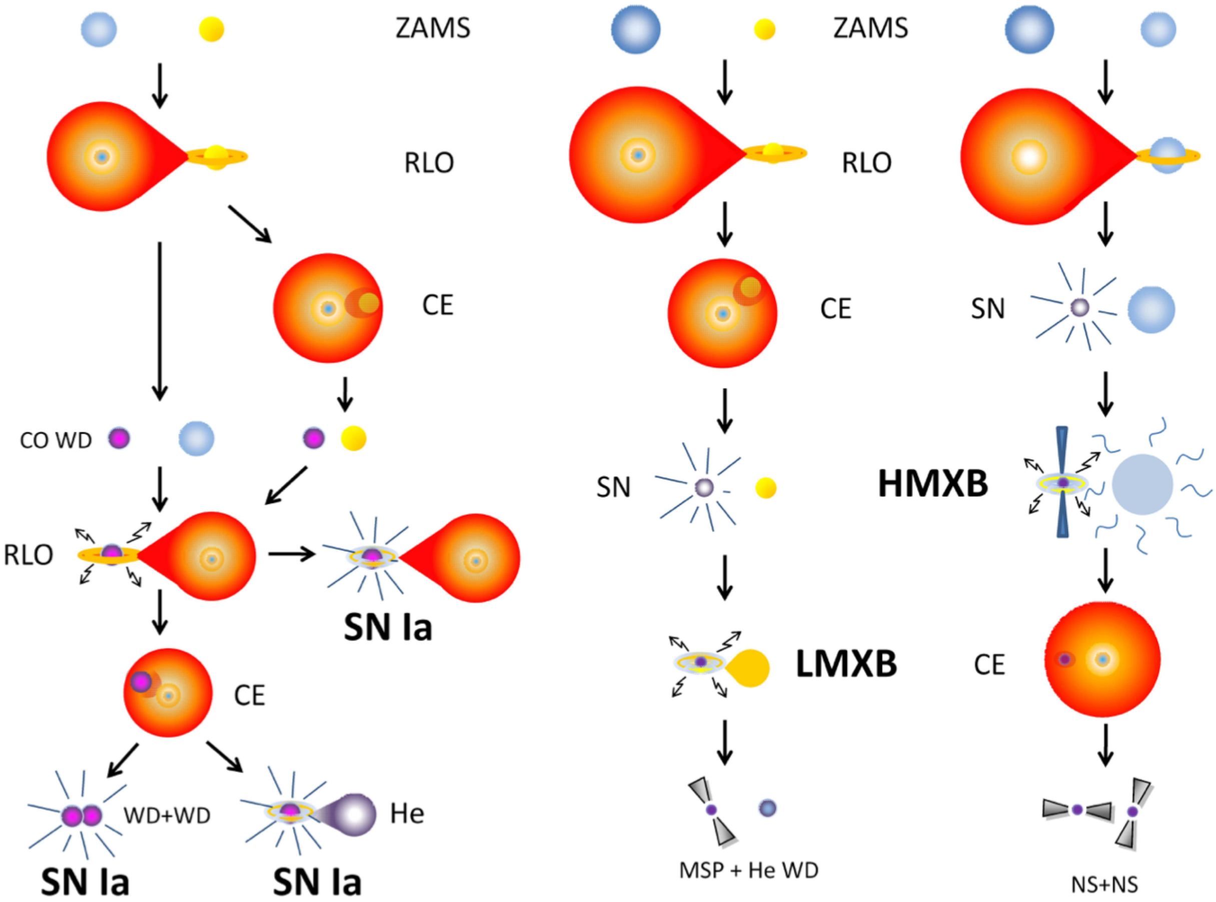

Figure 1.1: The role of CEE in several of the many formation channels for compact binaries and other exotica, reprinted from (Ivanova et al., 2013).

of CEE and other aspects of stellar evolution. In particular, this often involves assuming a single value for the CEE efficiency parameter α_{CE} discussed below. Furthermore, BPS codes often treat α_{CE} as a free or tunable parameter rather than a function of the properties of the binary (for example, Giacobbo & Mapelli, 2018). This is a highly undesirable state of affairs since the results of BPS studies are sensitive to their treatment of CEE.

1.2 STAGES

Due in part to the large range of timescales involved in CEE, astronomers divide CEE into distinct phases which can be studied individually.

1.2.1 Loss of Corotation

Prior to CEE, the binary has been in a stable orbit. The binary separation is small enough that tidal forces from the companion have spun up the rotation of the giant until the giant is tidally locked to the binary orbit (Soker, 1996). The rotation rate can be a significant fraction of the giant's break-up velocity. This corotation is lost when the giant overflows its Roche lobe and begins a period of unstable mass transfer onto the companion. The loss of corotation operates on a dynamical timescale; prior evolution leading up to this phase occurs on many dynamical timescales (for the tidal locking) as well as the thermal timescale (for the expansion of the primary as it ascends the red giant branch or asymptotic giant branch) (Podsiadlowski et al., 2002).

Loss of corotation could also be caused by other effects such as the Darwin instability (Darwin, 1879), which occurs when the spin angular momentum of the binary exceeds one-third of its orbital angular momentum. At this point, the tidal forces cause a runaway transfer of angular momentum from the orbit to the spins of the binary components, leading to a merger. Here we will focus on the case of unstable mass transfer, as this mechanism is relevant to our systems of interest.

1.2.2 Radial Plunge

Immediately following the loss of corotation is the radial plunge, which is a rapid inspiral that occurs on the dynamical timescale. Here the transfer of orbital energy to the envelope results in the partial or complete ejection of the envelope from the binary. This phase is the primary focus of my work, as it occurs over a timescale which hydrodynamical simulations are well-suited to model.

1.2.3 Self-Regulating Spiral-In

Once the envelope has expanded enough that the binary orbit is cleared, the inspiral stalls and a self-regulating phase begins (assuming that the envelope has not been entirely ejected during the radial plunge). In this phase, the envelope is held in limbo as its gravitational attraction to itself and to the binary is balanced by heating from interactions between the binary and the inner envelope. If the local density around the binary orbit rises, frictional luminosity will generate additional heating, keeping the envelope in a stable equilibrium (Meyer & Meyer-Hofmeister, 1979). Thus, the self-regulating phase operates on the thermal timescale of the envelope. This phase is best studied by 1-D models which can follow the evolution over much longer timescales than 3-D hydrodynamical simulations.

1.2.4 Termination of Self-Regulating Phase

If the envelope receives enough energy from frictional luminosity to be ejected, the self-regulating phase is terminated (Ivanova, 2002; Han et al., 2002). Another possibility is that one of the binary components again overflows its Roche lobe, which can result in a merger (Ivanova, 2002) but can also provide a mechanism for liberating orbital energy to eject the envelope (Ivanova et al., 2002; Podsiadlowski et al., 2010). Like the radial plunge, this also operates on the dynamical timescale.

1.3 ENERGY FORMALISM

The energy formalism, also known as the α-formalism, is a theoretical model to analyze the energetics of a common envelope phase (van den Heuvel, 1976; Webbink, 1984; Livio & Soker, 1988; Iben & Livio, 1993). Here the orbital energy lost by the binary is compared against the binding energy of the envelope. The liberated orbital energy can be expressed as

$$\Delta E_{\text{orb}} = -\frac{Gm_1m_2}{2a_i} + \frac{Gm_{1,\text{c}}m_2}{2a_f}, \tag{1.1}$$

where m_1 and m_2 are the initial masses of the primary and secondary, $m_{1,\text{c}}$ is the mass of the primary core, and a_i and a_f are the initial and final binary separations. On the other hand, the binding energy of the envelope can be expressed as

$$E_{\text{bind}} = \frac{m_1m_{1,\text{env}}}{\lambda R_1}, \tag{1.2}$$

where $m_{1,\text{env}}$ is the mass of the envelope and R_1 is the radius of the primary. The parameter λ accounts for the effect of stellar structure on the binding energy (de Kool, 1990; Dewi & Tauris, 2000, 2001). The value of λ varies by star as well as on the definition of the boundary between the core and envelope (Tauris & Dewi, 2001). Furthermore, the definition of λ in literature is inconsistent.

The energy formalism then comes from equating ΔE_{orb} to E_{bind}. However, not all of the orbital energy contributes to envelope ejection. Therefore, we must introduce an efficiency parameter α_{CE}:

$$\frac{m_1m_{1,\text{env}}}{\lambda R_1} = \alpha_{\text{CE}}(-\frac{Gm_1m_2}{2a_i} + \frac{Gm_{1,c}m_2}{2a_f}). \tag{1.3}$$

Note that the energy formalism assumes that material ejected from the envelope acquires no more energy than that needed to escape at exactly the local escape velocity. This is generally untrue; even if $\alpha_{\mathrm{CE}}\Delta E_{\mathrm{orb}}$ exceeds the binding energy, the fraction of the envelope which actually escapes from the systems depends on how this energy is distributed throughout the envelope. The energy formalism also assumes that the envelope need only escape from the primary, neglecting the companion as a source of binding energy.

One might expect α_{CE} to take on values between 0 and 1. However, BPS studies often choose values for the efficiency parameter which exceed unity. Though this at first glance seems to violate energy conservation, this choice is used to account for alternate sources of energy not included in the energy formalism. One such source is recombination energy, which is a potentially large source of energy in the outer envelope. When ionized material in the envelope cools, it can recombine into atoms and release energy, which we discuss further in section 3.3. The formalism also ignores radiative losses and other energy sinks. Tidal heating is not a source of energy, as it is a mechanism by which orbital energy is transferred to the envelope. However, it may aid in the common envelope efficiency.

In short, the two parameters λ and α_{CE} encode our ignorance of the important physics and are poorly constrained by theory and observation. Fortunately, (1.3) allows us to combine them into a single parameter $\alpha_{\mathrm{CE}}\lambda$.

An alternative to the energy formalism is the angular momentum formalism, also known as the γ-formalism (Nelemans et al., 2000; Nelemans & Tout, 2005). Instead of orbital energy, this formalism considers the amount of angular momentum lost by the binary:

$$\frac{\Delta J_{\mathrm{binary}}}{J_i} = \gamma \frac{m_{1,\mathrm{env}}}{m_1 + m_2}. \tag{1.4}$$

Here the initial angular momentum of the binary is J_i and γ is the efficiency parameter.

The γ-formalism was introduced to explain a set of double white dwarf systems which are thought to have been formed through two common envelope events. These events all shared similar values of γ, making the formalism useful for these systems. However, when applied to a wider range of systems, the γ formalism encounters problems similar to those experienced by the energy formalism.

1.4 OBSERVATIONS

CEE events are difficult to observe due to their short periods relative to a stellar lifetime. We are therefore mostly relegated to observing pre-common envelope (i.e. stellar binaries) and post-common envelope systems such as compact binaries and planetary nebulae (PNe). Furthermore, theory provides few predictions for the appearance of such an event due to the fact that the phases operate on much different timescales; this means that CEE cannot be modeled consistently from beginning to end. For example, 1-D calculations must be used to study the self-regulating phase, but 3-D codes are used to study the radial plunge. To make matters worse, the best-studied phase – the radial plunge – is also the shortest.

It is thought that roughly 20% of PNe are formed as a result of envelope ejection from CEE (Han et al., 1995; Bond, 2000). Thus, astronomers have tried to work backward, using the shapes and velocities of PNe to infer information about how the envelope was ejected. Such PNe can take on a variety of shapes, but a bipolar shape is favored due to the fact that much of the envelope is ejected in the equatorial plane (Sandquist et al., 1998). Then a fast wind from the primary is collimated in the polar direction by the ejected envelope. Magnetic fields are also thought to play a role in forming the bipolar shape, and recent work using magnetohydrodynamical (MHD) simulations to study a CEE event over several thousand days supports this hypothesis (Ondratschek et al., 2021). As we show in section 5.5.3, magnetic fields thought to be responsible for shaping the PNe are found to form quickly at the onset of CEE (also see Ohlmann et al., 2016b).

Besides the possible existence of a PNe, the binary resulting from CEE can also be used as a probe. The masses and periods of these post-common envelope binaries (PCEBs) can be used to estimate values of $\alpha_{\rm CE}$ (for example, Zorotovic et al., 2010). But again, there is no reason to believe that even systems which are alike will have $\alpha_{\rm CE}$ values that are equal or even similar.

There is some hope for detecting CEE as a transient event, as they are expected to produce energy roughly equal to the binding energy of the envelope ($\sim 10^{47}$ ergs) (Kulkarni et al., 2007). Indeed, there are several transients which are thought to have been caused by CEE or other violent binary interactions; these include the eruptions of V838 Mon (Bond et al., 2003) and V1309 Sco. In particular, V1309 Sco is thought to be a stellar merger due to its steadily decreasing period prior to its eruption and lack of a binary companion afterward (Tylenda et al., 2011). The resemblance of V1309 Sco to V838 Mon (for example, Retter & Marom, 2003) and other transients has spawned a class of red transients thought to be connected to binary interactions. Members of this class, which include M31 LRN2015 (MacLeod et al., 2017b), PTF 10fqs (Kasliwal et al., 2011), and M85 OT2007 (Kulkarni et al., 2007), are known as "intermediate-luminosity optical transients" (ILOTs) or "red novae." These events have absolute visual magnitudes M_V in the range of -13 to -15, placing them between the luminosities of novae and supernovae (Ivanova et al., 2013). Though ILOTs are not novae, they are thought to occur at as much as 20% of the rate of core-collapse supernovae (Thompson et al., 2009). Furthermore, the timescales of the light curves of ILOTs broadly agree with what we know about CE events, lasting for roughly ten dynamical times (MacLeod et al., 2017b). This is much shorter than either the thermal or nuclear timescales and indicates a dynamical phenomenon.

CHAPTER 2

Moving-Mesh Hydrodynamics

We begin this chapter with a discussion of two numerical methods which have been instrumental in simulating astrophysical phenomena such as stars, accretion disks, and galaxies. These are smoothed-particle hydrodynamics (SPH) and Eulerian grid codes, each of which comes with its own set of strengths and challenges. We then describe the arbitrary Lagrangian-Eulerian (ALE) method, a relatively recent development which is a hybrid of the two aforementioned methods. Implementations of ALE methods involve the motion and deformation of a mesh; for this reason, they are referred to as moving-mesh (MM) codes.

2.1 SMOOTHED-PARTICLE HYDRODYNAMICS

2.1.1 Overview

SPH is based on the Lagrangian formulation of fluid dynamics in which the fluid is composed of particles, each of which traces out an individual path in space and time. In practice, this means that SPH codes model the fluid as a collection of fixed-mass particles whose properties evolve according to the Euler equations. SPH is able to automatically adjust its resolution as needed, since – for example – a clumping of matter corresponds to a clumping of particles (Springel, 2010b). This affords it the ability to treat problems involving large dynamic ranges. Lagrangian schemes are also naturally Galilean invariant and immune to advection errors. Furthermore, they are easily adapted to self-gravity algorithms (Hernquist & Katz, 1989) and are computationally inexpensive.

For a review of SPH, see Monaghan (1992); Dolag et al. (2008); Rosswog (2009); Springel (2010b). Common SPH codes include GADGET (Springel et al., 2001), HYDRA (Pearce &

Couchman, 1997), MAGMA (Rosswog & Price, 2007), and VINE (Wetzstein et al., 2009). Additionally, the SPH code ChaNGa (Jetley et al., 2008, 2010; Menon et al., 2015) – based on the earlier code GASOLINE (Wadsley et al., 2004a) – forms the basis of MANGA, which we discuss in detail in section 2.4.

2.1.2 Formalism

At the heart of SPH is the kernel function, which is used to smooth a field $F(\boldsymbol{r})$ to form a smoothed field $F_s(\boldsymbol{r})$ using a convolution integral:

$$F_s(\boldsymbol{r}) = \int F(\boldsymbol{r}')W(|\boldsymbol{r} - \boldsymbol{r}'|, h)d\boldsymbol{r}'^3. \tag{2.1}$$

Here $W(|\boldsymbol{r}-\boldsymbol{r}'|, h)$ is a kernel with characteristic width h, known as the smoothing length. The smoothing length is sometimes allowed to vary depending on the clustering of particles; for example, in ChaNGa it varies such that 64 particles lie within h_i of the particle at $\boldsymbol{r}_i$. There are many possible choices of kernel, but all share the properties of being symmetric, normalized to unity, monotonically decreasing, and (at least) twice differentiable. A typical choice for the kernel is a cubic spline which vanishes for $|\boldsymbol{r} - \boldsymbol{r}'| > 2h$. There are many similar choices of kernel (Schoenberg, 1969; Hockney & Eastwood, 1981; Monaghan, 1985), but nearly all of them vanish outside a radius of $\mathcal{O}(h)$. This is due in part to computational considerations: a kernel with infinite extent would require a summation over all particles to perform a single smoothing calculation. Thus the computational cost of the entire smoothing computation would scale as the square of the number of particles N^2. This is the case for Gaussian kernels such as the one used by Gingold & Monaghan (1977). In contrast, the computation time scales as N for a kernel with finite extent.

Equation (2.1) must be discretized, as we are not dealing with a continuous field $F(\boldsymbol{r})$ but a discrete distribution of particles $F_i(\boldsymbol{r}_i)$. To do this, we first define a volume element

$V_i = m_i/\rho_i$. Then the integral in (2.1) can be replaced by

$$F_{s,i}(\boldsymbol{r}_i) = \sum_j V_j F(\boldsymbol{r}_j) W(|\boldsymbol{r}_i - \boldsymbol{r}_j|, h_i). \tag{2.2}$$

There is a caveat here: the particles must sufficiently sample the kernel volume, so h must be at least as large as the average particle spacing.

The Euler equations for inviscid gas dynamics in Lagrangian (comoving) form are given by

$$\frac{D\rho}{Dt} + \rho \boldsymbol{\nabla} \cdot \boldsymbol{v} = 0, \tag{2.3}$$
$$\frac{D\boldsymbol{v}}{Dt} + \frac{\boldsymbol{\nabla} P}{\rho} = 0, \tag{2.4}$$

and

$$\frac{Du}{Dt} + \frac{P}{\rho} \boldsymbol{\nabla} \cdot \boldsymbol{v} = 0, \tag{2.5}$$

where ρ, $\boldsymbol{v}$, P, and u are the fluid density, velocity, pressure, and internal energy. Here $D/Dt = \partial/\partial t + \boldsymbol{v} \cdot \boldsymbol{\nabla}$ is the convective derivative. We will treat only inviscid fluids – in which viscosity can be neglected – as these are most relevant in astrophysics due to the high Reynolds numbers involved. Rather than discretizing these equations directly, as is done in Eulerian hydrodynamics, it is perhaps more useful to use the Lagrangian. Shown in both its integral and discretized forms, the Lagrangian for an inviscid gas is

$$L = \int \rho(\boldsymbol{v}^2/2 - u) dV = \sum_i (m_i \boldsymbol{v}_i^2/2 - m_i u_i). \tag{2.6}$$

Then the Euler-Lagrange equation can be used to derive the SPH equations of motion

(Springel, 2010b).

2.1.3 Artificial Viscosity

Due to its smoothing nature, SPH encounters issues when confronted with discontinuities including shock waves and contact discontinuities. Whereas Eulerian methods can sharply resolve the location of a discontinuity, in SPH they are smeared out across several particles. These poor gradient estimates can lead to suppression of fluid instabilities (Agertz et al., 2007). Furthermore, the SPH formalism assumes inviscid flow, which is not valid for shock waves due to the increase in entropy experienced by particles which cross a shock front. Thus, one must introduce a method by which kinetic energy can be dissipated into heat when a discontinuity is encountered.

This is accomplished by introducing an artificial viscosity by applying a friction force to damp the relative motion of particles. The viscosity sources the momentum and energy equations as follows:

$$\left.\frac{D\boldsymbol{v}_i}{Dt}\right|_{\text{visc}} = -\sum_{j=1} m_j \Pi_{ij} \boldsymbol{\nabla}_i \overline{W}_{ij}, \tag{2.7}$$

$$\left.\frac{Du_i}{Dt}\right|_{\text{visc}} = \frac{1}{2}\sum_{j=1} m_j \Pi_{ij} \boldsymbol{v}_{ij} \cdot \boldsymbol{\nabla}_i \overline{W}_{ij}. \tag{2.8}$$

Here $\overline{W}_{ij}$ is the symmetrized kernel

$$\overline{W}_{ij} = [W(|\boldsymbol{r}_i - \boldsymbol{r}_j|, h_i) + W(|\boldsymbol{r}_i - \boldsymbol{r}_j|, h_j)]/2 \tag{2.9}$$

and Π_{ij} is the viscosity factor which is symmetric in i and j. Π_{ij} is a function of the relative position $\boldsymbol{r}_{ij} = \boldsymbol{r}_i - \boldsymbol{r}_j$ and velocity $\boldsymbol{v}_{ij} = \boldsymbol{v}_i - \boldsymbol{v}_j$, and is chosen to vanish if $\boldsymbol{r}_{ij} \cdot \boldsymbol{v}_{ij} > 0$. Note that while Π_{ij} and $\overline{W}_{ij}$ are symmetric under an exchange of indices, $\boldsymbol{\nabla}_i \overline{W}_{ij}$ is antisymmetric. This means that any momentum lost by one particle due to (2.7) will be gained by another, preserving momentum conservation. Similarly, the thermal energy source (2.8) compensates for the kinetic energy sapped by (2.7). Also note that $\boldsymbol{v}_{ij} \cdot \boldsymbol{\nabla}_i \overline{W}_{ij}$ is symmetric, so that all particles *gain* thermal energy.

It is important to ensure that the artificial viscosity is only activated when there is a shock present. Shear flows can be problematic in this regard because the relative particle velocities are high, and Π_{ij} scales linearly with $\boldsymbol{v}_{ij}$ at low Mach numbers (Monaghan, 1997; Monaghan & Gingold, 1983). A common fix to this issue is the Balsara switch (Balsara, 1995), which makes the replacement

$$\Pi_{ij} \longrightarrow \frac{f_i^{\mathrm{AV}} + f_j^{\mathrm{AV}}}{2} \Pi_{ij}, \tag{2.10}$$

where

$$f_i^{\mathrm{AV}} = \frac{|\boldsymbol{\nabla} \cdot \boldsymbol{v}|_i}{|\boldsymbol{\nabla} \cdot \boldsymbol{v}|_i + |\boldsymbol{\nabla} \times \boldsymbol{v}|_i}. \tag{2.11}$$

With this switch, Π_{ij} vanishes for flows with large shear $|\boldsymbol{\nabla} \times \boldsymbol{v}|$ and low compression $|\boldsymbol{\nabla} \cdot \boldsymbol{v}|$.

2.2 EULERIAN GRID CODES

Contrary to the Lagrangian viewpoint, the Eulerian formulation of fluids watches the flow of a fluid past a static point of reference in space. Eulerian codes discretize the space into a mesh rather than discretizing the fluid into particles. Cartestian meshes are the most common, though cylindrical, spherical, and other geometries are often used for specific applications. The presence of a mesh allows the application of finite-volume methods – which are superior at modeling shocks and other discontinuities – to solve the Euler equations. Common Eulerian grid-based codes are FLASH (Fryxell et al., 2000), RAMSES (Teyssier, 2002), HARM (Gammie et al., 2003), Athena (Stone et al., 2008), and Enzo (Bryan et al., 2014), to name just a few.

The Euler equations written in conservative form are

$$\begin{aligned} \frac{\partial \rho}{\partial t} + \boldsymbol{\nabla} \cdot (\rho \boldsymbol{v}) &= 0, && (2.12) \\ \frac{\partial \rho \boldsymbol{v}}{\partial t} + \boldsymbol{\nabla} \cdot (\rho \boldsymbol{v} \boldsymbol{v}^T) + \boldsymbol{\nabla} P &= -\rho \boldsymbol{\nabla} \Phi, && (2.13) \end{aligned}$$

and

$$\frac{\partial \rho e}{\partial t} + \boldsymbol{\nabla} \cdot (\rho e + P)\, \boldsymbol{v} = -\rho \boldsymbol{v} \cdot \boldsymbol{\nabla} \Phi, \tag{2.14}$$

where ρ is the density, $\boldsymbol{v}$ is the fluid velocity, Φ is the gravitational potential, $e = \epsilon + v^2/2$ is the specific energy, ϵ is the specific internal energy, and $P(\rho, \epsilon)$ is the pressure. Equations (2.12) to (2.14) can be written in a compact form by introducing a state vector $\boldsymbol{\mathcal{U}} = (\rho, \rho \boldsymbol{v}, \rho e)$:

$$\frac{\partial \boldsymbol{\mathcal{U}}}{\partial t} + \boldsymbol{\nabla} \cdot \boldsymbol{\mathcal{F}} = \boldsymbol{\mathcal{S}}, \tag{2.15}$$

where $\boldsymbol{\mathcal{F}} = (\rho \boldsymbol{v}, \rho \boldsymbol{v} \boldsymbol{v}^T + P\mathbb{I}, (\rho e + P)\boldsymbol{v})$ is the flux function and $\boldsymbol{\mathcal{S}} = (0, -\rho \boldsymbol{\nabla} \Phi, -\rho \boldsymbol{v} \cdot \boldsymbol{\nabla} \Phi)$ is the source function. Here $\mathbb{I}$ is the identity matrix. For each cell, the integral over the volume of the ith cell V_i defines the charge of the ith cell to be

$$\boldsymbol{U}_i = \int_{V_i} \boldsymbol{\mathcal{U}} dV = \boldsymbol{\mathcal{U}}_i V_i. \tag{2.16}$$

We then use Gauss' theorem to convert the volume integral over the divergence of the flux in equation (2.15) to a surface integral

$$\int_{V_i} \boldsymbol{\nabla} \cdot \boldsymbol{\mathcal{F}} dV = \int_{\partial V_i} \boldsymbol{\mathcal{F}} \cdot \hat{\boldsymbol{n}} dA, \tag{2.17}$$

where ∂V_i is the boundary of the cell. We now take advantage of the fact that the volumes are cells with a finite number of neighbors to define an integrated flux

$$\int_{\partial V_i} \boldsymbol{\mathcal{F}} \cdot \hat{\boldsymbol{n}} dA = \sum_{j \in \text{neighbors}} \boldsymbol{F}_{ij} A_{ij}, \tag{2.18}$$

where $\boldsymbol{F}_{ij}$ and A_{ij} are the average flux and area of the common face between cells i and j. The discrete time evolution of the charges in the system from step n to step $n+1$ is given by

$$\boldsymbol{U}_i^{n+1} = \boldsymbol{U}_i^n + \Delta t \sum_j \hat{\boldsymbol{F}}_{ij} A_{ij} + \Delta t \boldsymbol{S}_i, \tag{2.19}$$

where $\hat{\boldsymbol{F}}_{ij}$ is an estimate of the half time-step flux between the initial $\boldsymbol{U}_i^n$ and final states $\boldsymbol{U}_i^{n+1}$ and $\boldsymbol{S}_i = \int_{V_i} \boldsymbol{\mathcal{S}} dV$ is the time-averaged integrated source function. The flux and source function are determined at the half-time-step so that the algorithm achieves second-order accuracy in time.

The face flux $\hat{\boldsymbol{F}}_{ij}$ is determined using the state $\boldsymbol{\mathcal{U}}$ and flux function $\boldsymbol{\mathcal{F}}$ on each side of the cell interface by applying an approximate Riemann solver, described by Toro (2009), at each cell interface. Several Riemann solvers are available, though the most common are the Harten-Lax-van Leer (HLL) and Harten-Lax-van Leer-Contact (HLLC) solvers. The HLL solver (Harten et al., 1983) models the interaction between the two fluid states on the left ($\boldsymbol{\mathcal{U}}_{\rm L}$) and right ($\boldsymbol{\mathcal{U}}_{\rm R}$) sides of the interface by introducing a third state

$$\boldsymbol{\mathcal{U}}^{\rm HLL} = \frac{S_{\rm R}\boldsymbol{\mathcal{U}}_{\rm R} - S_{\rm L}\boldsymbol{\mathcal{U}}_{\rm L} + \boldsymbol{\mathcal{F}}_{\rm L} - \boldsymbol{\mathcal{F}}_{\rm R}}{S_{\rm R} - S_{\rm L}}. \tag{2.20}$$

This new state originates at the interface and propagates outward at speed $S_{\rm L}$ (to the left) and $S_{\rm R}$ (to the right), which are the fastest signal speeds of each initial state. The HLL solver is discussed in more detail in sections 4.2 and 4.3.5, where we describe modifications to the solver to implement reflective boundary conditions. The approximations made by the HLL solver mean that several types of waves are not modeled correctly, including contact discontinuities and shear waves. The HLLC solver was introduced to restore these waves (Toro et al., 1994) and splits the interaction region into two partitions $\boldsymbol{\mathcal{U}}_{*,\rm L}$ and $\boldsymbol{\mathcal{U}}_{*,\rm R}$ which are separated by a third wave S_*. MANGA uses the HLLC solver by default.

Furthermore, many Eulerian codes offer adaptive resolution through adaptive mesh refinement (AMR) schemes which increase the resolution of the grid where needed (see Fig. 2.1). For each level of refinement, each cell is split into its eight octants (in 3-D) or four quadrants (in 2-D), which inherit properties based on the cell-centered values and gradients of its parent cell.

However, Eulerian methods are not without their own issues. Static grids suffer from a lack of Galilean invariance, and structured grids introduce errors in angular momentum conservation due to preferred directions. Furthermore, even with adaptive mesh refinement, grid-based solvers encounter difficulty with highly-refined regions that move with large velocities relative to the mesh. This is due to the challenges associated with adapting the mesh to the anticipated motion of the system (Springel, 2010a).

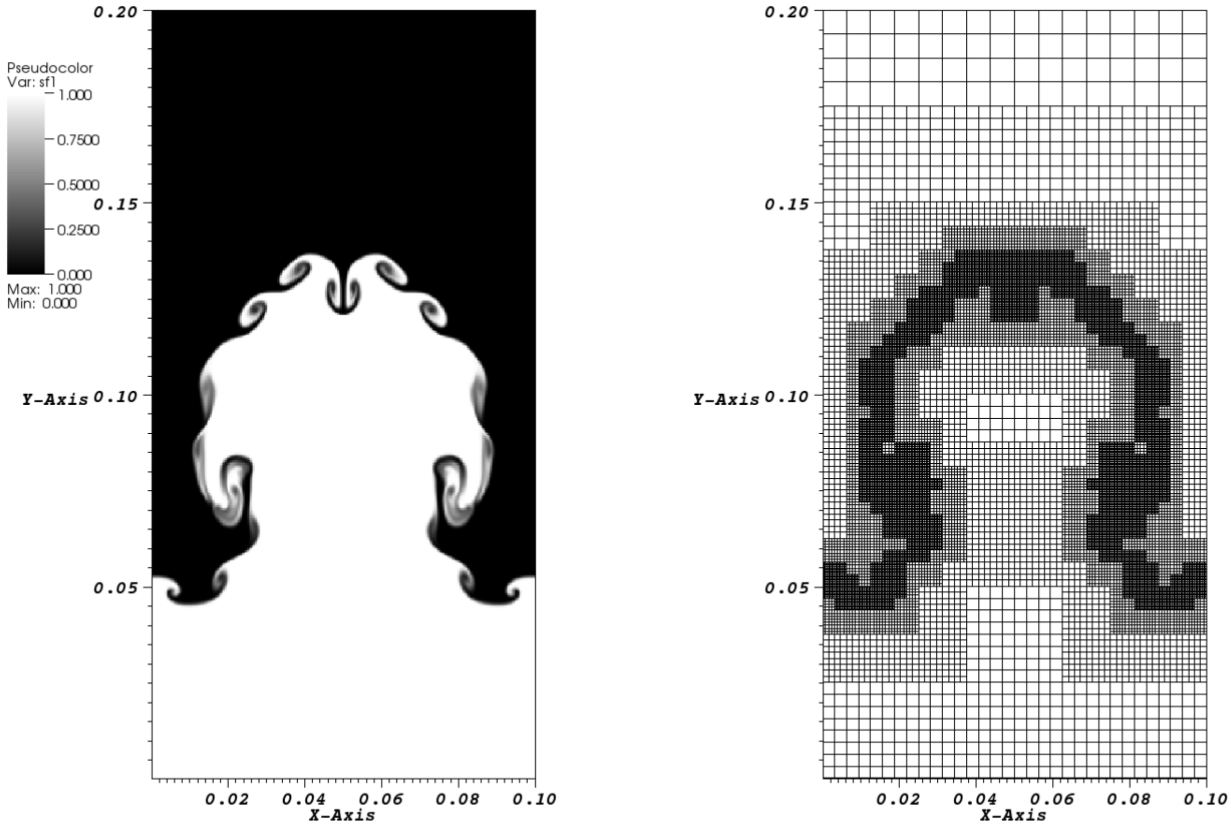

Figure 2.1: *(Left)* A Rayleigh-Taylor instability simulated using Athena in Stone et al. (2008). *(Right)* A snapshot of the mesh, showcasing the adaptive mesh refinement algorithm in Athena.

2.3 ARBITRARY LAGRANGIAN-EULERIAN SCHEMES

2.3.1 Overview

In recent decades, a new approach has developed as a hybrid of the methods presented above. This is the arbitrary Lagrangian-Eulerian (ALE) scheme, which uses a mesh that flows and deforms along with the fluid (for a review see Donea et al., 2004). Due to the presence of a mesh, finite-volume methods can be applied, allowing for the appropriate handling of discontinuities. But because the mesh moves with the fluid, ALE schemes benefit from the Galilean invariance, lack of preferred axes, and automatic resolution adjustment of Lagrangian methods.

Early attempts at ALE schemes were moving-mesh (MM) codes such as FLAME (Whitehurst, 1995) and the algorithms used in Gnedin (1995) and Pen (1998). However, these implementations were plagued by problems that involved large mesh distortions. In particular, mesh tangling can create oddly shaped elements such as "bow-tie" cells. A common approach to counteract mesh tangling is to periodically re-map the mesh onto a new, regularized mesh. This sudden re-mapping is not an ideal solution as it inherently introduces numerical diffusion. It is also difficult to create a general re-mapping algorithm that generates a mesh appropriate to a variety of problems. Due to these difficulties, it is preferable to have a mesh which can smoothly deform and re-map. Springel (2010a) described one such scheme that has proven successful, which is implemented in the code AREPO.

2.3.2 Voronoi Tessellations

To avoid the mesh tangling and re-mapping as discussed above, Springel (2010a) constructed the mesh using a Voronoi tessellation (Okabe et al., 1992) from an arbitrary distribution of mesh-generating points $\boldsymbol{p}_i$ (Fig. 2.2). For a given mesh-generating point $\boldsymbol{p}_j$, its Voronoi cell is defined as the set of all points which are closer (defined by the 2-norm) to $\boldsymbol{p}_j$ than to any other $\boldsymbol{p}_{i \neq j}$. The Euler equations (2.15) can then be solved on this mesh using the same method as described in section 2.2 with a few tweaks. There are two advantages to the use of Voronoi tessellations:

1. The tessellation is unique to the distribution of mesh-generating points.

2. The tessellation varies smoothly under perturbations of the positions of the mesh-generating points. That is, the volumes and face areas of the cells change smoothly as the mesh moves.

In addition to the Voronoi tessellation, the Delaunay triangulation is an alternative method to create a unique unstructured mesh from an arbitrary distribution of points. This results in tetrahedral cells with mesh-generating points at their vertices. Delaunay triangulations are ideal for modeling the complex geometries encountered in solid mechanics and steady-state aerodynamics. For this reason, they are commonly used in proprietary finite-element codes such as ANSYS and Star-CCM+. The Voronoi tessellation and Delaunay triangulation are said to be topologically dual to one another: the Voronoi tessellation can be determined using the Delaunay triangulation, and vice versa. This means that there are two ways in which a Voronoi tessellation can be generated:

1. The Delaunay triangulation can be generated first, then used to determine the Voronoi tesselation. Here the edge of each tetrahedron corresponds to a cell interface in the Voronoi tessellation; the cell interface occurs at the midpoint of the edge and is normal to it. This method is described in Springel (2010a) and used in AREPO, TESS (Duffell & MacFadyen, 2011), FVMHD3D (Gaburov et al., 2012), and RICH (Yalinewich et al., 2015).

2. The Voronoi tessellation can be computed directly from the mesh-generating points, in which each mesh-generating point is the center of the Voronoi cell. MANGA uses this method, using the publicly-available VORO++ libraries (Rycroft, 2009) to compute the tessellation.

The algorithm used by VORO++ to determine the Voronoi cell about a point proceeds as follows (Fig. 2.2):

1. An arbitrarily large cell is drawn around the point, with size much larger than that of the interparticle spacing.
2. The neighbors of this point are ordered by distance from the point.
3. The line connecting the point to its nearest neighbor is computed.
4. The plane bisecting this line – normal to the line at its midpoint – is computed.
5. This plane is used to split the cell into two partitions; the partition not containing the mesh-generating point is discarded.
6. Steps 3-5 are repeated with the next-nearest neighbor. This continues until the distance between the mesh-generating point and the neighbor is more than twice between the point and any vertex on the surface of the cell, meaning that the cell is complete and can no longer be partitioned.

2.4 MANGA ALGORITHM

2.4.1 Overview

As mentioned above, the SPH code ChaNGa (Charm N-body GrAvity solver) (Jetley et al., 2008, 2010; Menon et al., 2015), which is based on GASOLINE, forms the basis for the

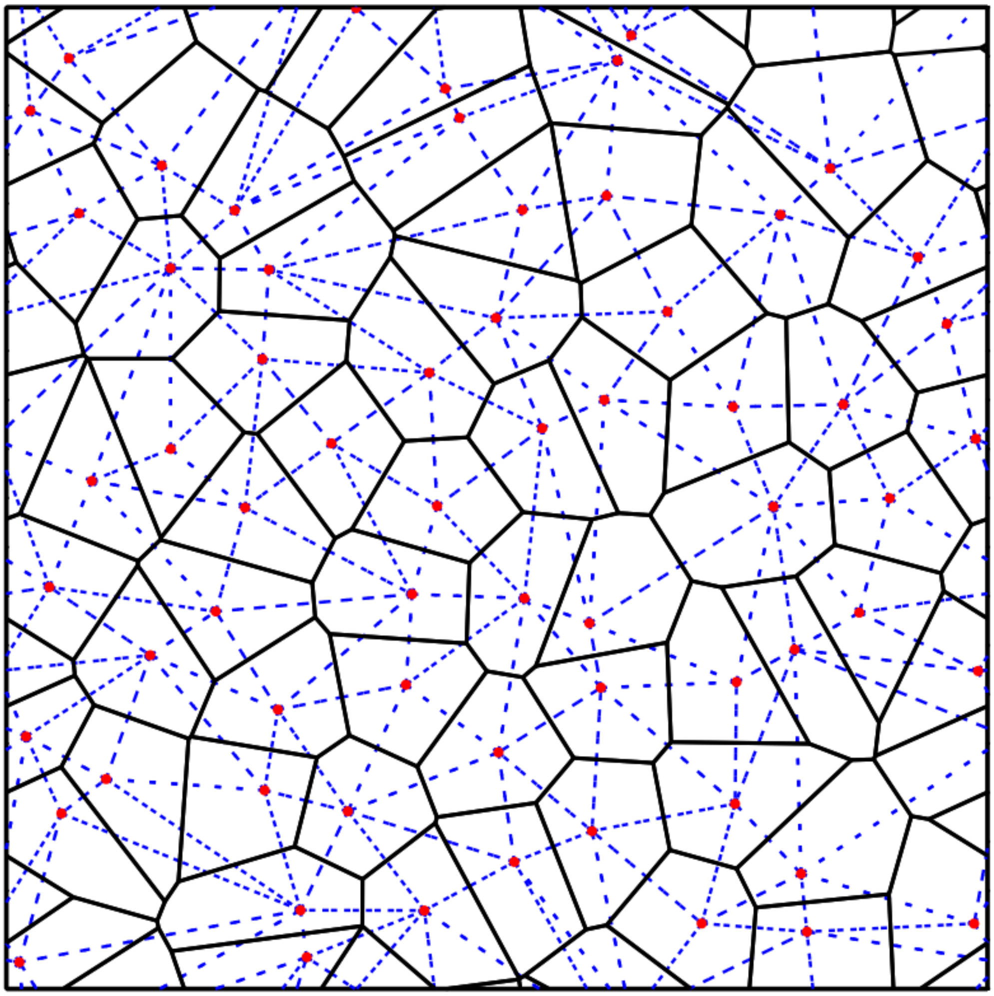

Figure 2.2: A Voronoi tessellation (black lines) generated from an arbitrary distribution of points (red). The Delaunay triangulation is also shown (blue dashed lines). Note that each line in the Delaunay triangulation corresponds to a cell face in the Voronoi tessellation (reprinted from Springel, 2010a).

moving-mesh code MANGA. Similarly, the moving-mesh code AREPO is built on top of Gadget, demonstrating that SPH codes can be adapted for ALE purposes. Rather than a custom message-passing interface (MPI) design, ChaNGa uses Charm++ (Kale & Krishnan, 1996) for parallelization, meaning that it has superior scaling. Indeed, ChaNGa has been shown to scale up to 1.2×10^{10} particles on 5.12×10^{5} cores with 93% efficiency.

2.4.2 Numerical Approach

The ALE algorithm that is implemented in MANGA is summarized as follows. We refer the reader to Chang et al. (2017) and Prust & Chang (2019) for detailed discussions. MANGA is second-order accurate in time, meaning that the error in the solution is $\mathcal{O}(\Delta t)^2$. To enforce this, at each time-step, the half-time-step values are first determined, which are then used to evolve the charges to the full time-step. We first outline the algorithm and elaborate on each step below:

1. The Voronoi tessellation is constructed using the VORO++ library.

2. Using the integral quantities $\boldsymbol{U}_i^n$, the local gradients and half time-step conserved variables $\boldsymbol{U}_i^{n+1/2}$ are calculated.

3. The cells drift by a half time-step and the Voronoi tessellation is rebuilt.

4. The state vectors at the cell interfaces are determined at the half time-step using the gradient estimates.

5. The flux across the faces is calculated using a Riemann solver.

6. The new state $\boldsymbol{U}_i^{n+1}$ is determined from the fluxes. New velocities for the mesh-generating points are determined, and the mesh-generating points drift by a full time-step.

2.4.3 Gradient Estimation

MANGA is also second-order accurate in space, which demands an appropriate estimate for the state vector at the face centers of each cell. The state vector on the face between the ith cell and its jth neighbor is taken to be

$$\tilde{\boldsymbol{\mathcal{U}}}_{ij} = \boldsymbol{\mathcal{U}}_i + (\tilde{\boldsymbol{r}}_{ij} - \boldsymbol{c}_i) \cdot \boldsymbol{\nabla} \boldsymbol{\mathcal{U}}_i, \tag{2.21}$$

where $\tilde{\boldsymbol{r}}$ and $\boldsymbol{c}_i$ are the centroids of the face and ith cell, respectively. Equation (2.21) requires an estimate of the gradient of the state vector in the ith cell. To calculate the gradients, we follow the procedure of Steinberg et al. (2016), who improved upon the prescription of Springel (2010a) in using the Gauss-Green theorem to estimate these gradients. We refer the reader to Chang et al. (2017) for a more detailed discussion.

MANGA uses a slope limiter that reduces numerical oscillations near strong gradients

$$\langle \boldsymbol{\nabla} \boldsymbol{\mathcal{U}} \rangle_i^{S10} = \alpha_i^{S10} \langle \boldsymbol{\nabla} \boldsymbol{\mathcal{U}} \rangle_i, \tag{2.22}$$

where α_i^{S10} is defined in Springel (2010a). As noted by Springel (2010a), this limiter is not total variation diminishing (TVD), so spurious oscillations can still occur. For this reason, we follow the suggestion by Duffell & MacFadyen (2011) and apply an additional slope limiter

$$\langle \boldsymbol{\nabla} \boldsymbol{\mathcal{U}} \rangle_i^{DM} = \alpha_i^{DM} \langle \boldsymbol{\nabla} \boldsymbol{\mathcal{U}} \rangle_i^{S10}, \tag{2.23}$$

where

$$\alpha_i^{DM} = \min(1, \psi'_{ij}). \tag{2.24}$$

Here,

$$\psi'_{ij} = \begin{cases} \max[\theta(\boldsymbol{\mathcal{U}}_j - \boldsymbol{\mathcal{U}}_i)/\Delta\boldsymbol{\mathcal{U}}_{ij}, 1] & |\Delta\boldsymbol{\mathcal{U}}_{ij}| > 0 \\ 1 & \text{otherwise} \end{cases} \tag{2.25}$$

and

$$\Delta\boldsymbol{\mathcal{U}}_{ij} = \langle \boldsymbol{\nabla}\boldsymbol{\mathcal{U}} \rangle_i \cdot (\boldsymbol{c}_j - \boldsymbol{c}_i). \tag{2.26}$$

This limiter is TVD if $\theta < 0.5$, and setting $\theta = 1$ reduces it to the S10 limiter.

2.4.4 Flux Computation

The flux $\hat{\boldsymbol{F}}_{ij}$ across each face is estimated as follows:

1. We first estimate the half time-step velocity $\tilde{\boldsymbol{w}}_{ij}$ of the face following Springel (2010a).

2. The state vector is boosted from the "lab" frame (the rest frame of the simulation box) to the rest frame of the face to find the flux along the normal to the face.

3. We estimate the flux $\hat{\boldsymbol{F}}_{ij}$ across the face using an HLLC (by default) or HLL approximate Riemann solver implemented following Toro (2009), as discussed in section 2.2. For magnetohydrodynamics, we use an HLLD solver as implemented in Athena++ (see Chapter 5).

4. The solved flux is boosted back into the lab frame.

We can then use the estimated fluxes to time-evolve the charges $\boldsymbol{U}_i$ following equation (2.19) using the full time-step Δt and apply changes owing to the source terms.

2.4.5 Flux Alterations Due to Mesh Motion

Because the mesh – and thus the cell interfaces – moves relative to the fluid, the flux calculations must be modified to account for this motion. For a face moving with speed $\boldsymbol{w}$, the flux across a static face $\boldsymbol{\mathcal{F}}_{\rm s}(\boldsymbol{v})$ must be supplemented by an additional term $\boldsymbol{\mathcal{F}}_{\rm corr}$ related to the flow of fluid across the face due to $\boldsymbol{w}$. This gives us the flux across a moving face

$$\boldsymbol{\mathcal{F}}_{\rm m} = \boldsymbol{\mathcal{F}}_{\rm s}(\boldsymbol{v}) - \boldsymbol{\mathcal{F}}_{\rm corr} = \begin{pmatrix} \rho\boldsymbol{v} \\ \rho\boldsymbol{v}\boldsymbol{v}^T + P \\ (\rho e + P)\boldsymbol{v} \end{pmatrix} - \begin{pmatrix} \rho\boldsymbol{w} \\ \rho\boldsymbol{v}\boldsymbol{w}^T \\ \rho e\boldsymbol{w} \end{pmatrix}. \tag{2.27}$$

However, as discussed above in section 2.4.4, the fluxes are not computed in a static frame but rather in the rest frame of the face. This is because the Voronoi cells move at or very close to the fluid velocity (see section 2.4.7), so the mass flux across the faces is very small in the lab frame. This can cause sign errors in the mass flux, which makes the scheme unstable (Pakmor et al., 2011). Instead, we work in the rest frame of the face where $\boldsymbol{\mathcal{F}}_{\rm s}(\boldsymbol{v})$ is replaced by $\boldsymbol{\mathcal{F}}_{\rm s}(\boldsymbol{v}-\boldsymbol{w})$. Then the correction for the mesh motion is expressed as

$$\boldsymbol{\mathcal{F}}_{\rm s}(\boldsymbol{v}-\boldsymbol{w}) - \boldsymbol{\mathcal{F}}_{\rm m} = \begin{pmatrix} 0 \\ \rho w^2 - \rho(\boldsymbol{v}\cdot\boldsymbol{w}) \\ \rho w^2(\boldsymbol{v}-\boldsymbol{w})/2 - \rho(\boldsymbol{v}\cdot\boldsymbol{w})(\boldsymbol{v}-\boldsymbol{w}) - P\boldsymbol{w} \end{pmatrix}. \tag{2.28}$$

These corrections are applied after a Riemann solution is performed.

2.4.6 Gravity Solver

MANGA includes self-gravity by incorporating the gravitational potential as a source term in the momentum and energy equations (2.13 and 2.14). User-specified potentials can also be used, though they are not relevant for this work. Self-gravity is handled via a tree-based gravity algorithm. The construction of the tree is summarized as follows (Wadsley et al., 2004b):

1. The simulation domain is split into its eight octants, known as tree nodes.
2. The mass multipole moments of each node are computed up to hexadecapole (fourth order).
3. Any node containing more than 12 (by default) particles is further split into its eight octants.
4. Steps 2 and 3 are repeated until the tree has been split into all of its "leaves" containing 12 or less particles.

The tree traversal algorithm is based on PKDGrav (Stadel, 2001), which is similar to the Barnes-Hut algorithm (Barnes & Hut, 1986).

The gravitational potential for each particle is not computed by summing the contributions from all other particles in the simulation, as this would result in a scaling of N^2 for the gravity solution. To optimize the calculation, only certain tree nodes are used. The nodes used in the computation are determined by the inequality

$$\frac{s}{d} < \theta, \tag{2.29}$$

where s is the width of the node, d is the distance from the node to the particle in question, and θ is some specified threshold. If the inequality is satisfied, then the node is used in the gravity computation, as the node is sufficiently far from the target particle that breaking the node down into its component nodes and leaves in not necessary. If (2.29) is not satisfied, then the node is broken down into its component nodes and the inequality is checked for each. This approach scales as approximately $N \log N$, where the base of the logarithm depends on the number of dimensions and the spatial distribution of particles.

Additionally, gravitational forces are softened using a cubic spline, reflecting the fact that the mass is not simply concentrated at a discrete distribution of points. All gas cells in ChaNGa have equal softening lengths h_{gas}, defined at the start of the simulation as the mean separation between cell centers in the region of highest density

$$h_{\mathrm{gas}} = 2(m_{\mathrm{max}}/\rho_{\mathrm{max}})^{1/3}. \tag{2.30}$$

Here ρ_{max} is the maximum density and m_{max} is the cell mass at the location of ρ_{max}.

Once the gravitational potential (and its gradient) have been computed, we can determine the time-average integrated source functions following Springel (2010a):

$$\int\limits_{V_i} \rho_i \boldsymbol{\nabla}\Phi_i dV = \frac{1}{2}(m_i^n \boldsymbol{\nabla}\Phi_I^n + m_i^{n+1}\boldsymbol{\nabla}\Phi_I^{n+1}) \tag{2.31}$$

and

$$\int\limits_{V_i} \rho_i \boldsymbol{\nabla}\Phi_i \cdot \boldsymbol{v} dV = \frac{1}{2}(m_i^n \boldsymbol{v}_i^n \boldsymbol{\nabla}\Phi_I^n + m_i^{n+1}\boldsymbol{v}_i^{n+1}\boldsymbol{\nabla}\Phi_I^{n+1}). \tag{2.32}$$

2.4.7 Voronoi Cell Velocities

ALE schemes typically set the velocities $\boldsymbol{w}$ of the mesh-generating points to the cell-centered fluid velocity $\boldsymbol{v}$. While this offers the advantages of a Lagrangian scheme, other choices are available. For example, $\boldsymbol{w} = 0$ is equivalent to using a static-mesh Eulerian scheme, while $\boldsymbol{w} = \eta\boldsymbol{v}$ where $0 < \eta < 1$ is a hybrid between the two. Though we take the Lagrangian approach, we also apply corrections to $\boldsymbol{w}$ in the interest of keeping the

Voronoi cells round. Codes which experience mesh tangling provide a cautionary tale of the numerical errors can occur with oddly-shaped or elongated cells. Thus, it is desirable to ensure that all Voronoi cells are kept reasonably round (Springel, 2010a). That is, the positions of the mesh-generating points $\boldsymbol{r}_i$ should be near to the geometric centers of the Voronoi cells $\boldsymbol{c}_i$. In MANGA and AREPO this problem is solved by modifying the velocities of the mesh-generating points such that it is difficult for such voids to appear, and they are filled in if they do appear:

$$\Delta \boldsymbol{w} = \chi c_{s,i} \frac{\boldsymbol{c}_i - \boldsymbol{r}_i}{d_i} \begin{cases} 0 & d_i < 0.9\zeta r_{\text{eff}} \\ \frac{d_i}{0.2\zeta r_{\text{eff}}} - 4.5 & 0.9\zeta r_{\text{eff}} \leq d_i \leq 1.1\zeta r_{\text{eff}} \\ 1 & d_i > 1.1\zeta r_{\text{eff}}, \end{cases} \tag{2.33}$$

where $d_i = |\boldsymbol{c}_i - \boldsymbol{r}_i|$, $c_{s,i}$ is the local sound speed, and $r_{\text{eff}} = (\frac{3}{4\pi} V_i)^{1/3}$ is the cell effective radius. We choose typical values for the constants $\chi = 1$ and $\zeta = 0.25$.

2.4.8 Multi-Stepping

Though there are several limits on the time-step for each particle, the limiting factor in the vast majority of cases is the Courant time-step

$$\Delta t_{ij} = \eta_{\text{CFL}} \frac{\Delta \boldsymbol{R}_{ij}}{c_{s,i} + c_{s,j} - \Delta \boldsymbol{v}_{ij} \cdot \Delta \boldsymbol{R}_{ij} / |\Delta \boldsymbol{R}_{ij}|}. \tag{2.34}$$

Here $\Delta \boldsymbol{R}_{ij}$ is the difference in position between the mesh-generating point (i) and a neighboring point (j), $\Delta \boldsymbol{v}_{ij}$ is the difference in fluid velocities between i and j, and $0 < \eta_{\text{CFL}} < 1$ is the Courant-Friedrichs-Levy (CFL) coefficient. The Courant time-step enforces causality: because each cell has access only to information about itself and its neighbors, information cannot be allowed to cross an entire cell in one time-step. Hence, the time-step is related to the cell size and to the maximum speed at which a wave can travel through the fluid. These are represented by the numerator and denominator of (2.34), respectively. When MHD or radiative transfer are included, the Alfvén speed or reduced speed of light (respectively) are added to the denominator of (2.34) similarly to the sound speed. The Courant time-step for a particle i is the minimum of all Δt_{ij} computed between the particle and its neighbors

$$\Delta t_i = \min_{j \in neighbors} \Delta t_{ij}. \tag{2.35}$$

MANGA as described by Chang et al. (2017) imposes a universal time-step for all particles. This global time-step is set to be the minimum Δt among all cells $\Delta t_{\mathrm{CFL}} = \min_i \Delta t_i$. Large speedups for problems with large dynamic range are possible with individual time-steps. Hence, to greatly enhance the applicability of MANGA to the problem of CEE, we have implemented an individual time-stepping scheme for MANGA. Once the Δt_i have been individually computed for each particle, the particles can be assigned to time-step levels which we call "rungs." This proceeds as follows:

1. The largest allowable time-step, which is a parameter in our simulations, is assigned to rung 0. We call this time-step Δt.

2. The time-step of each successive rung is smaller than that of the previous rung by a factor of 2. Thus the time-step associated with rung k is $\Delta t/2^k$.

3. Each particle is assigned to the rung with the maximum k satisfying $\Delta t/2^k > \Delta t_i$. That is, the highest rung with time-step larger than the particle's individual Δt_i.

The evolution of each particle then occurs according to the time-step associated with its rung.

The universal time-stepping algorithm for a second order accurate (in time) integrator can be broken down into three stages, the initial time (a), the half time-step (b), and the full time-step (c).

a. *Initial time* $t = 0$*:* determine Voronoi cells using current positions of mesh-generating points. Estimate gradients and construct half time-step predictions.

b. *Half time-step* $t = 0.5\Delta t$*:* drift Voronoi cells to half time-step positions. Construct Voronoi cells at half time-steps. Perform linear reconstruction to the half time-step cell faces and compute fluxes. Perform a Riemann solution and incorporate source terms with the *full* time-step. Place these changes into $\delta \boldsymbol{U}$.

c. *Full time-step* $t = \Delta t$*:* drift Voronoi cells to full time-step positions. Advance charges to be $\boldsymbol{U}^{n+1} = \boldsymbol{U}^{n} + \delta \boldsymbol{U}$.

In comparison, Pakmor et al. (2016) achieve the same formal second order accuracy in two steps, an initial and full time-step. Here, they make a full time-step prediction for the primitive variables, perform a Riemann solution using the initial Voronoi cells and faces for a half time-step and perform a closing Riemann solution (again a half time-step) using the final Voronoi cells and faces at the full time-step and the full time-step prediction for the primitives. The two methods differ in the comparative numbers of Voronoi tessellations and Riemann solutions. In particular, we only need to solve the Riemann problem once, whereas Pakmor et al. (2016) require two solutions of the Riemann problem (with associated linear reconstructions). However, we require an extra Voronoi calculation at the half time-step. Depending on the relative cost of Riemann solution and the Voronoi calculation, the two schemes have their relative merits.

To adapt our scheme for multistepping, we note that the full time-step for any cell involves actions at a full time-step (a, c) and the half time-step (b). Let us then consider

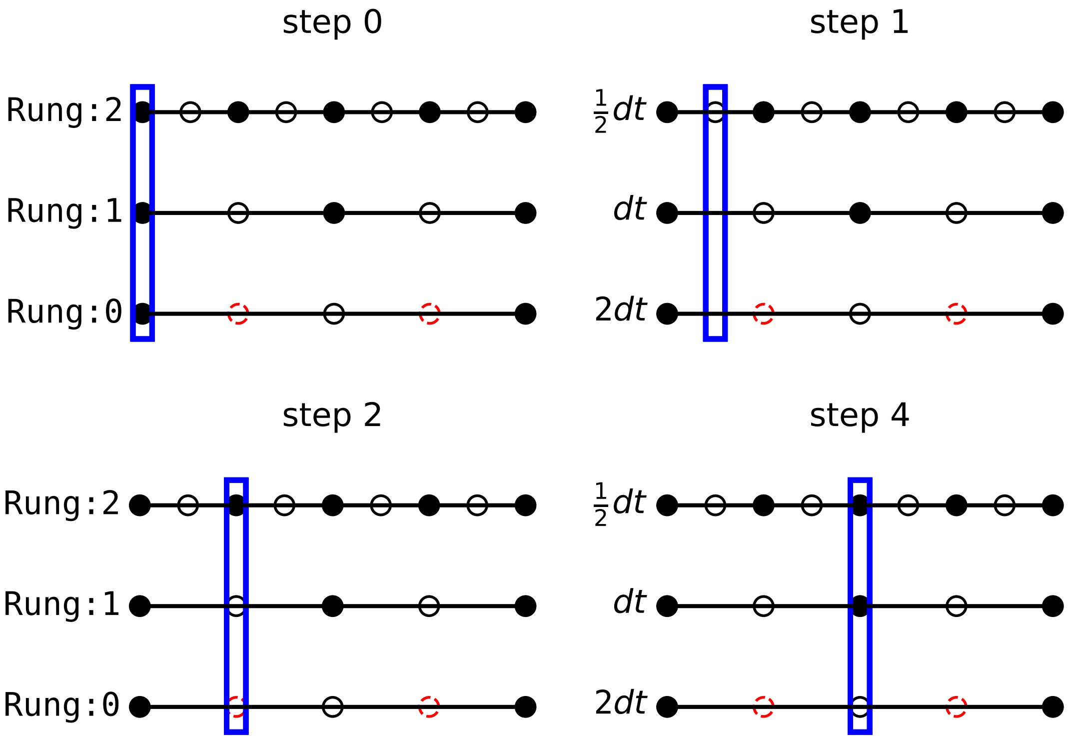

Figure 2.3: Integration of time-stepping for individual time-steps. Starting at the lowest rung (rung 0), the time-step is decreased by 2 for each higher rung. Full and half time-steps at each rung are shown as solid and empty circles, respectively. The time-stepper (blue rectangle) steps at the smallest half time-step, which in this case is at $0.25\Delta t$. All particles drift along at this smallest time-step following the time-stepper. Half time-step procedures (full time-step Riemann solutions on half time-step Voronoi cells) are executed only at half time-steps relevant to the particular rung. Full time-step procedures (accumulating all $\delta \boldsymbol{U}$'s and full time-step gradients and half time-step prediction) are executed at full time-steps. Note that only one half time-step at one rung is relevant for each step of the time-stepper, but multiple full time-steps at more than one rung can be executed at the time-stepper's current position.

the time advancement of three separate rungs at 0, 1, and 2. In Fig. 2.3, the full time-steps are represented by filled circles, while the half time-steps are represented by empty circles. At step 0, all three rungs are synchronized at their respective full time-steps: all the circles are black and step (a) is executed on all three rungs. The particles are then drifted $0.25\Delta t$ to step 1. The half time-step reconstruction and Riemann solution is performed for rung 2. Note that the Riemann solution is for the full time-step $0.5\Delta t$ at rung 2 so that when the $\delta \boldsymbol{U}$ is summed at the next step, the $\boldsymbol{U}$s for rung 2 are updated to the full time-step. Now at step 2, the full time-steps (c) and initial time-steps (a) are performed at rung 2 and the half time-step (b) is performed for rung 1. In addition, cells at rung 0 that share a face with a cell at rung 1 (denoted by red-dashed circles) also have a Riemann solution at the common face at the rung 1 half time-step. We skip step 3 as it is the same as step 1 and now proceed to step 4. Here, we do the full time-steps for rungs 1 and 2 and the half time-step for rung 0.

From this discussion, we can conclude that for the half time-step for rung k, full time-steps are executed from all rungs $m > k$. Conversely, there can only be one half time-step for only one rung per (drift) time-step. This is the half time-step of the highest rung. In addition, cells only switch rungs during their full time-steps to ensure consistency of the second-order time integration and they can only reduce their rung when their new reduced rung is at its full time-step.

One additional feature that we have included in our implementations is the smoothing of time-steps by large propagating velocity fluctuations, or shocks. This is a well known issue in SPH, for which Saitoh & Makino (2009) show that large localized changes in the time-step can lead to incorrect results. They also showed that smoothing out time-stepping changes over a SPH kernel such that the time-step variation is limited to a factor of 4 mitigates these issues. We have adopted a similar approach here in that we limit the cell's time-step to be less than $\sqrt{2}$ of the minimum time-step of its neighbors. This results in time-step changes no greater than a factor of two occurring over two cells away from a minimum cell. We find that this smoothing allows for stable integrations in MANGA.

This multi-stepping algorithm was applied to a CEE simulation to test the speed-up factor. At each step, we find speed-ups ranging from 3 to 9 times that of the universal time-stepping algorithm, resulting in an average speed-up of 4 to 5 times.

2.4.9 Van Leer Time Integration

An alternative method of achieving second-order time integration is known as the van Leer method. Rather than estimating the gradients of the conserved quantities and using them to determine the half-time-step quantities via equation (2.15), we instead solve equation (2.19) with the replacement $\Delta t \longrightarrow \Delta t/2$ and solve for the fluxes as described above. This method simplifies the code as we only need use the integral forms of the hydrodynamic equations rather than both the integral and differential forms. Van Leer integration is also easily adapted to our multistepping scheme. Finally, this method also automatically includes the source terms at second order. This follows the time integration used in Athena++ as described in White et al. (2016). Because of the necessity of computing the magnetic field flux using a Riemann solver, our MHD implementation always uses van Leer integration (see section 5.1).

2.4.10 Other Modules

Recently, modules have been added to MANGA to include physics such as radiative transfer (Chang et al., 2020), general relativistic hydrodynamics (GRHD) (Chang & Etienne, 2020), magnetohydrodynamics (MHD) (Prust & Chang, in preparation) and nuclear burning (Humphrey & Chang, in preparation). Though the GRHD and nuclear burning modules are not relevant to this work, we discuss future directions using the radiative transfer module in section 3.6.2. The MHD module is described in detail in Chapter 5.

CHAPTER 3

Simulating Common Envelope Evolution

3.1 GENERATION OF INITIAL CONDITIONS

We now discuss the development of appropriate initial conditions for MANGA. We adopt initial conditions similar to those of Ohlmann et al. (2016a), who previously performed a moving-mesh simulation of CEE. We first use the open-source stellar evolution code MESA (Paxton et al., 2011, 2013, 2015, 2018, 2019) to evolve a 2 $M_\odot$ star with metallicity $Z = 0.02$ from the pre-main sequence to the red giant phase. We stop when the star reaches 52 $R_\odot$ with a helium core mass of 0.36 $M_\odot$. Compared with that of Ohlmann et al. (2016a), our red giant is slightly larger and its helium core mass is slightly smaller. This could be due to the updates in the MESA code since their original result or discrepancies in our MESA inlists. From the MESA output, we take the entropy and hydrogen fraction. For the core, we take the total mass at a density that is 50 times greater than the mean density of the red giant, giving a core mass $M_\mathrm{c} = 0.379\ \mathrm{M}_\odot$. This corresponds to a core radius $R_\mathrm{c} = 1.99\ \mathrm{R}_\odot$, which we use as the core gravitational softening length. Because of the great difference in density between the helium core and the hydrogen envelope, we model the core as a dark matter particle with mass M_c and softening radius of R_c. The practice of excising the core and replacing it with a point particle is a common practice to reduce computation times: both the high resolution necessary to model the core as well as the high temperatures would drive down the Courant time-step. After the core is excised, the star is no longer in hydrostatic equilibrium due to the removal of its center. Thus, we then construct a star of mass $M - M_\mathrm{c}$ with an entropy profile and radius which match those of the original star and which contains a dark matter particle core. This yields a radial profile of density, temperature, and hydrogen fraction that can be mapped to a particle (mesh-generating point) profile.

The profile produced by the mapping from a 1-D stellar evolution model to a fully 3-D hydrodynamical simulation is not in perfect hydrostatic balance due to discretization errors. Previously, Chang et al. (2017) used this fact to compare (roughly) hydrostatic stars experiencing oscillations using the moving-mesh and SPH solvers. Here we are interested in the equilibrium solution in the moving-mesh solver. Thus, following the mapping from 1-D to 3-D, we damp spurious velocities and energies and allow the star to relax to a final configuration. We note that this same procedure has been used for merging white dwarfs (Zhu et al., 2013) and was also used by Ohlmann et al. (2016a) for giant star initial conditions.

We show the result of this relaxation in Fig. 3.1 as blue circles and compare this to the radial profile from MESA (orange circles). Here we downsample the number of points from MANGA by a factor of 100. The horizontal line denotes the cutoff density for the core (50 times the mean density). The envelope follows the original MESA profile quite faithfully in spite of the differences in the physical structure. The inner profile approaches a fixed density asymptotically due to the softened gravitational forces from the dark matter core.

We represent the 1 $M_\odot$ companion as a dark matter particle that is in an initially circular Keplerian orbit at the red giant radius $a = 52$ $R_\odot$. This follows the initial conditions of Ohlmann et al. (2016a) to facilitate a direct comparison. Although this neglects the evolution of the binary prior to CEE, we compensate by altering the dynamics of the giant. During the phase leading up to CEE, tidal forces from the companion on the envelope are expected to spin up the rotation of the envelope (Soker, 1996) to a significant fraction of its breakup velocity. We have implemented this corotation between the envelope rotation and orbital motion into our simulations by following the scheme of MacLeod et al. (2018).

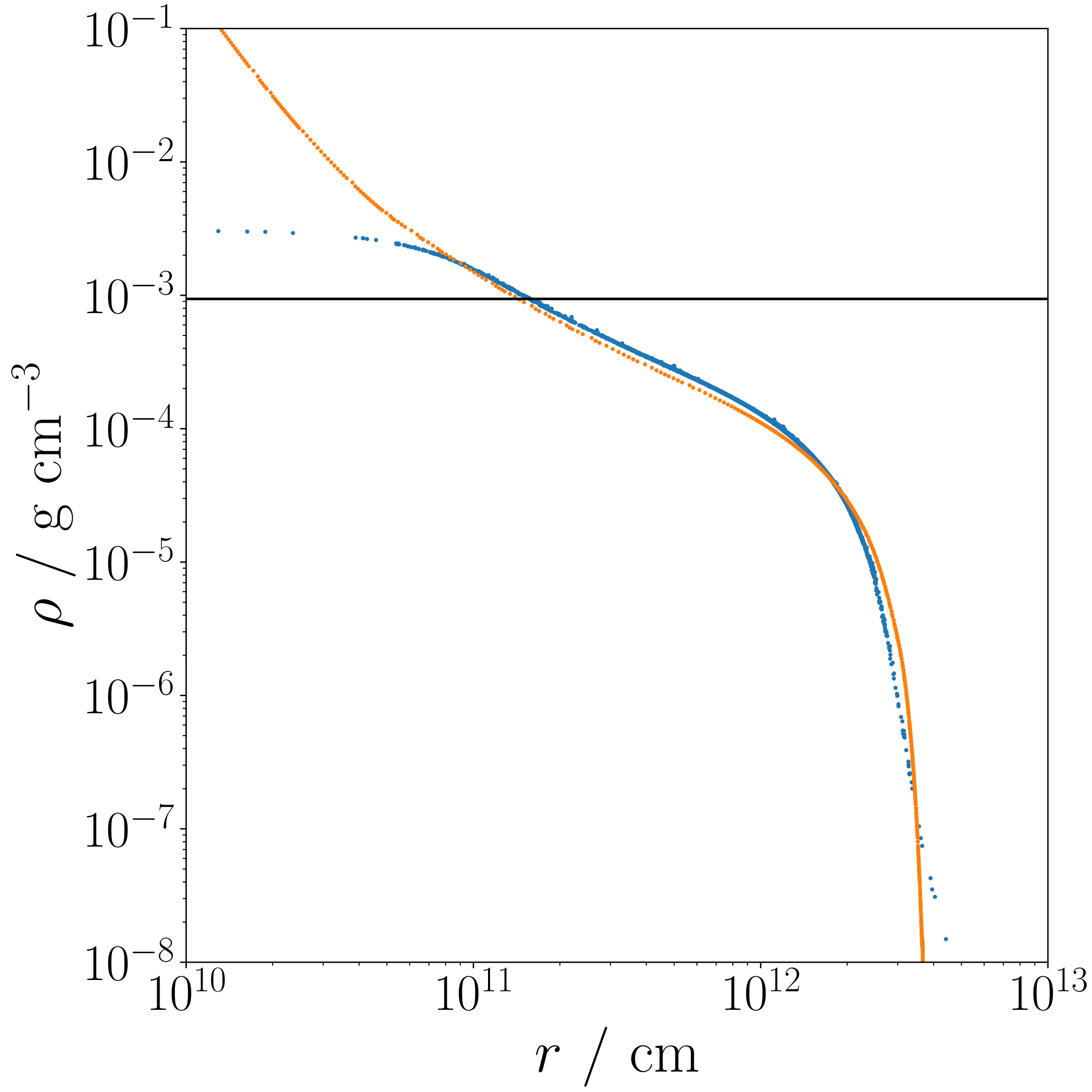

Figure 3.1: Relaxed density ρ against radius r profile from MANGA (blue circles) compared to the profile from MESA (orange circles). The horizontal line denotes the cutoff density for the dark matter core (50 times the mean density).

Within the envelope, we assume rigid body rotation and initialize the velocity as

$$v_\phi = f_{\rm cr}\Omega_{\rm orb}R_{\rm cyl}, \tag{3.1}$$

but give the atmosphere a velocity

$$v_\phi = \frac{f_{\rm cr}\Omega_{\rm orb}R_*^2\sin^2(\theta)}{R_{\rm cyl}}. \tag{3.2}$$

Here, $f_{\rm cr}$ is an adjustable parameter, ϕ is the azimuthal angle, θ is the polar angle, $\Omega_{\rm orb}$ is the orbital frequency of the red giant and companion, R_* is the radius of the giant, and $R_{\rm cyl}$ is the cylindrical radius from the rotation axis of the giant. We note that (3.1) and (3.2) ensure that the velocity is continuous at the surface of the giant.

Here, we run two simulations in which the giant is in different states of corotation, 95% corotation ($f_{cr} = 0.95$) and 0% corotation ($f_{cr} = 0$). We note that the 95% corotation case follows the simulations of Ohlmann et al. (2016a) and Ricker & Taam (2012). The choice to set f_{cr} to less than unity is also motivated by MacLeod et al. (2018) who found that orbital angular momentum lost by the companion prior to the onset of a common envelope phase does not necessarily go into spinning up the envelope, leading to a desynchronization between the orbital frequencies of the companion and envelope.

3.2 SIMULATION SETUP

We construct an appropriate particle mesh for the star from a pre-computed glass distribution. This is an unstructured distribution of 4096 points embedded within a cube of unit length, which we periodically replicate to produce a sufficient number of particles. It is important to begin with an unstructured distribution because it avoids degenerate faces and edges in the Voronoi tessellation and has no preferred directions. We assume that each particle is of equal mass and re-scale them to the appropriate radial position based on the computed $M(r)$ from MESA. These particles are also endowed with the radially-interpolated temperature and hydrogen fraction. The total number of particles representing the star is 3×10^5, which is smaller than the 2×10^6 particles used by Ohlmann et al. (2016a). Outside of the star, we include a low density atmosphere of 10^{-13} g cm^{-3} with temperature 10^5 K that extends out to the total box size of 3.5×10^{14} cm (5000 R$_\odot$), with periodic boundaries at its edges. The presence of the "hot vacuum" outside of the star is a necessity in grid codes to provide a pressure to the outer layers of the star, preventing them from overflowing stellar material into the surrounding cells (Iaconi et al., 2018). The total number of particles in the simulation is 8×10^5.

To lower the computational cost, we use a mesh refinement algorithm to decrease the number of gas particles in the atmosphere far from the star. We define a scale factor $\mathcal{S}(r) = (r/R_*)^k$ where R_* is the radius of the star, r is the spherical radius and k is an adjustable parameter which we have set to $k = 2/3$ in this case. Starting with the same uniform glass distribution as for the star, the linear spacing between particles is increased by $\mathcal{S}$ and their mass is increased by $\mathcal{S}^3$, preserving the external density. Because the simulation box has periodic boundary conditions at its edges, it would be problematic for the gravity solver if CEE outflows were to reach an edge of the box. Due to the refinement discussed above, the box can be extended arbitrary sizes without incurring significant computational cost. However, it should be noted that grid codes are not ideal for following outflows over long distances, as the mass and energy encountered by outflows due to the hot vacuum discussed above can become significant (Iaconi et al., 2018). Fortunately, this is only an issue for ejecta which has long since become unbound from the binary, and will not affect the analysis performed in this work.

3.3 INCLUSION OF RECOMBINATION ENERGY

The original implementation of MANGA described by Chang et al. (2017) used an ideal, adiabatic equation of state (EOS). In Prust & Chang (2019), we extended MANGA to use the equations of state implemented in MESA. The MESA equation of state relies on several equations of state relevant over the different regimes of stellar structure. See Paxton et al. (2011) – particularly their Fig. 1 – for a thorough description of the several EOSs used over various regions of ρ-T space. Improvements to the MESA equation of state are described by Paxton et al. (2013).

The interface between MANGA and MESA is accomplished via a wrapper written in Fortran 90 to call the MESA subroutines which interpolate the EOS tables. For each cell, the EOS is called once every step during the update of cell-centered variables. Gradient estimation and linear reconstruction are used to find the values of these variables on each cell interface. This avoids the need to call the EOS for every cell face, which would be computationally expensive as the average Voronoi cell has approximately 20 faces.

Besides the advantages of providing a more accurate physical model than the ideal gas EOS, the MESA EOS is particularly useful for the study of CEE since it allows us to account for recombination energy. As the envelope expands during CEE, plasma in the outer envelope cools and is expected to recombine into atoms, releasing its binding energy. Known as recombination energy, this is a potentially large energy source that may play significant role in ejecting the already tenuously-bound outer envelope (Lucy, 1967; Roxburgh, 1967; Paczyński & Ziółkowski, 1968). Care must be taken when considering the contribution of recombination to the energetics of CEE, as a stellar envelope contains enough recombination energy to unbind the entire envelope without the need for a companion. Obviously, single stars do not spontaneously eject their envelopes, so it is clear that recombination is only a useful source of energy under certain circumstances.

However, it is feasible that material which has already been thrown out from the stellar interior by the companion object could receive the "final push" to become unbound via recombination.

3.4 RESULTS

Starting with the above initial conditions, we simulate the binary for 240 days and show several density projections at $t = 1$, 10, 30, 75, 120 and 240 days in Figs. 3.2 and 3.3. We note that the simulation period is about 10 times the initial orbital period of 25 days.

In both simulations, the companion experiences an initial plunge into the envelope of the giant that lasts about 15 days, throwing off a large tidal tail (Figs. 3.2 and 3.3 upper center) and greatly decreasing the separation between the companion and core. The companions then continue to spiral in as their orbital energy is transferred to the gas; the spiral shocks facilitating this transfer can be seen in the projections (Figs. 3.2 and 3.3 upper right). We see smaller tidal tails thrown off at $t = 75$ days (lower left) and $t = 120$ days (lower center), as well as several others. The simulation ends well before the outflow reaches the edge of the simulation box.

3.4.1 Envelope Ejection

The total energy of each gas particle is given by

$$E_{\mathrm{tot,i}} = m_i[\frac{1}{2}(\boldsymbol{v}_i - \boldsymbol{v}_{\mathrm{CM}})^2 + \phi_i + I_{e,i}], \tag{3.3}$$

where m_i, $\boldsymbol{v}_i$, $\boldsymbol{v}_{\mathrm{CM}}$, ϕ_i and $I_{e,i}$ are the mass, velocity, center of mass velocity of the bound material, gravitational potential, and specific internal energy of each particle (Nandez et al., 2015). Gas particles with a negative total energy are bound to the binary, while

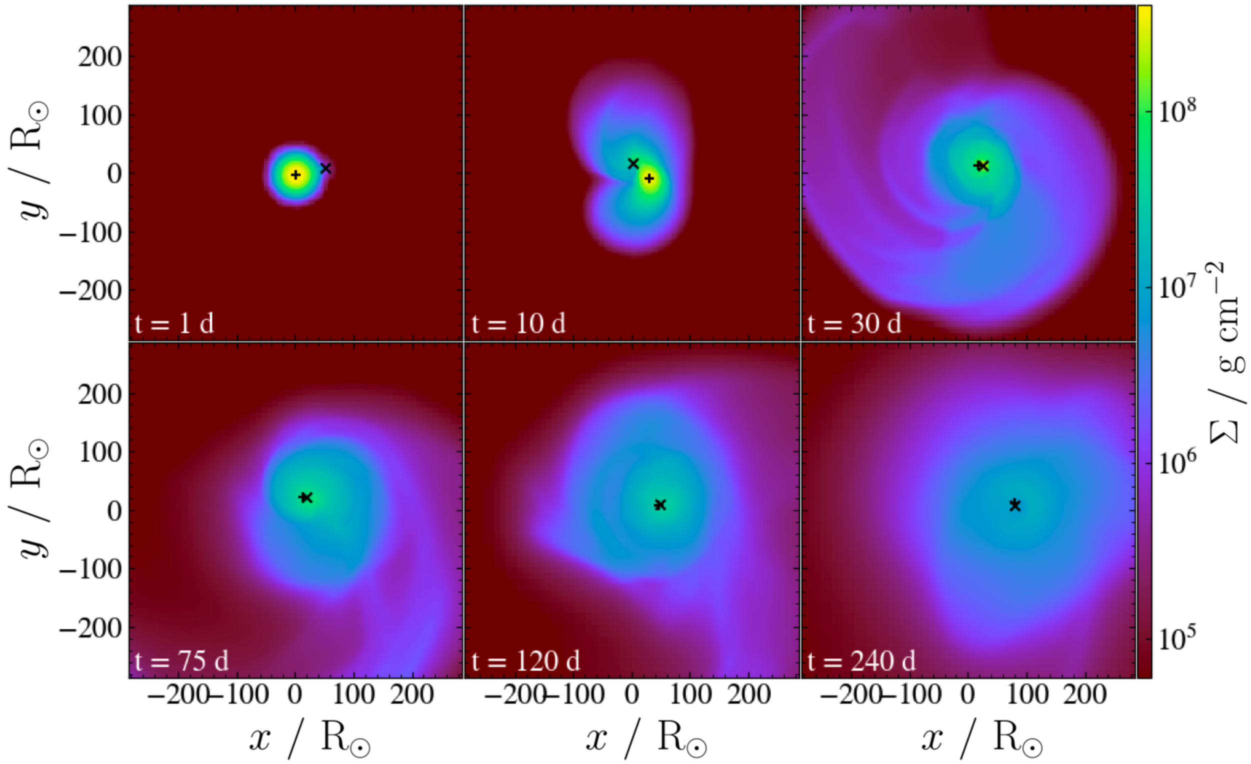

Figure 3.2: Density projections Σ in our CEE simulations with 95% corotation. The + sign marks the red giant core and the × marks the companion. We see gas ejected from the binary via tidal tails and spiral shocks as well as a decrease in the orbital separation to a small fraction of its initial value.

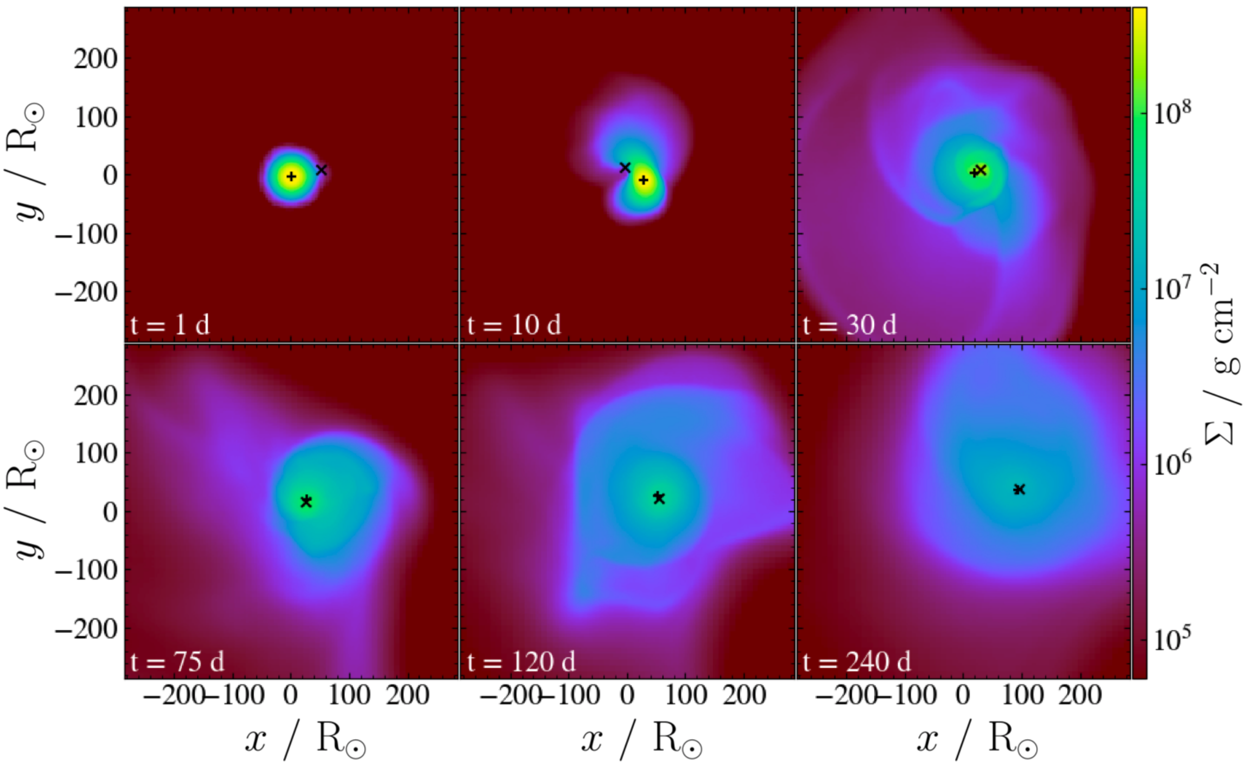

Figure 3.3: Same as Fig. 3.2 but neglecting initial rotation in the red giant.

those with a positive total energy are unbound. Fig. 3.4 shows a density slice in the $z = 0$ plane at $t = 15$ days in the 95% corotation case. The black contour encloses the matter bound to the binary.

The kinetic energy is computed relative to the velocity of the center of mass (CM) of the *bound* matter; that is, the bound gas as well as both dark matter particles. However, because the total energy is needed in order to determine which gas particles are bound, we used an iterative scheme to find the velocity of the CM.

1. The CM velocity is assumed to be zero.
2. The velocities of the gas particles are calculated relative to the CM velocity.
3. These velocities are used to find the kinetic energies of the gas particles, which are used to determine which particles are bound and which are not.
4. A new CM velocity $\boldsymbol{v}_{\rm CM}$ is found for everything *except* the unbound particles,

   $$\boldsymbol{v}_{\rm CM} = \frac{m_{\rm c,1}\boldsymbol{v}_1 + m_{\rm c,2}\boldsymbol{v}_2 + m_{\rm g,b}\boldsymbol{v}_{\rm g,b}}{m_{\rm c,1} + m_{\rm c,2} + m_{\rm g,b}}, \tag{3.4}$$

   where $m_{\rm c,1}$ and $m_{\rm c,2}$ denote the dark matter core and companion, $m_{\rm g,b}$ denotes the bound gas, and $m_{\rm c,1}\boldsymbol{v}_1$, $m_{\rm c,2}\boldsymbol{v}_2$, $m_{\rm g,b}\boldsymbol{v}_{\rm g,b}$ and $\boldsymbol{v}_1$, $\boldsymbol{v}_2$, $\boldsymbol{v}_{\rm g,b}$ are the momenta and velocities of the dark matter core, companion, and bound gas.
5. Steps 2 to 4 are repeated until $\boldsymbol{v}_{\rm CM}$ reaches convergence.

This is similar to the method of Guillochon & Ramirez-Ruiz (2013). With the total energies of all particles known, we can find the mass of the unbound gas as a fraction of the total mass of the envelope $m_{\rm env}$,

$$f_{\rm unb} = \frac{m_{\rm g,u}}{m_{\rm env}}, \tag{3.5}$$

which we refer to as the ejection efficiency. This is shown in Fig. 3.5. Qualitatively, the simulations are very similar in this regard. They show a large ejection of gas during the initial plunge as well as during the ejection of additional tidal tails. Unsurprisingly, the system set into corotation consistently exhibits a higher ejection efficiency owing to the inclusion of additional energy and angular momentum. We find that matter continues to be ejected up until the end of the simulation period, ending with an efficiency of 66% with corotation and 63% without.

We also show in Fig. 3.5 the ejection efficiency that would be obtained if the internal energies were neglected. We find that only 8% of the envelope is unbound in both the corotating and non-corotating cases, which is similar to the reported ejection efficiency in Ohlmann et al. (2016a). This dramatic difference in ejection efficiency indicates that the internal energy plays a major role in unbinding the envelope. Thus, should the envelope expand enough to lose energy rapidly by radiation, further work on CEE may not be able to ignore radiative cooling due to its possible large effects.

We can define a common envelope efficiency parameter using the energy formalism as in de Kool (1990):

$$\frac{m_1 m_{\rm env}}{\lambda R_1} = \alpha_{\rm CE}\left(-\frac{m_1 m_{\rm c,2}}{2a_{\rm i}} + \frac{m_{\rm c,1} m_{\rm c,2}}{2a_{\rm f}}\right), \tag{3.6}$$

where m_1 is the mass of the primary, R_1 is the radius of the primary, λ is a numerical factor of order unity that depends on the stellar structure, and $a_{\rm i}$ and $a_{\rm f}$ are the initial and final separations, respectively. Here $\alpha_{\rm CE}$ and λ are both uncertain, but Ivanova (2011) specifically notes that for a red giant star of mass $M \approx 2\ {\rm M}_\odot$ the numerical factor λ is well-approximated by $\lambda = 1$, which we adopt here. This allows us to obtain the values $\alpha_{\rm CE} = 2.01$ with corotation and $\alpha_{\rm CE} = 1.67$ without.

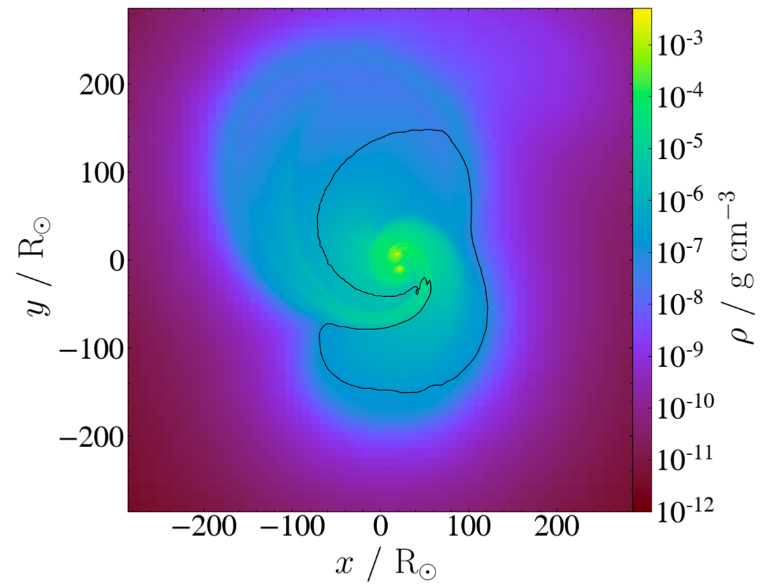

Figure 3.4: A density slice through the $z = 0$ plane at $t = 15$ days of the 95% corotation simulation. The black boundary encloses the gas that is bound to the binary, revealing an unbound tidal tail being ejected.

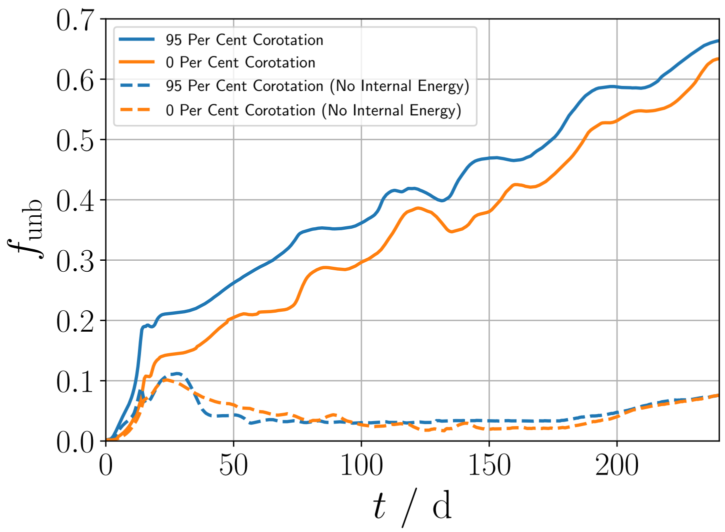

Figure 3.5: The fraction of mass of the envelope that has acquired enough energy to be unbound from the system. The large tidal tail thrown off in the initial plunge can be seen from 0 to 15 days, with several subsequent tails. A calculation of f_{unb} neglecting the internal energies is also shown (dashed lines).

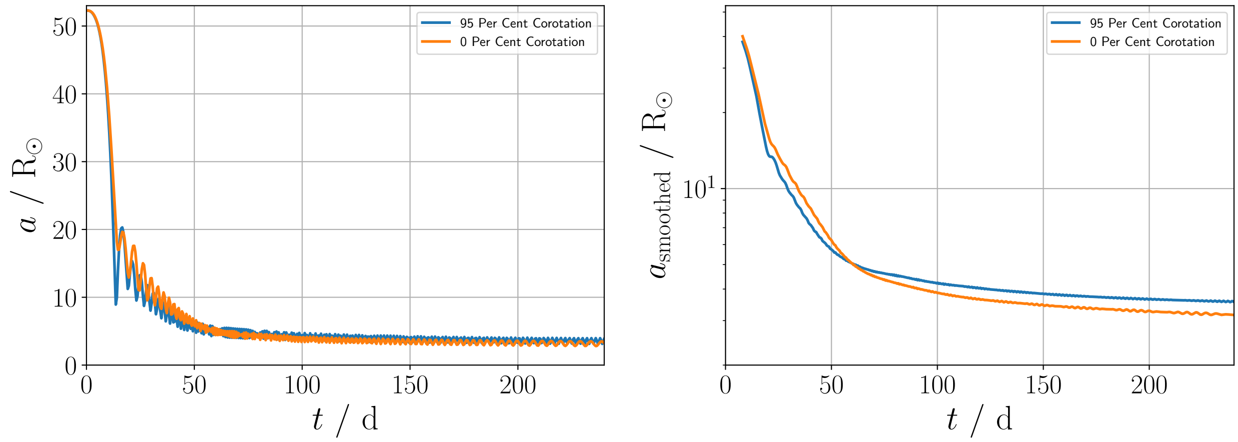

Figure 3.6: *(Left)* Separation a between the stellar core and companion in each case. *(Right)* The separations smoothed over time are shown on a logarithmic scale for ease of reading. Here we can see that the simulation without corotation results in a smaller separation by 0.4 R$_\odot$.

3.4.2 Orbital Parameters

The separations between the stellar core and companion are shown in Fig. 3.6. For ease of reading, we also show the separations on a logarithmic scale and smooth them over a period of 15 days. That is, each separation r_i is taken to be the average of all separations within an interval of 15 days centered on r_i.

After one orbit, both binaries have reduced their orbital separation to less than half the initial separation, and they continue to spiral in at a slower rate. Although the simulation with corotation initially falls to a smaller separation, it is eventually surpassed by its counterpart. The final (smoothed) separations are 3.6 R$_\odot$ with corotation and 3.2 R$_\odot$ with no corotation.

The eccentricity e can be found from the periapsis and apoapsis distances,

$$e = \frac{r_{\rm apo} - r_{\rm peri}}{r_{\rm apo} + r_{\rm peri}}, \tag{3.7}$$

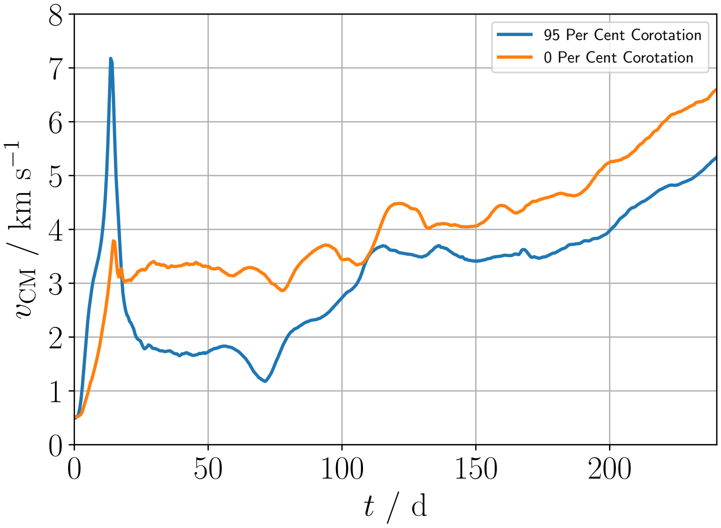

Figure 3.7: The velocity of the center of mass of the system v_{CM} over the simulation period. The simulation including corotation feels a large kick during the initial plunge but subsequent kicks quickly slow it to about 1 km s^{-1} less than its non-corotating counterpart.

where r_{apo} and r_{peri} denote the distances of closest and furthest approach. Here r_{apo} and r_{peri} are determined by interpolating the maxima and minima of the separation. The alert reader will notice that this definition is meaningful in this situation because the potential is not Keplerian owing to the distribution and nonaxisymmetry of the unbound gas. However, this method allows the determination of the eccentricity from only the orbital separations. Both binaries circularize their orbits over time, seeing drops in eccentricity from $e \approx 0.2$ down to $e = 0.1$ by the end of the simulation period.

In addition, each binary receives a kick velocity owing to the ejection of gas from the system, as shown in Fig. 3.7. Interestingly, although corotation results in a larger mass ejection and a large initial spike in CM velocity during the plunge, it quickly drops below the non-rotating case by about 1 km s^{-1}.

Table 3.1: Observed WD binaries with properties similar to our simulation results.

Name	$M_{\rm primary}$ (M$_\odot$)	$M_{\rm companion}$ (M$_\odot$)	a (R$_\odot$)
J0755+4800	0.409	0.89	3.07
J1151+5858	0.183	0.63	3.00
J1518+0658	0.224	0.60	2.84

3.4.3 Agreement with Observation

Our results can be linked to observations using surveys of binaries containing low-mass white dwarfs. Gianninas et al. (2014) have found systems with primary masses in the range of 0.18 to 0.41 M$_\odot$, consistent with the mass of our core, with companion masses $\geq$0.6 M$_\odot$ and separations of $\sim$3 R$_\odot$ (Table 3.1). These systems are consistent with our simulations, although the observed systems have ejected their envelopes, and it is not clear from our simulations whether the envelopes will be completely ejected and what the orbital parameters would be after ejection.

3.5 CONCLUSIONS

Our envelope ejection efficiencies are much larger than many of the results of previous work. However, three-dimensional numerical computations of CEE have found a wide variance in the ejection efficiency of the envelope. Early work (for example, de Kool, 1987; Livio & Soker, 1988; Terman et al., 1994; Sandquist et al., 1998, 2000; Terman et al., 1995; Rasio & Livio, 1996) on 3-D numerical simulations of CEE found envelope ejection efficiencies from about 10% to 80%. However, the resolutions of these early simulations were poor. More recent work (Passy et al., 2012; Ricker & Taam, 2012; Nandez et al., 2015; Ohlmann et al., 2016a) also find a large variance in the efficiencies (about 5% to 100%). For instance, Passy et al. (2012) found that only 15% of the mass was unbound in their simulations. Ricker & Taam (2012) found that about 25% of the mass is unbound, but the unbound mass is still rising at the end of their simulations (see their Fig. 9). Nandez et al. (2015) found that between 50% and 100% of the envelope mass is ejected in their simulations, depending on the inclusion of recombination energy. Ohlmann et al. (2016a) found that about 8% of the envelope mass is ejected. Our results are on the higher side and are similar to what Nandez et al. (2015) find. One difficulty in comparing these results is that the initial conditions and simulation parameters are not similar in these different groups. In this paper, we have adopted initial conditions and parameters similar to those used by Ohlmann et al. (2016a) but our results are dramatically different. The difference may be attributed to different simulation parameters such as the gravitational softening, the parameterization of the dark matter particle that represents the core of the red giant and the companion, or our inclusion of the recombination energy though the use of the MESA EOS.

Indeed, it has been suggested that inclusion of recombination energy would result in more efficient expulsion of the envelope (see the review by Ivanova, 2017). The first SPH simulations that included a realistic equation of state, using tabulated MESA tables, showed that the envelope is completely expelled during the radial plunge phase (Nandez & Ivanova, 2016). We should note, however, that these same simulations without recombination resulted in substantial expulsion of the envelope, making the problem significantly less difficult. We also note that this point is controversial, as Soker and collaborators have claimed in a series of papers (Sabach et al., 2017; Soker, 2017; Soker et al., 2018; Grichener et al., 2018) that the energy from recombination is easily transported away either by radiation or convection. However, Ivanova (2018) reached the opposite conclusion that the fraction of recombination energy transported away from the regions in which recombination takes place is negligible. The importance of radiative cooling in this case highlights the need for a more careful accounting of radiation effects in future calculations.

Our work here reinforces the results of Nandez et al. (2015), which suggests that the entire envelope of the red giant might be ejected during the plunge phase of CEE, or at least can be numerically simulated. Thus, the effects or relevance of the other phases of CEE such as the self-regulated spiral-in phase is unclear. It may be the case that these phases are important or relevant for different system parameters, though this requires a more detailed exploration of parameter space. The simulations of Law-Smith et al. (2020) find complete envelope ejection and the formation of a neutron star binary that will merge within 1 Gyr, though they consider a massive red supergiant, which differs markedly from the red giant we consider here.

Finally, we note here that other processes may also aid the expulsion of the envelope. Much recent work has focused on energy and momentum injection from jets produced by accretion onto the companion (Papish et al., 2015; Moreno Méndez et al., 2017; Soker, 2017; Shiber & Soker, 2018; Chamandy et al., 2018; López-Cámara et al., 2018). In addition, the transition from laminar flow to accretion flows around the companion star can be complicated and also provide another mechanism by which orbital energy is dissipated (MacLeod & Ramirez-Ruiz, 2015b,a; MacLeod et al., 2017a). Much of the work has focused on Bondi-Hoyle-Lyttleton type accretion around a point mass. However, a typical accretor has a physical scale on the order of a solar radius, which gives it a nontrivial cross-section in a red giant envelope. Typically, a 1 $R_\odot$ accretor encounters 10% to 50% of the envelope in one orbit. This hydrodynamic interaction may play a significant role in the evolution of the common envelope and the binary orbit. We also mention the suggestion that dust formation during CEE can drive winds to expel the envelope (Soker, 1994; Glanz & Perets, 2018).

3.6 FUTURE DIRECTIONS

3.6.1 Converting Simulation Results to Observables

The conversion from simulation results to observables is a relatively unexplored area, leading to a disjoint between theorists and observers. As discussed in section 1.4, intermediate luminosity optical transients (ILOTs) such as V838 Mon (Bond et al., 2003) and M85 OT2007 (Kulkarni et al., 2007) are thought to be common envelope events, but it is not clear whether their observed features align with numerical work on CEE. These transients are brighter than novae but dimmer than supernovae, and are very red. The light curves of ILOTs typically last roughly ten times the orbital period of the initial binary (MacLeod et al., 2017b), which is much shorter than the thermal or nuclear timescales and is consistent with our current understanding of the timescale of CEE.

Vinaya Valsan is now performing data analysis on my simulation results with the goal of obtaining light curves which could be compared with observations of ILOTs (Valsan et al., in preparation). The simulation output can be used to compute the location and temperature of the last scattering surface, assuming Thompson scattering. This 3-D map of the surface can then be integrated to find the luminosity and light curve of a simulated event, as shown in Fig. 3.8. The light curve exhibits an initial peak which lasts for the first 40 days; this is consistent with observed CEE light curves which typically last for several tens of days (Kulkarni et al., 2007; Kasliwal et al., 2011; Kasliwal, 2013). We also find a subsequent rise in luminosity over several hundred days, which is not present in optical observations of these events. However, we also see in Fig. 3.8 that the effective temperature during this rise is $\sim$2000 K, meaning that the emission peaks in the infrared. This is a potentially interesting prediction as there is a dearth of infrared data on these events. Matsumoto & Metzger (2022) also predict a second plateau which is powered by

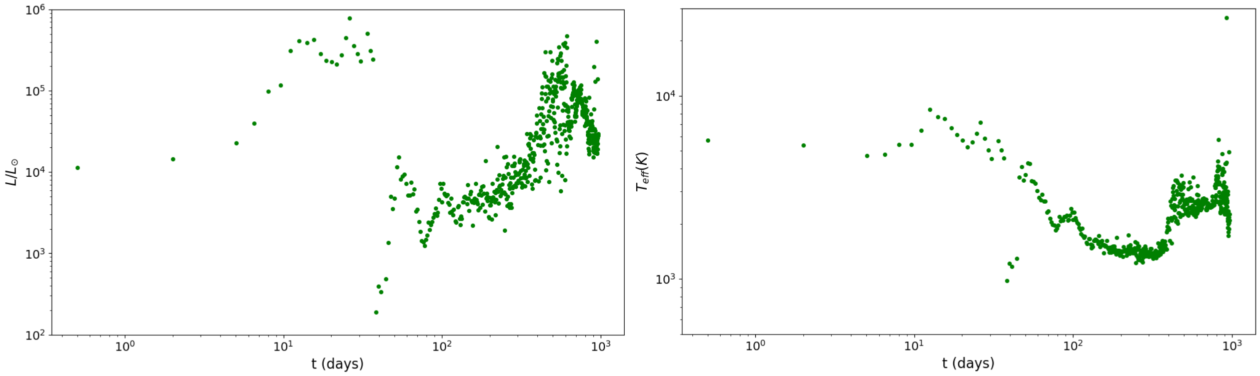

Figure 3.8: *(Left)* Light curve from a simulated CEE event. A swift rise and fall in luminosity occurs over the first 40 days, consistent with typical ILOT timescales. After several hundred days, the luminosity rises to a value rivaling that of the initial peak. *(Right)* Effective temperature of the last scattering surface for a simulated event, assuming Thompson scattering. At late times, the surface is at roughly 2000 K, indicating that the emission peaks in the infrared.

hydrogen recombination, though we find that it emerges regardless of the inclusion of recombination. We propose to expand on this work by predicting the light curves and spectra of CEE from simulated events by implementing realistic opacities. Rather than assuming Thompson scattering, MESA can be used to compute the opacities directly. It is also important to obtain the spectra of ILOTs to differentiate from other transients such as supernovae. This can be accomplished by use of the code TARDIS (Kerzendorf & Sim, 2014), which utilizes Monte Carlo methods to obtain synthetic spectra. Though TARDIS was originally developed with supernovae ejecta in mind, it requires as input only information which is already present in our simulation output. In addition to existing ILOT observations, the Rubin Observatory will provide more data with which to compare our results.

3.6.2 Radiation Hydrodynamics

Numerical simulations by a number of previous groups (Passy et al., 2012, for example) have found that only 5% to 25% of the envelope is ejected during CEE. This differs from the large implied values of ejection efficiency from observational studies, which suggests the existence of some additional energy not accounted for in the simulations. This changed with the SPH simulation of Nandez et al. (2015), who found that including hydrogen recombination energy leads to a complete ejection of the envelope and the formation of a clean double white dwarf binary. Indeed, we found in Prust & Chang (2019) that the inclusion of hydrogen recombination has a large effect on envelope ejection. However, as discussed above, it has been claimed that the energy from recombination is quickly lost to radiation (Sabach et al., 2017, for example). This suggests that the incorporation of radiation physics may be an important next step in modeling CEE.

Recently, a module has been added to MANGA that solves the equations of time-dependent radiative transfer using a reduced speed of light approximation (Chang et al., 2020) following the algorithm of Jiang et al. (2014). Specific radiative intensities are computed along discrete angles, and can be integrated to find energy and momentum source terms. The radiation is coupled to the fluid by including these source terms in the hydrodynamic equations. This differs from moment formalisms such as M1 and flux-limited diffusion, which introduce closure relations to solve the radiative transfer equations (González et al., 2007).

This radiation module has been successfully applied to several test cases including thermal equilibrium, a linear wave, the shadow test, and crossing beams of radiation (Fig. 3.9). The shadow test and crossing beams are of particular importance since they can produce qualitatively incorrect results based on the method of radiative transfer. For example, the M1 method when applied to the crossing beams test merges two beams

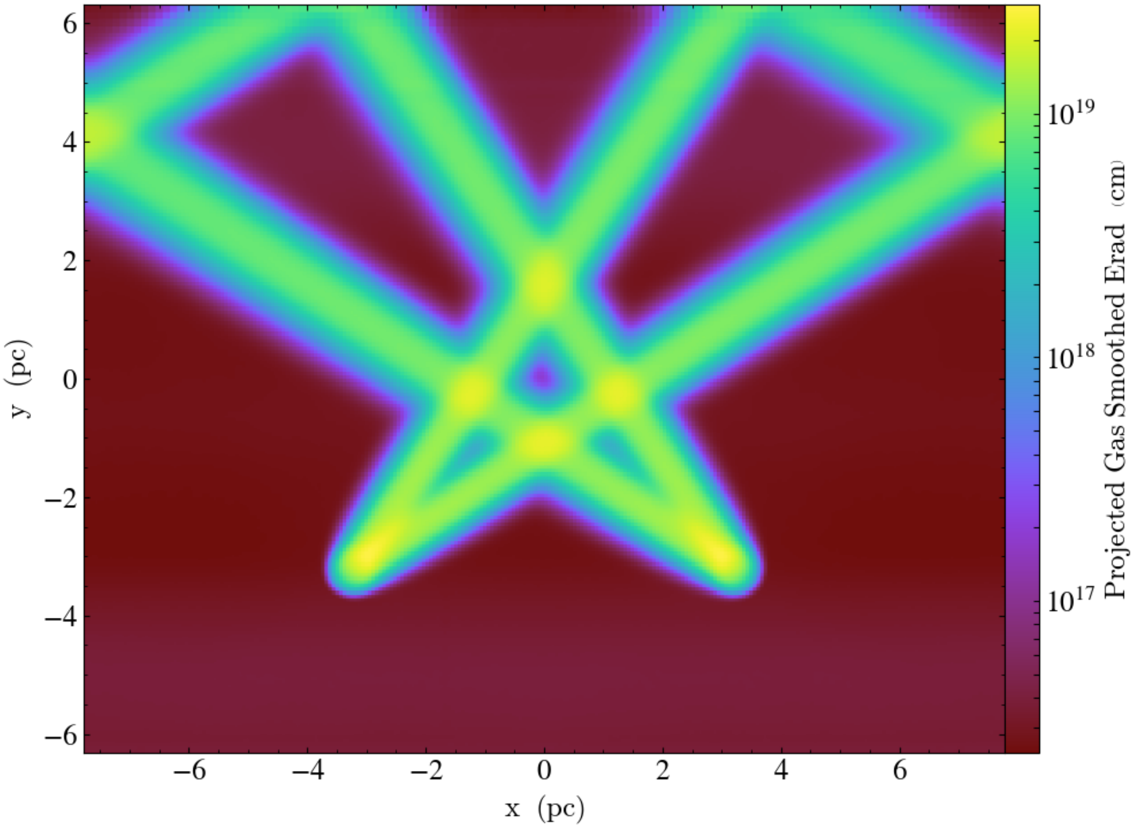

Figure 3.9: Radiation energy density in the crossing beam test of the MANGA radiation module in Chang et al. (2020). The beams of radiation pass through one another, in contrast to the merging beams seen in the M1 scheme. Periodic boundary conditions are used in the x and z directions, with an absorbing boundary placed at $y = 6.7$ pc.

of radiation at the point of intersection. In Fig. 3.9 we see the crossing beams test in MANGA. Here two sources of radiation create beams which pass through one another without interruption. Periodic boundary conditions are used in the x- and z-directions, and absorbing boundaries in the y-direction.

I plan to resolve the issue of radiative transfer in CEE by implementing the MANGA radiation module into my simulations. This will determine whether the energy from recombination is available to assist in the ejection of the envelope, or if it is quickly radiated away. Because the radiation module has been completed and tested on a moving mesh, its implementation into our CEE simulations should be straightforward; the only risk lies in the computational cost. Because of the high opacity near the center of giant stars, the inclusion of radiation limits the time-step to a small value.

Thus, I have implemented a radiation sub-cycling algorithm in which the radiation is evolved for several time-steps for each single step of the fluid, as in the algorithm of Kannan et al. (2019). Here the rungs (discussed in section 2.4.8) used for the fluid calculations are divorced from those used for radiation. For any rung higher than the maximum fluid rung, only the radiation is treated and the hydrodynamic and gravity solvers can be skipped as well as (perhaps most importantly) the Voronoi mesh computations. The reduction in computation time due to sub-cycling depends largely on the system in question; for a static box of gas at thermal equilibrium with isotropic radiation we find a reduction by a factor of $\sim$2.

The current radiation hydrodynamics module works well in optically thin to moderately optically thick environments, but does not perform well in extremely optically thick environments such as stellar centers. To that end, I also plan to develop an implicit radiation solver following the method recently developed by Jiang (2021). This solver will allow solutions in extremely optically thick environments with the standard (as opposed to a reduced) speed of light. It will also remove any time-step constraint related to the speed of light, further reducing computation times. Development of such a module will be useful for many radiation hydrodynamics problems including accretion disks, stellar mergers, and tidal disruption events.

CHAPTER 4

Moving Boundary Conditions

4.1 OVERVIEW

In fluid dynamics it is often desirable to set boundary conditions on a surface. For example, in modeling the flow around an airfoil, the edges of the simulation box can be treated as inflow or outflow boundaries and the airfoil itself as a reflective boundary, which allows no matter to pass through it. Indeed, Wan & Zhong (2019) use a 2-D ALE scheme with moving boundaries to model a pitching NACA 0012 airfoil. Immersed boundary methods can also be useful, especially when the relative displacement of the boundaries is large (Hedayat & Borazjani, 2019).

Such schemes are common in fields such as aerodynamics, but also have interesting and useful applications in astrophysics. For example, Chen et al. (2020) use two separate boundary conditions in their simulations of asymptotic-giant-branch (AGB) binaries using the adaptive mesh refinement code ASTROBEAR. On a cylindrical surface surrounding the binary, they set the fluid velocity to be supersonic in the radially outward direction, ensuring that no information propagates into the cylinder from the outside. They also set an inner boundary condition beneath the photosphere of the AGB star requiring that the radial fluid velocity oscillate in time, which approximates stellar pulsations (Bowen, 1988). Additionally, outflow conditions can be useful in astrophysical problems where accretion is present, such as in the growth of intermediate mass black holes in the early universe (for example, Toyouchi et al., 2019). However, due to the difficulty of implementing moving boundaries, such phenomena are typically modeled using static boundary conditions even in cases where moving boundaries are a more natural fit to the system in question.

The implementation of boundary conditions in Eulerian grid-based solvers, which we discuss in section 4.2, is straightforward. However, because Eulerian grid codes have a static mesh, it is at best very difficult to have a boundary which moves with respect to the mesh. This is compounded by difficulties in modeling a boundary of arbitrary shape. On a structured mesh the surface area elements will always point along the preferred axes, and this discretization can produce incorrect results for the surface area of a boundary (Yarza et al., 2022). For example, on a Cartesian mesh the volume of a spherical boundary will converge with increasing resolution to the correct value of $4\pi R^3/3$, but its surface area will converge to a value greater than $4\pi R^2$. On the other hand, moving-mesh codes are ideal for moving boundaries since the mesh-generating points can move with respect to one another and there are no preferred directions. In ALE schemes, the velocities of the mesh-generating points are typically taken to be equal or similar to the fluid velocity to gain the advantages offered by a Lagrangian scheme. However, the mesh-generating points can in principle move at any velocity relative to the fluid.

Springel (2010a) carried out a simple 2-D simulation using moving boundaries in AREPO in which a curved boundary (thought of as a "spoon") stirs a fluid. They generate their boundary using two sets of points on either side of and equidistant from the desired boundary surface (see their Fig. 38), on which they set reflective boundary conditions. They also require that both sets of points move together as a rigid body, and move their spoon at a constant speed along a pre-determined circular path. We adopt a similar strategy for our implementation of moving boundaries into MANGA, requiring the motion of the cells adjacent to the boundary to be identical to the motion of the boundary itself. However, we also set the velocity of the boundary such that its motion is reactive to external forces.

All CEE simulations to date have modeled the companion object as a dark matter particle, which interacts only gravitationally with the gas. While this may be appropriate in the case of a black hole companion, it is unclear how well it approximates a fluid body with a well-defined boundary such as a neutron star, white dwarf, or small star. In particular, stars have hydrodynamically relevant surfaces. As material accretes onto a star or just passes by it, it can create a shock, and this shock can backreact on the material. It is impractical numerically to model the companion star as a hydrostatically supported object. However, because of the great density contrast between the companion star and the extended envelope of the primary, the surface of the companion can instead be treated as a hard boundary. It is therefore desirable to model the companion as a moving, reflective boundary which interacts both gravitationally and hydrodynamically with the primary. To this end, we have implemented moving boundary conditions into MANGA in Prust (2020).

Moving-mesh codes, in contrast to Eulerian grid codes, naturally lend themselves to moving boundaries since the mesh-generating points can move with respect to one another. Moreover, the external forces acting on the boundary can be found by integration of the gas pressure and gravitational force over the surface and volume within the boundary, respectively. The motion of the boundary can then be made to react to these forces. We emphasize that studies of CEE to date have not accounted for hydrodynamic drag.

Previous studies of the drag experienced by a point particle companion have used a "common envelope wind tunnel" approach, which examines only the gas in the immediate vicinity of the companion (MacLeod & Ramirez-Ruiz, 2015a; MacLeod et al., 2017a; De et al., 2020). These simulations are able to capture the local properties of the flow near the companion with high resolution, and are ideal for exploring the parameter space of quantities such as mass ratio, adiabatic index, upstream Mach number and accretion coefficient, among others. In addition, these simulations are able to analyze both the dynamical friction and the drag from the accretion of linear momentum via a sink region (De et al., 2020). However, they are forced to make assumptions about the global evolution of the envelope.

On the other hand, Chamandy et al. (2019) investigate the drag force on a point particle companion in global CEE simulations by integrating the gravitational force of the entire envelope on the companion. In particular, they find that the torque on the companion is always positive in the non-inertial rest frame of the primary. That is, the binary never gains angular momentum from the gas. They also conclude that an additional source of drag is necessary in simulations of CEE in order for the results to match observations of post-common envelope systems.

4.2 HYDRODYNAMICS OF A MOVING BOUNDARY

Let us consider a face on which we would like to set a boundary condition and boost our state vectors and flux functions into the rest frame of the face. If we rotate the face such that its normal lies along the x-direction, as is done in MANGA, then we can write the flux normal to the face as

$$\boldsymbol{\mathcal{F}}_x = (\rho v_x,\ \rho v_x^2 + P,\ \rho v_x v_y,\ \rho v_x v_z,\ (\rho e + P) v_x). \tag{4.1}$$

Here we have expanded the momentum flux tensor $\rho \boldsymbol{v}\boldsymbol{v}^T$ into its three components. The flux of mass, momentum and energy that pass through the face are determined by the values of the state vector $\boldsymbol{\mathcal{U}}_{\rm L}$, $\boldsymbol{\mathcal{U}}_{\rm R}$ and the flux function $\boldsymbol{\mathcal{F}}_{x,{\rm L}}$, $\boldsymbol{\mathcal{F}}_{x,{\rm R}}$ on either side of the face. We see that under the transformation $v_x \to -v_x$ all terms in $\boldsymbol{\mathcal{F}}_x$ change sign with the exception of the x-momentum flux $\rho v_x^2 + P$. Conversely, when this transformation is applied to the state vector $\boldsymbol{\mathcal{U}} = (\rho, \rho v_x, \rho v_y, \rho v_z, \rho e)$, the *only* term that changes sign is the

x-momentum ρv_x. Consider now the HLL approximate Riemann solver (Einfeldt, 1988), which computes the flux across the face as

$$\hat{\boldsymbol{F}}_{\rm HLL} = \frac{\alpha_+ \boldsymbol{\mathcal{F}}_{x,{\rm L}} + \alpha_- \boldsymbol{\mathcal{F}}_{x,{\rm R}} - \alpha_+ \alpha_- (\boldsymbol{\mathcal{U}}_{\rm R} - \boldsymbol{\mathcal{U}}_L)}{\alpha_+ + \alpha_-}, \tag{4.2}$$

where $\alpha_\pm = \max[0, \pm\lambda_\pm(\boldsymbol{\mathcal{U}}_{\rm L}), \pm\lambda_\pm(\boldsymbol{\mathcal{U}}_{\rm R})]$, the maximum and minimum eigenvalues of the Jacobians of each state are $\lambda_\pm = v_x \pm c_{\rm s}$, and $c_{\rm s}$ is the sound speed. We now impose the condition that the state vector and flux on either side are equal except for the fluid velocities normal to the face, which are opposite: $v_x = v_{x,{\rm L}} = -v_{x,{\rm R}}$. That is,

$$\boldsymbol{\mathcal{F}}_{x,{\rm R}}(v_x) = \boldsymbol{\mathcal{F}}_{x,{\rm L}}(-v_x) \quad \text{and} \quad \boldsymbol{\mathcal{U}}_{\rm R}(v_x) = \boldsymbol{\mathcal{U}}_{\rm L}(-v_x). \tag{4.3}$$

This implies $\alpha_+ = \alpha_- = c_{\rm s} + |v_x|$ and simplifies the HLL flux to the form

$$\hat{\boldsymbol{F}}_{\rm HLL} = \frac{\boldsymbol{\mathcal{F}}_{x,{\rm L}}(v_x) + \boldsymbol{\mathcal{F}}_{x,{\rm L}}(-v_x) - \alpha_+[\boldsymbol{\mathcal{U}}_{\rm L}(-v_x) - \boldsymbol{\mathcal{U}}_{\rm L}(v_x)]}{2}. \tag{4.4}$$

If we now plug in $\boldsymbol{\mathcal{F}}$ and $\boldsymbol{\mathcal{U}}$ in component form as in (4.1), we obtain

$$\hat{\boldsymbol{F}}_{\rm HLL} = (0,\ \rho v_x^2 + P + \rho v_x(c_{\rm s} + |v_x|),\ 0,\ 0,\ 0). \tag{4.5}$$

We see that all terms in $\hat{\boldsymbol{F}}_{\rm HLL}$ vanish except for the term corresponding to the flux of x-momentum – that is, the component of momentum normal to the face. Thus, the reflective boundary condition (4.3) prevents the transport of any quantity besides momentum normal to the face for the HLL Riemann solver; mass, energy and entropy cannot be transported. This momentum flux corresponds to the contact pressure exerted on the face. The derivation for the HLLC solver (Toro et al., 1994) proceeds in a similar fashion. The implementation of reflective boundary conditions requires modifications to the Riemann solver

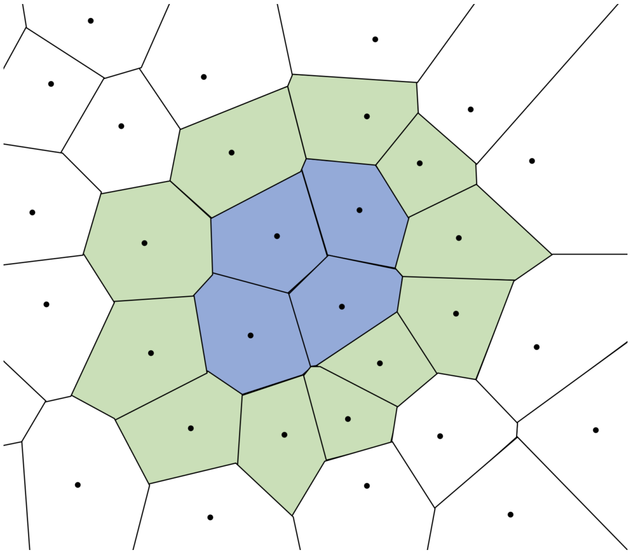

Figure 4.1: Illustration of a moving boundary on a Voronoi mesh. The boundary cells (blue) are defined at the start of the simulation, and any cell sharing a face with a boundary cell is designated as an edge cell (green). Reflective boundary conditions are implemented at the faces between blue and green cells. All other gas cells (white) function normally.

and – for schemes that are accurate to second order or higher in space – the gradient estimation, both of which are discussed below. The alternate condition $\boldsymbol{\mathcal{F}}_{x,\mathrm{L}}(v_x) = \boldsymbol{\mathcal{F}}_{x,\mathrm{R}}(v_x)$ and $\boldsymbol{\mathcal{U}}_{x,\mathrm{L}}(v_x) = \boldsymbol{\mathcal{U}}_{x,\mathrm{R}}(v_x)$ corresponds to an outflow boundary condition. However, we focus on reflective conditions in this paper for the reason that inflow or outflow conditions in a moving-mesh code would necessitate the creation or destruction of mesh-generating points, which are not yet implemented in MANGA. A separate publication (Chang et al., 2020) details the development of inflow and outflow conditions for radiation, which is applicable to fluids on a static mesh.

4.3 IMPLEMENTATION INTO MANGA

4.3.1 Initialization

In the initialization step at the beginning of the simulation, we declare some user-specified region as the initial boundary. Cells with centers within this region are defined to be a part of the boundary. We will refer to these cells as "boundary cells" and to all other cells as "gas cells" (see Fig. 4.1). The boundary cells will comprise the boundary for the entirety of the simulation, as boundary cells are never added or removed. We define the boundary particles to have equal mass so that the density of the boundary is constant, provided that the density of mesh-generating points is constant within the boundary. The total mass of the boundary is an input parameter in our simulations.

To accurately produce the desired boundary shape, it is necessary to have a sufficiently high density of mesh-generating points near the edges of the boundary. To this end, it is sometimes beneficial to initialize the simulation with a larger resolution in the region containing the boundary than in the rest of the simulation box. We demonstrate this in section 4.5. In principle, a boundary of arbitrary shape can be constructed given a sufficiently high density of mesh-generating points.

4.3.2 Edge Cells

We define all gas cells which share a face with a boundary cell as "edge cells." These cells function as normal gas cells for the most part; however, the motion of their mesh-generating points always matches that of the boundary. The result of this is a layer of gas cells which do not move with respect to the boundary, as in Springel (2010a). This is important because the surface of the boundary is comprised of the shared faces between the edge cells and boundary cells, which we refer to as "boundary faces." The boundary faces are redrawn with every Voronoi computation, which happens several times during each time-step. Therefore, if the mesh-generating points were allowed to flow past the boundary, the surface of the boundary would deform, which is undesirable. Although the edge cells are the only gas cells which have direct contact with the boundary, they communicate its effects to the rest of the gas through their properties and motion.

4.3.3 Gradient Estimation and Linear Reconstruction

As discussed in section 2.4.3, the state vector on the face between the ith cell and its jth neighbor is

$$\tilde{\boldsymbol{\mathcal{U}}}_{ij} = \boldsymbol{\mathcal{U}}_i + (\tilde{\boldsymbol{r}}_{ij} - \boldsymbol{c}_i) \cdot \boldsymbol{\nabla} \boldsymbol{\mathcal{U}}_i. \tag{4.6}$$

These gradients are calculated following the procedure of Steinberg et al. (2016).

We modify the gradient estimation algorithm for edge cells by modifying the properties of their neighboring boundary cells. Consider an edge cell with state vector $\boldsymbol{\mathcal{U}}_i$, fluid velocity $\boldsymbol{v}_i$ and neighbors with states $\boldsymbol{\mathcal{U}}_j$, where the normal vectors of the faces shared with its neighbors are $\hat{\boldsymbol{n}}_{ij}$. For each boundary cell neighbor, we first copy the state vector of the edge cell into the boundary cell ($\boldsymbol{\mathcal{U}}_j = \boldsymbol{\mathcal{U}}_i$). We then modify $\boldsymbol{\mathcal{U}}_j$ such that the component of its fluid velocity $\boldsymbol{v}_j$ normal to the shared face is equal and opposite to $\boldsymbol{v}_i$. That is,

$$\boldsymbol{v}_j = \boldsymbol{v}_i - 2(\hat{\boldsymbol{n}}_{ij} \cdot \boldsymbol{v}_i)\hat{\boldsymbol{n}}_{ij}, \tag{4.7}$$

which enforces the condition (4.3) for reflective boundary conditions. We also modify the slope limiter in the presence of a boundary. MANGA uses a slope limiter

$$\langle \nabla \boldsymbol{\mathcal{U}} \rangle_i^{DM} = \alpha_i^{DM} \langle \nabla \boldsymbol{\mathcal{U}} \rangle_i^{S10}, \tag{4.8}$$

where

$$\alpha_i^{DM} = \min(1, \psi'_{ij}). \tag{4.9}$$

Here,

$$\psi'_{ij} = \begin{cases} \max[\theta(\boldsymbol{\mathcal{U}}_j - \boldsymbol{\mathcal{U}}_i)/\Delta\boldsymbol{\mathcal{U}}_{ij}, 1] & |\Delta\boldsymbol{\mathcal{U}}_{ij}| > 0, \\ 1 & \text{otherwise.} \end{cases} \tag{4.10}$$

For all simulations presented in this chapter, we use $\theta = 0.49$. However, when performing a reconstruction on a face between an edge cell and a boundary cell we set $\theta = 0$, effectively turning off this additional slope limiter. We find that this marginally improves the conservation properties of our simulations and the stability of the code.

4.3.4 Time-Stepping

In Chapter 2, we discuss the implementation of individual time-steps into MANGA. When a moving boundary is present, we place the boundary and edge cells on the highest rung (smallest time-step) of all cells present. Besides improving the stability of the code, this mitigates the risk of gas cells penetrating into the boundary or other pathological behaviors. Because the number of edge cells is typically small relative to the total number of cells, we find that this does not substantially slow down the simulation code.

4.3.5 Riemann Solver

MANGA uses either an HLLC or HLL approximate Riemann solver to estimate the the flux through each face of a cell at the half time-step. We have made several modifications to the Riemann solver in the presence of a boundary.

1. A Riemann solution is not performed for boundary cells. Because the state vector $\boldsymbol{\mathcal{U}}$ of a boundary cell is determined by those of its neighbors, as described in section 4.3.3, there is no need to compute the time rate of change of the boundary cell charges.

2. For boundary faces, we modify the state vector $\boldsymbol{\mathcal{U}}$ as well as the flux function $\boldsymbol{\mathcal{F}}$ inside of the boundary cell according to (4.3). The reconstruction gives the states on either side of the boundary face in the edge cell and boundary cell $\boldsymbol{\mathcal{U}}_{\rm e}, \boldsymbol{\mathcal{U}}_{\rm b}$ as well as the flux functions $\boldsymbol{\mathcal{F}}_{\rm e}$, $\boldsymbol{\mathcal{F}}_{\rm b}$. We rotate these such that the normal direction to the face lies along the x-direction. To enforce reflective boundary conditions, we ignore the $\boldsymbol{\mathcal{U}}_{\rm b}$ and $\boldsymbol{\mathcal{F}}_{\rm b}$ given by the reconstruction and instead set them using condition (4.3). Denoting the (rotated) x-velocity in the edge cell as $v_{x,{\rm e}}$, we require

   $$\boldsymbol{\mathcal{U}}_{\rm b} = \boldsymbol{\mathcal{U}}_{\rm e}(-v_{x,{\rm e}}) \quad \text{and} \quad \boldsymbol{\mathcal{F}}_{\rm b} = \boldsymbol{\mathcal{F}}_{\rm e}(-v_{x,{\rm e}}). \tag{4.11}$$

   The new $\boldsymbol{\mathcal{U}}_{\rm b}$ and $\boldsymbol{\mathcal{F}}_{\rm b}$ along with $\boldsymbol{\mathcal{U}}_{\rm e}$ and $\boldsymbol{\mathcal{F}}_{\rm e}$ are then used by the Riemann solver to estimate the flux $\hat{\boldsymbol{F}}$ across the face, and the result is used in equation (2.19) to evolve the charges in time.

3. The contact pressure $P_{\rm con}$ at each boundary face, computed by the Riemann solver

as in (4.5), is given by

$$P_{\text{con}} = \bar{P} - \frac{1}{2}\hat{\boldsymbol{n}} \cdot (\boldsymbol{v}_{\text{b}} - \boldsymbol{v}_{\text{e}})\bar{\rho}\bar{c}_{\text{s}} + \begin{cases} 0 & \hat{\boldsymbol{n}} \cdot \boldsymbol{v}_{\text{e}} \leq 0 \\ 2\bar{\rho}(\hat{\boldsymbol{n}} \cdot \boldsymbol{v}_{\text{e}})^2 & \hat{\boldsymbol{n}} \cdot \boldsymbol{v}_{\text{e}} > 0, \end{cases} \tag{4.12}$$

with the condition that the contact pressure must be non-negative. Here P, $\hat{\boldsymbol{n}}$, ρ, c_{s}, are the pressure, normal to the face in the direction of the boundary cell, density and sound speed. The bar denotes an average of the values on each side of the face which are obtained from the state vectors $\boldsymbol{\mathcal{U}}_{\text{e}}$ and $\boldsymbol{\mathcal{U}}_{\text{b}}$. For a face with area A, this results in a hydrodynamic force

$$\boldsymbol{F}_{\text{hy}} = \hat{\boldsymbol{n}} A P_{\text{con}} \tag{4.13}$$

at the face. We sum all such forces at boundary faces to find the total hydrodynamic force on the boundary.

4.3.6 Gravity Solver

As discussed in section 2.4.6, MANGA uses a tree-based gravity solver originally implemented in GASOLINE which uses multipole moments up to fourth order (hexadecapole) to represent the mass distribution within cells at each level of the tree (Wadsley et al., 2004b). After a gravity solution is performed, we intercept the gravitational accelerations $\boldsymbol{a}_i$ on all boundary particles and average them to find the gravitational acceleration of the boundary $\boldsymbol{a}_{\text{gr}}$. All gas cells have equal softening length, defined at the start of the simulation. We require boundary cells to have this same softening length, which guarantees that the self-gravity of the boundary does not impact its motion.

4.3.7 Motion of Boundary

The motion of our boundaries is reactive to both hydrodynamic and gravitational forces. The hydrodynamic force is calculated during the half time-step Riemann solution, and is the sum of all forces on the boundary faces (4.13). For a boundary with mass $m_{\rm b}$, this results in an acceleration

$$\boldsymbol{a}_{\rm hy} = \frac{1}{m_{\rm b}} \sum_j \hat{\boldsymbol{n}}_j A_j P_{{\rm con},j}. \tag{4.14}$$

We combine this with $\boldsymbol{a}_{\rm gr}$ to get the total acceleration of the boundary

$$\boldsymbol{a}_{\rm b} = \boldsymbol{a}_{\rm gr} + \boldsymbol{a}_{\rm hy}. \tag{4.15}$$

At the drift step, the boundary velocity kick

$$\Delta \boldsymbol{v}_{\rm b} = \boldsymbol{a}_{\rm b} \Delta t \tag{4.16}$$

is used to update the velocities of all boundary and edge cells. Unlike normal gas cells, the boundary and edge cells do not receive kicks in the direction of the fluid velocity nor the velocity corrections described in Chang et al. (2017).

4.4 TEST CASES

4.4.1 Supersonic Wind

We begin by simulating a sphere moving through air at supersonic speed. The air is initialized with atmospheric conditions $\rho = 0.001225$ g cm^{-3}, $T = 288$ K, $\gamma = 1.4$ and mean molecular weight $\mu = 29$ g/mol. Our simulation box has dimensions (10, 6, 6) cm

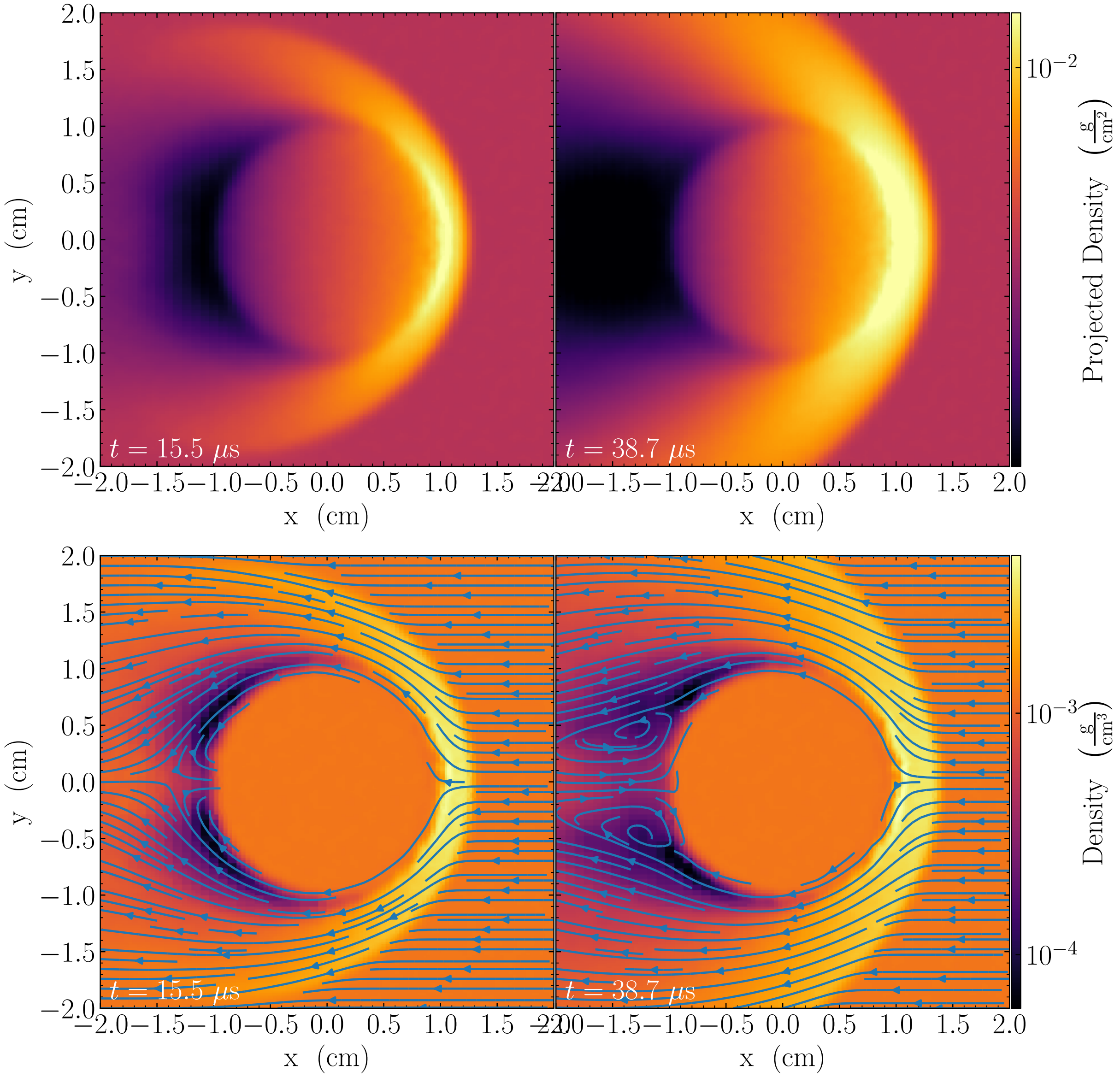

Figure 4.2: The supersonic wind test case at $t = 15.5\ \mu$s *(left)* and $t = 38.7\ \mu$s *(right)*. *(Top)* Density projections along the z-axis, showing the bow shock as it strengthens and detaches from the sphere. *(Bottom)* Density slices through the $z = 0$ plane with streamlines. Here, the stagnation point and vortices are visible.

and our spherical boundary has a radius of 1 cm. We use an HLLC Riemann solver for this test and do not include gravity. For all simulations presented in this chapter, we use an adiabatic ideal gas equation of state.

We initialize the positions of our mesh-generating points using a pre-computed glass distribution. Low spatial resolution is problematic for this test case as large mesh cells cause the surface of the boundary to be rough and jagged, which can eventually lead to unphysical values for the state vector $\boldsymbol{\mathcal{U}}$. In fact, we find in all test cases that the stability of the code depends largely on the smoothness of the boundary surface. When the boundary surface is well-resolved, we find that our code is robust against unphysical results, even in extreme situations. For this test case, our simulation contains 1.5×10^6 gas and 1.7×10^4 boundary cells.

Our boundary moves through the air with Mach number $M = 2$, shown in Fig. 4.2. The top left panel shows a density projection at $t = 15.5$ μs, where we can see the formation of a bow shock as it detaches from the sphere. The bottom left panel shows a density slice through the $z = 0$ plane overplotted with streamlines, where we see turning of the streamlines across the shock as well as a stagnation point behind the boundary. In the panels on the right, we show the same plots at $t = 38.7$ μs. Here the shock has strengthened and we see a void in the path cleared by the sphere. In addition, the turbulence behind the boundary has now evolved into vortices. Qualitatively, these are the results that one would expect from this test case. This is encouraging, as the problem of an object moving through a dense gas appears in many astrophysical settings.

Our implementation goes one step beyond Prust (2020) by altering the mesh motion of cells in the vicinity of the boundary. Because the edge cells move with a velocity equal to that of the boundary, $\boldsymbol{v}_{\mathrm{b}}$, they often move with high velocity relative to the neighboring gas cells. This can be problematic for two reasons:

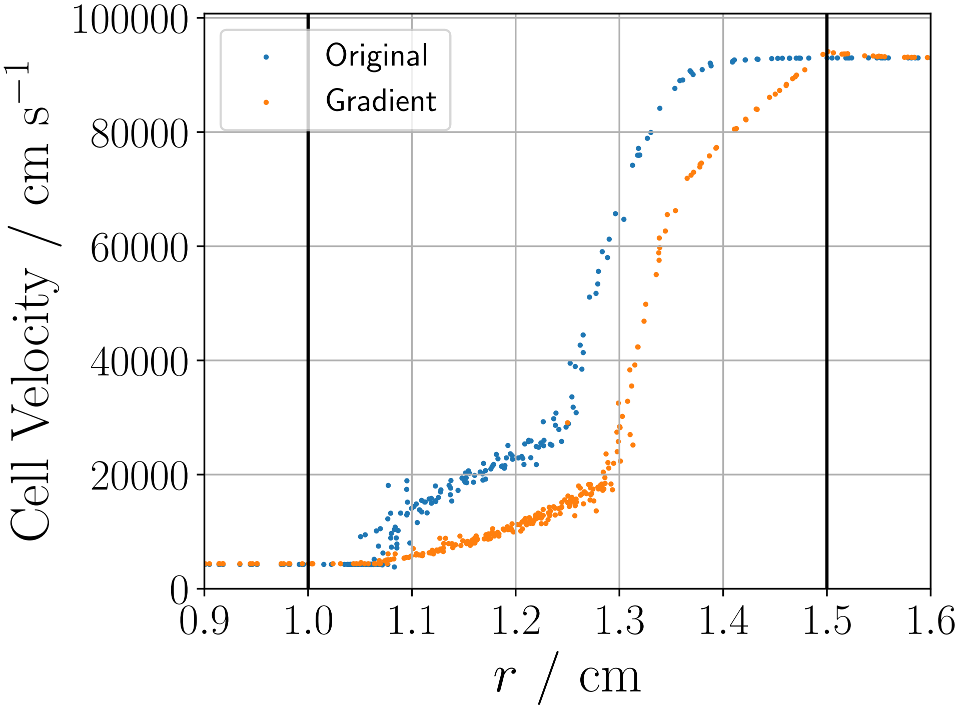

Figure 4.3: Velocities of the mesh-generating points in the supersonic wind tunnel test using the original implementation (blue dots) as well as the new gradient of velocities (orange dots). The black lines mark the locations of the boundary radius at $R_{\mathrm{b}} = 1$ cm and the outer radius of the shell at $R_{\mathrm{s}} = 1.5$ cm. The cell velocity varies between the boundary velocity $\boldsymbol{v}_{\mathrm{b}}$ on the left and the freestream velocity on the right. The distribution is smoother for the new implementation, minimizing relative velocities between cells.

1. The advantages offered by a Lagrangian scheme are forfeited.
2. Inconsistencies between the changes in cell volume assumed by the hydrodynamic calculations and the actual volume changes can lead to errors in the flux computations, as described by Steinberg et al. (2016).

To combat this, mesh-generating points near the boundary move with a velocity that grows from the boundary velocity $\boldsymbol{v}_\mathrm{b}$ for cells near the boundary to the fluid velocity $\boldsymbol{v}_i$ for cells far away. This effectively slows the mesh motion near the boundary, reducing volume inconsistency errors. For a spherical boundary with radius R_b, this takes the form

$$\boldsymbol{v}(r) = \frac{r - R_\mathrm{b}}{R_\mathrm{s} - R_\mathrm{b}}\boldsymbol{v}_i + \frac{R_\mathrm{s} - r}{R_\mathrm{s} - R_\mathrm{b}}\boldsymbol{v}_\mathrm{b} \tag{4.17}$$

within a spherical shell with outer radius R_s, where r is the distance between the centers of the fluid cell and boundary. Note that this satisfies $\boldsymbol{v}(R_\mathrm{b}) = \boldsymbol{v}_\mathrm{b}$ and $\boldsymbol{v}(R_\mathrm{s}) = \boldsymbol{v}_i$. For $r > R_\mathrm{s}$, the velocity is determined as usual by the fluid velocity as well as the corrections described in Chang et al. (2017).

We have repeated the supersonic wind tunnel test with the new gradient of velocities and $R_\mathrm{s} = 1.5$ cm. The velocities of the mesh-generating points along a radial slice at $t = 15.5\ \mu s$ are shown in Fig. 4.3 (blue dots) along with the previous results (orange dots). The boundary radius at $R_\mathrm{b} = 1$ cm and the outer radius of the shell at $R_\mathrm{s} = 1.5$ cm are shown as solid black lines. In both cases, the cell velocity grows from $\boldsymbol{v}_\mathrm{b}$ to the freestream velocity. We see that the new method results in a smoother distribution of cell velocities, and thus a reduction in relative velocities between the cells.

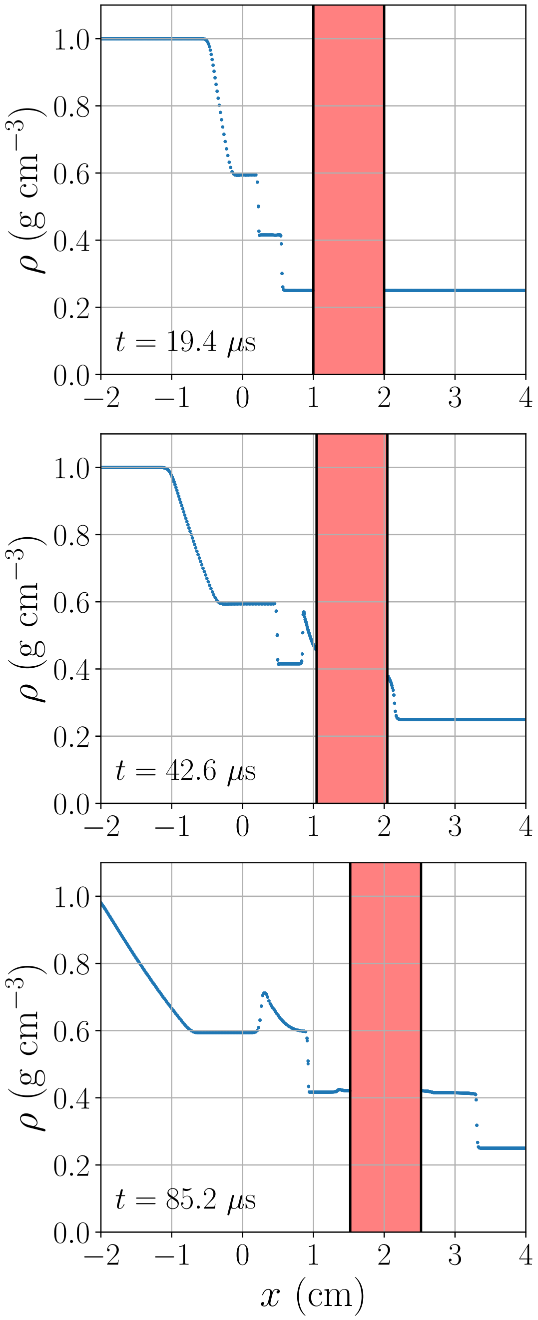

Figure 4.4: Gas density in our Sod shock tube test at $t = 19.4$, 42.6 and 85.2 μs. *(Top)* We initially see a shock front propagating to the right, followed by a contact discontinuity, as well as an expanding rarefaction wave. *(Middle)* The shock front then collides with the piston (shaded in red) and reflects back to the left. *(Bottom)* The piston is pushed to the right, creating a transmitted shock; the reflected shock passes the contact discontinuity.

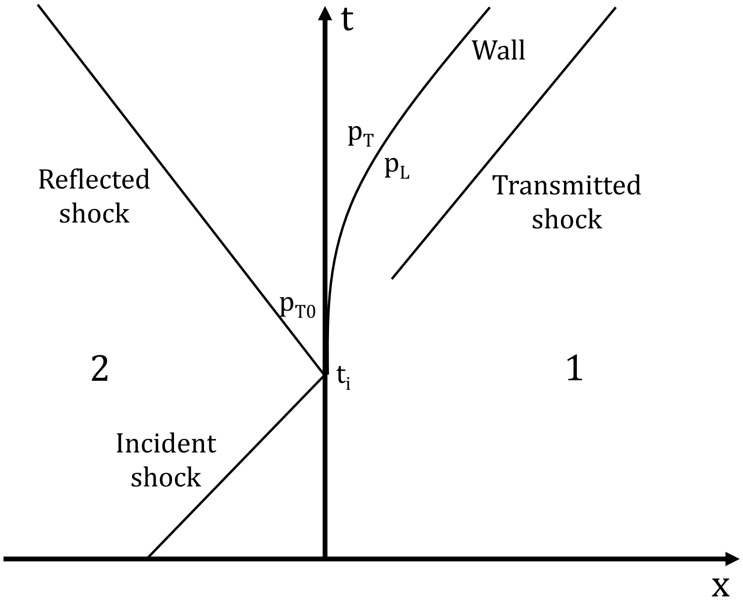

Figure 4.5: Wave diagram showing the paths of the wall and shock waves. The regions 1 and 2, which denote the states on the right and left sides of the wall before disruption by the transmitted or reflected shocks, are shown as well as the pressures relevant to (4.18).

4.4.2 Sod Shock Tube with Piston

We now perform a Sod shock tube test using a simulation box of dimension (16, 1, 1) cm centered at (0, 0, 0). On the left side of the box $(x < 0)$, the gas has density $\rho = 1$ g cm^{-3} and temperature $T = 2.5$ K, while the right side $(x \geq 0)$ has $\rho = 0.25$ g cm^{-3} and $T = 1.8$ K. The gas is initially stationary $(\boldsymbol{v} = 0)$ with $\gamma = 1.4$. We use a periodic simulation box, so the shock propagates through the tube in both directions. These conditions are similar to those used by Chang et al. (2017) to validate MANGA. We choose our moving boundary to be a piston of mass $m = 0.1$ g (1% of the mass of the gas in the tube) that extends from $x = 1$ cm to $x = 2$ cm and spans the tube in the y- and z-directions. The piston is free to move but is initially at rest. We use a rectangular mesh – an appropriate choice because of our rectangular piston – with 160 cells in the x-direction and 10 cells in the y- and z-directions, for a total of 16,000 cells.

In Fig. 4.4, we show the density as a function of position at $t = 19.4$, 42.6 and 85.2 μs. We initially see the formation of the shock front, contact discontinuity, and rarefaction wave. At $t = 34.8$ μs, the shock front impacts the piston (shaded in red) and reflects back to the left. This impact also pushes the piston to the right, inducing a transmitted shock.

We validate the motion of the piston using an analytical result for the impact of a shock wave on a movable wall. Following Meyer (1957), the motion of the wall is described by

$$\frac{du_\mathrm{w}}{dt} = \frac{p_\mathrm{T} - p_\mathrm{L}}{p_\mathrm{T0} - p_1} \left(\frac{du_\mathrm{w}}{dt} \right)_{t=t_\mathrm{i}} . \tag{4.18}$$

Here u_w is the wall velocity, p is the gas pressure and t_i is the time of shock impact. The subscripts L and T correspond to the leading and trailing edges of the wall (Fig. 4.5). The regions 1 and 2 are the states on the right and left sides of the wall before disruption by the transmitted or reflected shocks. Furthermore, p_T0 is the pressure on the trailing edge just after shock reflection. We use the isentropic relations as well as the Riemann invariants

$$P = \frac{2}{\gamma - 1} c_\mathrm{s} + v \quad \text{and} \quad Q = \frac{2}{\gamma - 1} c_\mathrm{s} - v \tag{4.19}$$

to obtain the relations

$$p_\mathrm{L} = p_1 \left(\frac{Q_1 + u_\mathrm{w}}{Q_1} \right)^{2\gamma/(\gamma-1)} \tag{4.20}$$

and

$$p_\mathrm{T} = p_\mathrm{T0} \left(\frac{P_2 - u_\mathrm{w}}{P_2} \right)^{2\gamma/(\gamma-1)} . \tag{4.21}$$

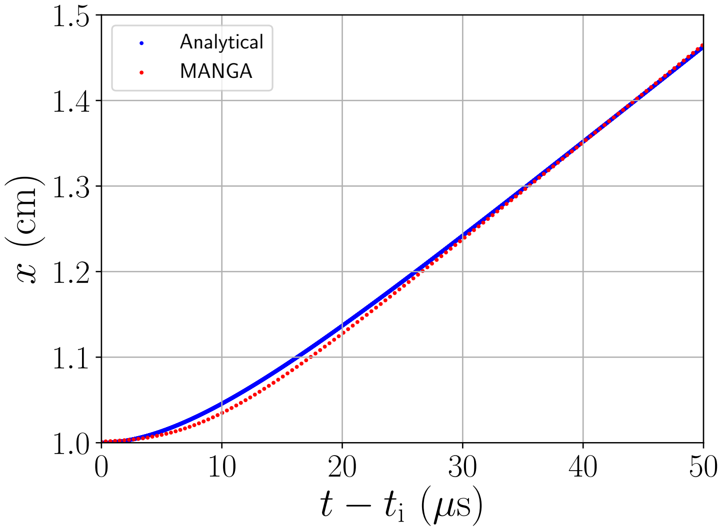

Figure 4.6: An analytical solution for the response of a movable wall to a shock wave (blue) following Meyer (1957) compared with the results from our Sod shock tube test case in MANGA (red). On the horizontal axis is the time after shock impact $t_{\rm i}$.

We can express the initial wall acceleration pressure as

$$\left(\frac{du_{\rm w}}{dt}\right)_{t=t_{\rm i}} = (p_{\rm T0} - p_1)\frac{A}{m}, \tag{4.22}$$

where A is the cross-sectional area of the wall. Putting this all into (4.18), we arrive at

$$\frac{du_{\rm w}}{dt} = \frac{A}{m}\left[p_{\rm T0}\left(\frac{P_2 - u_{\rm w}}{P_2}\right)^{2\gamma/(\gamma-1)} - p_1\left(\frac{Q_1 + u_{\rm w}}{Q_1}\right)^{2\gamma/(\gamma-1)}\right], \tag{4.23}$$

which can be numerically integrated twice with the boundary conditions $u_w = 0$ and $x = 1$ cm at $t = t_{\rm i}$ to find the path of the wall. We obtain the relevant pressures and Riemann invariants for (4.23) from our simulation output. The results are shown in Fig. 4.6 alongside those obtained in MANGA, showing that the two are consistent.

4.4.3 1-D Sedov-Taylor Blast Wave

In this test problem, we use a similar setup as in the Sod shock tube test. However, we now initialize the gas with density $\rho = 1$ g cm^{-3} and temperature $T = 1$ K except for the region $|x| < 0.1$ cm, where we set $T = 1000$ K. This results in a point explosion that is described by the Sedov-Taylor solution. It is known that the Sedov-Taylor solution is self-similar in 3-D, and we briefly show that this also holds in 1-D. Following Taylor (1950), the appropriate similarity assumptions for an expanding blast wave of constant total energy in 1-D are

$$p/p_0 = R^{-1} f_1, \quad \rho/\rho_0 = \psi, \quad \text{and} \quad u = R^{-1/2}\phi_1. \tag{4.24}$$

Here R is the radius of the blast wave, u is the fluid velocity, p_0 and ρ_0 are the ambient pressure and density and f_1, ψ, and ϕ_1 are functions only of similarity variable $\eta = x/R$. In the absence of gravity, we can now cast the Euler equations (2.12), (2.13) and (2.14) into the one-dimensional forms

$$\frac{\partial u}{\partial t} + u\frac{\partial u}{\partial x} = -\frac{p_0}{\rho}\frac{\partial (R^{-1} f_1)}{\partial x}, \tag{4.25}$$

$$\frac{\partial \rho}{\partial t} + u\frac{\partial \rho}{\partial x} + \rho\frac{\partial u}{\partial x} = 0, \tag{4.26}$$

and

$$(\frac{\partial}{\partial t} + u\frac{\partial}{\partial x})(p\rho^{-\gamma}) = 0. \tag{4.27}$$

These equations are satisfied if $\frac{dR}{dt} = AR^{-1/2}$, where A is a constant. If we additionally define $a^2 = \gamma p_0/\rho_0$, $f = f_1 a^2/A^2$ and $\phi = \phi_1/A$, then (4.25), (4.26) and (4.27) become

$$\frac{1}{2}\phi - \eta\phi' + \phi\phi' = \frac{1}{\gamma\psi}(f - f'), \tag{4.28}$$

$$-\eta\psi' + \phi\psi' + \phi'\psi = 0, \tag{4.29}$$

and

$$-\gamma\eta f\psi' + f\psi^{-\gamma} + \eta f'\psi^{-\gamma} + \gamma f\phi\psi' - f'\phi\psi^{-\gamma} = 0, \tag{4.30}$$

respectively. Here a prime denotes a derivative with respect to η. We see that (4.28), (4.29) and (4.30) are independent of R; they depend only on the similarity variable η and the gas properties p_0, ρ_0, and γ. Therefore, this is a self-similar solution. Furthermore, because (4.28), (4.29), and (4.30) are all first-order, only one boundary condition is needed for each of f, ϕ, and ψ to find a solution. These are given by the Rankine-Hugoniot shock jump conditions, which for a sufficiently strong shock take on the asymptotic forms

$$\psi = \frac{\gamma+1}{\gamma-1}, \quad f = \frac{2\gamma}{\gamma+1}, \quad \text{and} \quad \phi = \frac{2}{\gamma+1} \tag{4.31}$$

at the shock front ($\eta = 1$).

We again choose a piston as our moving boundary, extending from $x = 1$ to $x = 1.5$ cm with mass $m = 0.5$ g. We plot the density as a function of position in Fig. 4.7 at $t = 6$ μs, showing only particles with $|y| < 0.1$ and $|z| < 0.1$ cm in order to reduce the particle noise. The blast wave quickly forms and propagates outward until it impacts the piston, which is shaded in red, pushing it to the right and creating a transmitted shock. A gap is visible

Table 4.1: Piston initial position, piston mass m, number of cells resolving the blast wave N_c and momentum error ϵ_p in our Sedov-Taylor blast wave resolution test. We calculate ϵ_p when the left edge of the piston has moved from its initial position by 10%.

x Position (cm)	m (g)	N_c	ϵ_p
1 – 1.5	0.5	10	4.68×10^{-10}
2 – 3	1	20	1.27×10^{-10}
3 – 4.5	1.5	30	7.44×10^{-11}

between the left side of the piston and the mesh-generating points comprising the shock front, due to the edge cell centers maintaining their original distance from the boundary. To analyze the conservation properties of our simulation, we consider the fractional error in the conservation of momentum of the system ϵ_p, including the contributions from both the gas and the piston. Here, we find $\epsilon_p = 4.68 \times 10^{-10}$. However, we also see from the spacing of the mesh-generating points that the spatial resolution of the blast wave is poor, and thus conduct a resolution test to determine its effect on ϵ_p. Rather than changing the cell size, we exploit the self-similarity of the Sedov-Taylor solution. We perform two additional runs in which the piston is initially placed further to the right so that the number of cells N_c resolving the blast wave is greater. The mass and width of the piston are taken to be proportional to R to preserve the self-similarity of the system. Specifically, we use pistons of mass $m = 1$ and $m = 1.5$ g, extending from $x = 2$ to $x = 3$ and from $x = 3$ to $x = 4.5$ cm, respectively. These are shown in Table 4.1 along with ϵ_p, which we calculate when the left edge of the piston has moved from its initial position by 10%. We find that higher resolution improves momentum conservation as $\epsilon_p \propto N_\mathrm{c}^{-1.7}$, which is the same scaling as that for sound waves in Chang et al. (2020) and is close to the expected second-order convergence.

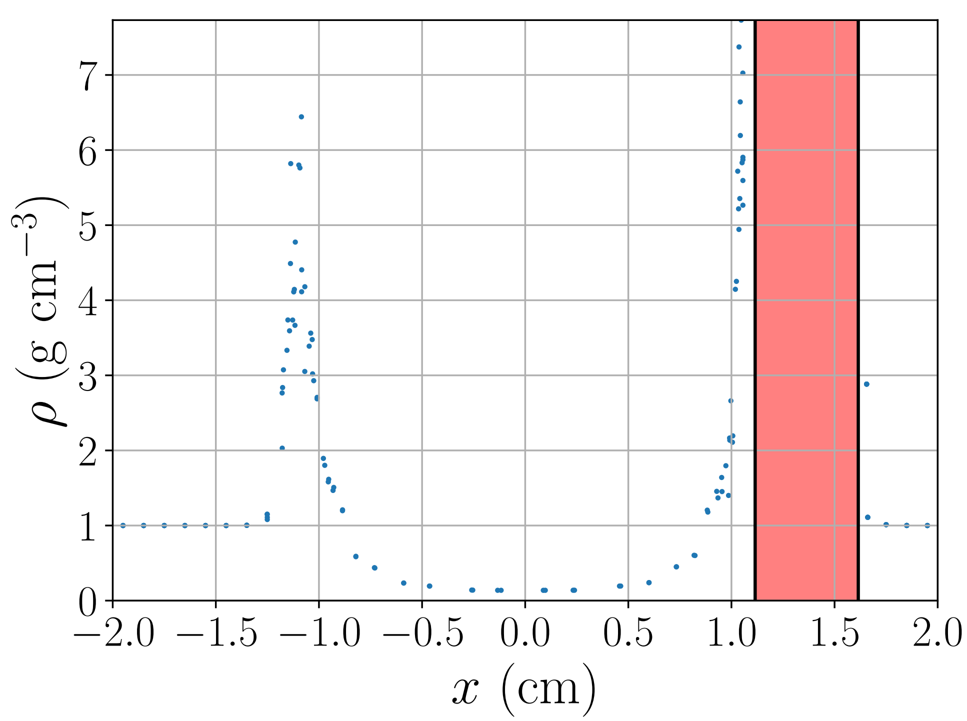

Figure 4.7: Gas density in the Sedov-Taylor blast wave test at $t = 6$ μs, restricted to particles with $|y| < 0.1$ and $|z| < 0.1$ cm to reduce the particle noise. The blast wave is colliding with a piston (shaded in red) and pushing it to the right. The gap between the left side of the piston and the mesh-generating points comprising the shock front is due to the edge cell centers maintaining their original distance from the boundary.

4.5 APPLICATION TO COMMON ENVELOPE EVOLUTION

We now discuss the development of appropriate initial conditions for CEE simulations in MANGA. Aside from the treatment of the companion, our setup is largely the same as that of Chapter 3, so we will summarize the generation of initial conditions. We first use MESA to evolve a $M = 2$ $\mathrm{M}_\odot$ star with metallicity $Z = 0.02$ from the pre-main sequence to the red giant phase, stopping when the star reaches 52 $\mathrm{R}_\odot$. This results in a helium core of mass $M_{\rm core} = 0.36$ $\mathrm{M}_\odot$, which we model as a dark matter particle. We include a hot atmosphere as in Chapter 3.

We again construct an appropriate particle mesh for the star from a pre-computed glass distribution. We assume that the particles are of equal volume and rescale them to the appropriate mass based on the computed $M(r)$ from MESA. This differs from Chapter 3, where we used equal-mass particles rescaled to the appropriate radial position to produce the same $M(r)$; a method better suited to SPH than to a moving mesh. Initially, the number of particles in the atmosphere is 9.4×10^5. The star contains 1.8×10^5 particles, yielding a total of 1.1×10^6 particles within the simulation box.

We employ an ideal gas EOS with $\gamma = 5/3$ rather than the MESA EOS. Though the MESA EOS allows us to account for recombination energy, we are concerned with the dynamics of the early inspiral. As this occurs before the ejection of the envelope, we use the computationally inexpensive ideal gas EOS.

We model the 0.99 $\mathrm{M}_\odot$ companion (half the mass of the red giant at this phase) as a spherical moving boundary. The number of particles $N_{\rm b}$ comprising the boundary is a parameter in our simulations, which we have set to $N_{\rm b} = 500$ here. This results in mesh cells with linear sizes in the range $0.2 - 0.6$ $\mathrm{R}_\odot$, depending on the radius of the boundary $R_{\rm b}$. To accurately capture the flow in the vicinity of the companion, and keeping in mind the new velocity kicks described in section 4.4.1, we refine the mesh near the initial posi-

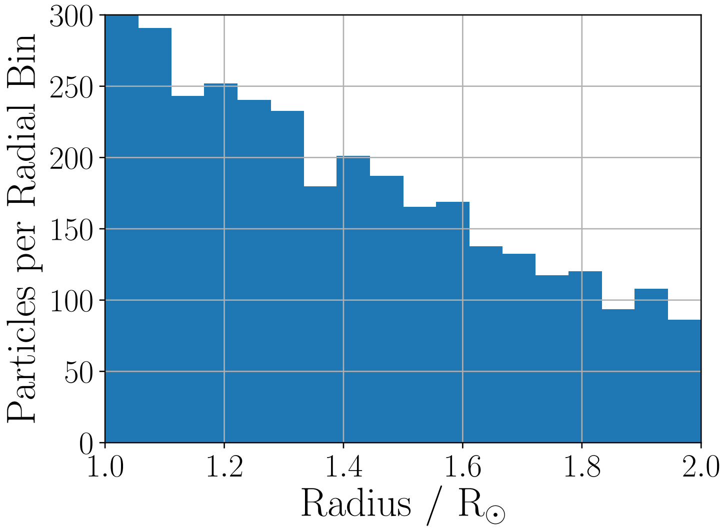

Figure 4.8: Distribution of particles near the companion in an example case with $R_\mathrm{b} = 1$ $\mathrm{R}_\odot$, normalized by $1/r^2$ to correct for the volume of each radial bin. The highest density of particles occurs next to the boundary, falling off nearly monotonically with distance.

tion of the boundary. This refinement occurs within a shell of radius $2R_\mathrm{b}$ centered on the boundary, as follows:

1. The same glass distribution of particles used for the star and atmosphere is inserted into this region.
2. The number density of mesh-generating points immediately outside of the boundary at $r = R_\mathrm{b}$ is set equal to that inside the boundary n_b.
3. At radius $r = 2R_\mathrm{b}$, the number density of particles is equal to that of the atmosphere n_atm.
4. Within the shell $R_\mathrm{b} < r < 2R_\mathrm{b}$, the number density is interpolated between n_b and n_atm, yielding $n(r)$. This is similar to the mesh refinement performed on the atmosphere, as in section 3.2, but with $k = 1$.

5. The radial positions of the mesh-generating points are rescaled to produce the computed $n(r)$.

This results in approximately 2200 particles in the vicinity of the companion. Fig. 4.8 shows an example distribution of the number of particles near the companion with $R_\mathrm{b} = 1$ R$_\odot$, sorted into radial bins. We weight each bin by $1/r^2$ to correct for the volume of each radial bin, so this histogram effectively shows the number density as a function of radius. We see that the highest number density occurs next to the boundary, and falls off almost monotonically with distance. Note that refinement need only be done during the initialization; because the boundary cells and edge cells move identically, a boundary that is highly resolved initially will remain so indefinitely. Additionally, we choose $R_\mathrm{s} = 2R_\mathrm{b}$ in (4.17) so that the volume in which the mesh refinement is performed coincides with that of the modified velocity kicks.

The companion is placed in an initially circular Keplerian orbit at a radius of 60 R$_\odot$. In Prust & Chang (2019) the companion was placed at the surface of the red giant; here it is placed farther out to facilitate the mesh refinement near the companion discussed above. Prior to the onset of CEE, tidal forces induced by the binary interaction are expected to spin up the rotation of the giant (Soker, 1996). We neglect to simulate this interaction, instead opting to initialize the rotation of the giant so that it corotates with the binary orbit following the scheme of MacLeod et al. (2018).

4.6 RESULTS

Here we perform a suite of simulations in which the size of the companion is varied across the range of 1 to 3 R$_\odot$. Specifically, we perform five simulations with $R_\mathrm{b} = 1$, 1.5, 2, 2.5 and 3 R$_\odot$ for 60 days. We show density projections in Fig. 4.9 for the case $R_\mathrm{b} = 2$ R$_\odot$, though all runs are qualitatively similar. The companion quickly plunges into the enve-

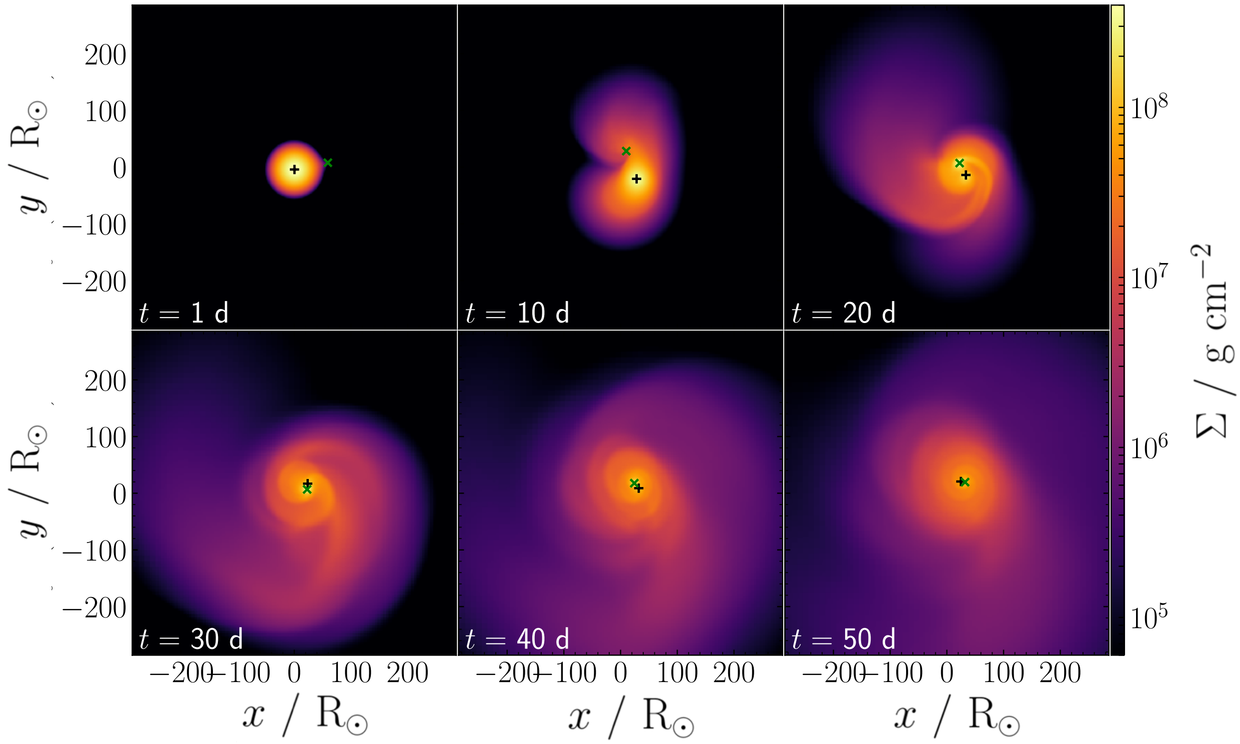

Figure 4.9: Projected density Σ along the z-axis in our simulation with $R_\mathrm{b} = 2\ \mathrm{R}_\odot$. The black + sign marks the red giant core and the green × marks the center of the companion.

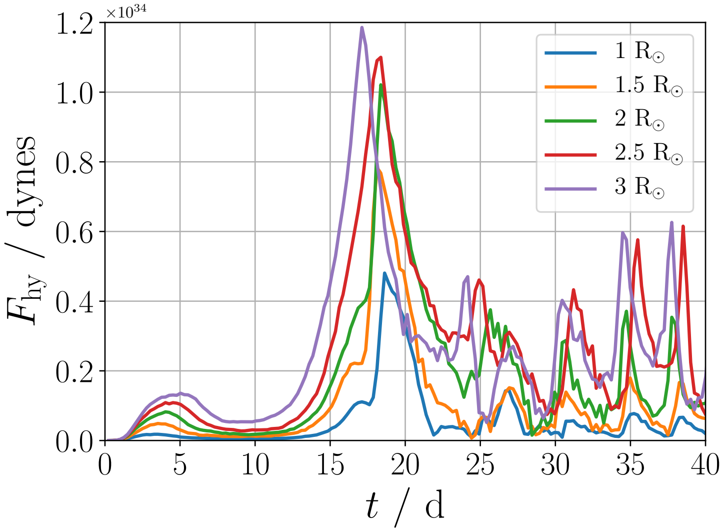

Figure 4.10: Hydrodynamic drag force versus time for all 5 runs. The peaks correspond to periastron passages. Unsurprisingly, larger boundaries experience larger hydrodynamic drag.

lope, followed by a slower inspiral. The initial tidal tail from the companion is visible, as are the spiral shocks responsible for the transfer of energy and angular momentum to the gas. After only 30 days, the orbital separation has decreased to a small fraction of its initial value.

4.6.1 Drag Force

The principal difference between simulations of CEE involving a companion of finite size and those which use a point particle companion is the presence of a hydrodynamic drag force. In Fig. 4.10, we show the hydrodynamic drag experienced by the companion as a function of time. The peaks correspond to periastron passages. Unsurprisingly, larger companions experience higher drag; the hydrodynamic drag averaged over the simulation period of 60 days for each run is shown in Fig. 4.11. Also shown is the drag as predicted using an estimate of the ram pressure on the companion, calculated as follows. As

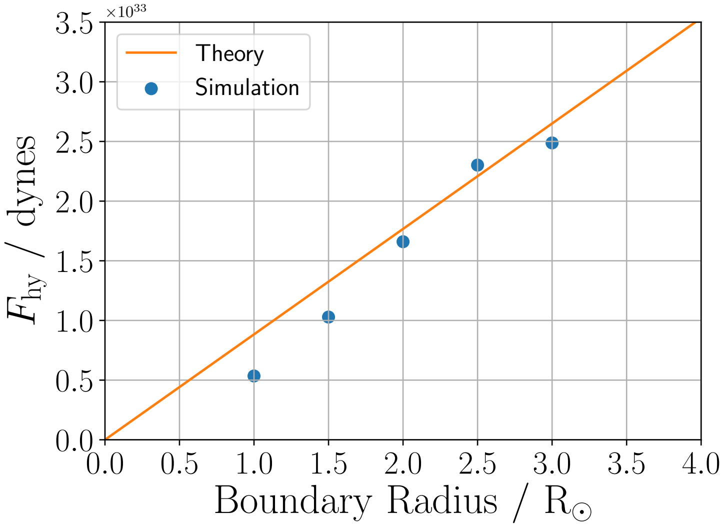

Figure 4.11: Hydrodynamic drag in each run averaged over the simulation period of 60 days, as a function of boundary radius $R_{\rm b}$. Good agreement is shown with the theoretical prediction of (4.34).

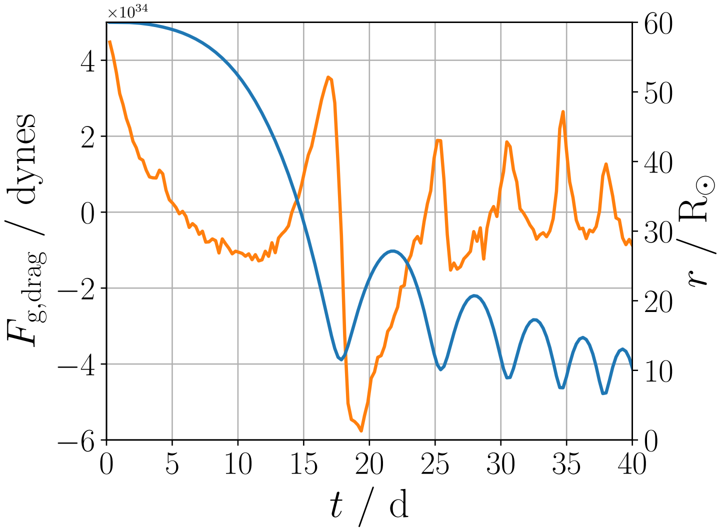

Figure 4.12: Gravitational drag (orange) and orbital separation (blue) for the case $R_{\rm b} = 2\ \rm R_\odot$, in the primed coordinate system. Periods of thrust and drag are seen to correspond to apastron and periastron, respectively.

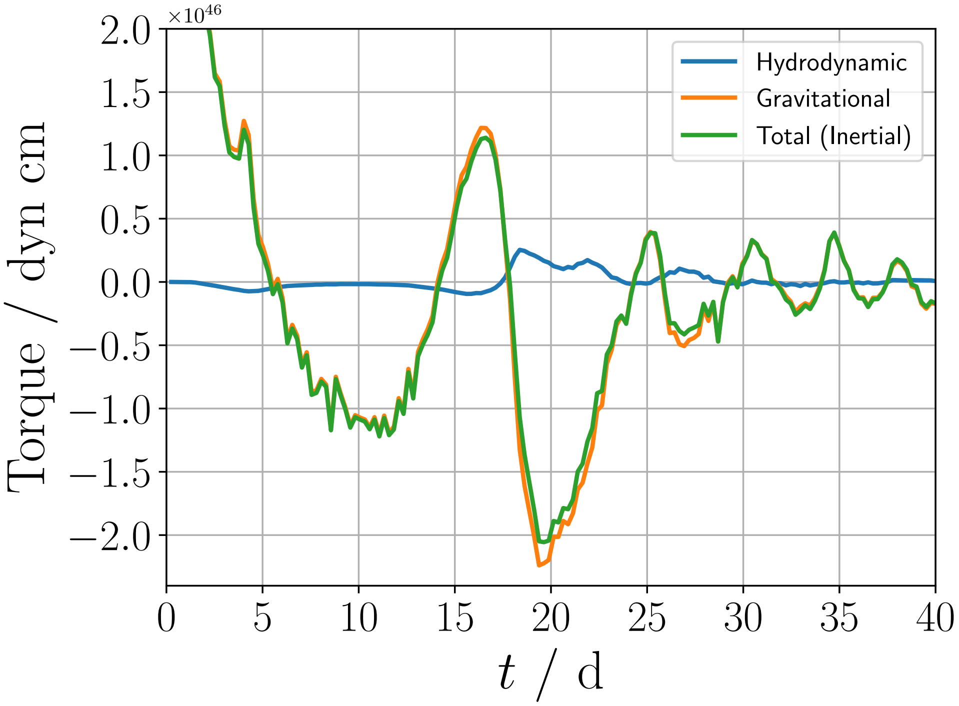

Figure 4.13: The torques exerted by hydrodynamic (blue), gravitational (orange) and total (green) forces for the case $R_{\rm b} = 2\ {\rm R}_{\odot}$. The torques are taken about the CM of the binary. We see that the gravitational torque dominates over the hydrodynamic torque, and that both can take on either positive or negative values. The negative values correspond to the injection of angular momentum into the binary, spinning it up.

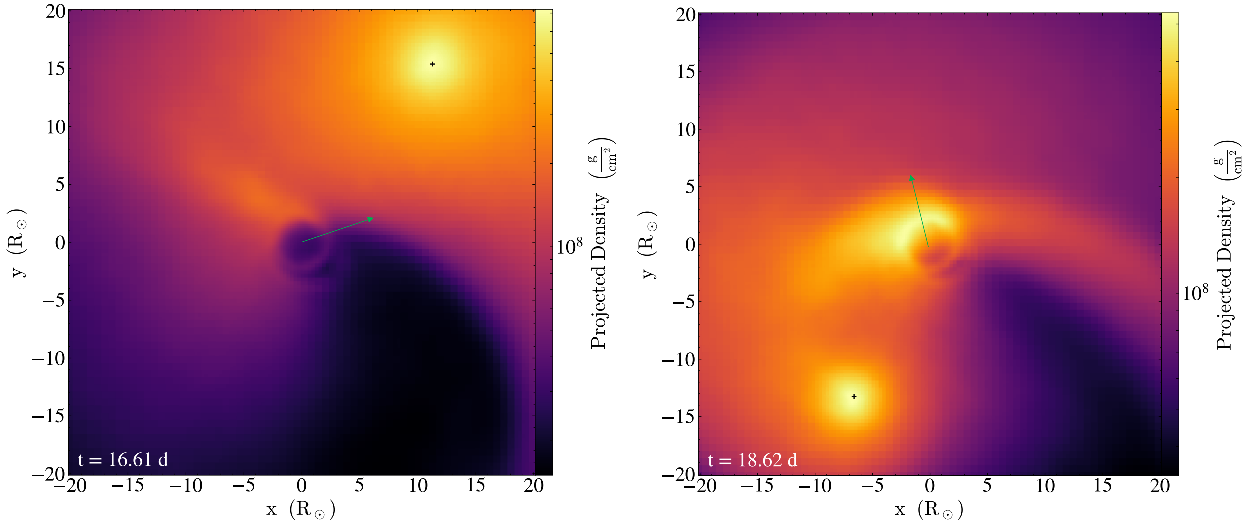

Figure 4.14: *(Left)* Density projection at $t = 16.6$ days, just before the first periastron, zoomed in and centered on the companion for $R_\mathrm{b} = 2\ \mathrm{R}_\odot$. The larger pressures on the trailing edge of the companion are evident, corresponding to the negative hydrodynamic torques seen in Fig. 4.13. The green arrow shows the direction of motion of the companion. *(Right)* The same system at $t = 18.6$ days, just after periastron. Here, we see higher pressures on the leading edge.

the companion passes through the envelope with velocity $v_{\rm c}$, it collides with gas within a cross-section with radius b. Due to the gravitational attraction of the companion, b can be much larger than $R_{\rm b}$. Thus, the accretion onto the companion can be modeled as Bondi-Hoyle-Lyttleton accretion, which was originally formulated to describe accretion onto a compact object moving through the interstellar medium (Hoyle & Lyttleton, 1939). Here the cross-section b and velocity $v_{\rm c}$ are related through the conservation of angular momentum: a particle of gas which is initially at an impact parameter b from the companion will barely reach the surface $R_{\rm b}$ moving at the escape speed $v_{\rm esc}$. Then

$$bv_{\rm c} = R_{\rm b}v_{\rm esc} = \sqrt{2GM_{\rm b}R_{\rm b}}, \tag{4.32}$$

and the accretion rate is the mass flow rate through the cross-section

$$\dot{M} = \pi b^2 \rho v_{\rm c}. \tag{4.33}$$

This leads to a hydrodynamic drag

$$F_{\rm hy} = \dot{M}v_{\rm c} \approx 2\pi G M_{\rm b} R_{\rm b} \langle\rho\rangle, \tag{4.34}$$

where $\langle\rho\rangle$ is the average density of the star. We find good agreement between this result and our simulation results, as shown in Fig. 4.11.

The other source of drag comes from gravity. The envelope exerts a gravitational force on the companion that is mostly directed inward toward the core. However, it also has an azimuthal component which can exert either a thrust or a drag on the companion. We consider a force with a negative azimuthal component to be a positive drag, and a positive azimuthal component to be a thrust (note that the direction of the orbit is counterclockwise). As do Chamandy et al. (2019), we transform to a non-inertial, non-rotating coordinate system in which the core is stationary. In this "primed" coordinate system, the position and velocity of the companion relative to the core are $\boldsymbol{r}'$ and $\boldsymbol{v}'$, respectively. Then the gravitational force on the companion transforms as

$$\boldsymbol{F}_{\mathrm{g}}' = \boldsymbol{F}_{\mathrm{g}} - \frac{M_{\mathrm{b}}}{M_{\mathrm{core}}}\boldsymbol{F}_{\mathrm{g,core}}. \tag{4.35}$$

The gravitational drag is then computed as

$$\boldsymbol{F}_{\mathrm{g,drag}} = -\hat{\boldsymbol{\phi}} \cdot \boldsymbol{F}_{\mathrm{g}}', \tag{4.36}$$

where

$$\hat{\boldsymbol{\phi}} = \hat{\boldsymbol{\phi}}' = \frac{\hat{\boldsymbol{r}}' \times \hat{\boldsymbol{v}}'}{|\hat{\boldsymbol{r}}' \times \hat{\boldsymbol{v}}'|} \times \hat{\boldsymbol{r}}' \tag{4.37}$$

is the azimuthal unit vector in the orbital plane. The gravitational drag for the case where $R_{\mathrm{b}} = 2\,\mathrm{R}_{\odot}$ is shown in Fig. 4.12 along with the orbital separation. We see that the gravitational drag changes sign in phase with the orbital period. After the ejection of large tidal tails of gas from the primary, the gas is nonaxisymmetrical. Thus, the variations in the the gravitational drag are largely due to the changing definition of $\hat{\theta}$. Chamandy et al. (2019) find that the gravitational drag is always positive in the primed coordinates, likely due to the fact that their orbits are less eccentric than ours. This is the result of differing initial conditions: to facilitate mesh refinement near the companion, we initialize the companion $\sim$8 $\mathrm{R}_{\odot}$ from the surface of the primary, while in most work it is placed in a circular orbit at the surface. We now argue that eccentric orbits can naturally result in gravitational thrust in this coordinate system. The angular momentum of the companion is $L = M_{\mathrm{b}} r^2 \dot{\phi}$, so

$$\ddot{\phi} = -2 \frac{L}{M_{\mathrm{b}}} \frac{\dot{r}}{r^3} + \frac{\dot{L}}{M_{\mathrm{b}} r^2}. \tag{4.38}$$

Then the tangential acceleration is

$$a_\phi = r\ddot{\phi} = -2 \frac{L}{M_{\mathrm{b}}} \frac{\dot{r}}{r^2} + \frac{\dot{L}}{M_{\mathrm{b}} r}. \tag{4.39}$$

A thrust corresponds to $a_\phi > 0$, and applying this condition to (4.39) yields

$$2\dot{L}/L > \dot{r}/r. \tag{4.40}$$

This can be satisfied by eccentric orbits, in which $\dot{r}$ is large and negative during the approach to periastron. This is particularly true at late times, when much of the envelope has been cleared from the orbit and $\dot{L} \approx 0$.

4.6.2 Torque

We now consider the torques exerted on the binary consisting of the core and companion by the forces discussed above. Because fictitious forces cancel out when computing torques, there is no need to boost into a non-inertial frame as in (4.35). Instead, we compute the torque about the center of mass of the binary, and take a projection normal to the orbital plane. Fig. 4.13 shows the torques for $R_{\mathrm{b}} = 2\ \mathrm{R}_\odot$. The gravitational torque is similar to the drag shown in Fig. 4.12, multiplied by the orbital separation. Here a negative torque corresponds to an addition of angular momentum to the binary, showing that gravity can indeed spin up the binary.

The hydrodynamic torque is much smaller, but makes notable contributions to the total torque during the time intervals immediately following periastron passage. Furthermore, it is negative during the initial plunge. This seemingly odd result can be explained by observing the gas in the vicinity of the companion. Fig. 4.14 shows density projections before and after the first periastron passage. At early times – before periastron – there is a tidal tail attached to the trailing edge of the companion, providing a small hydrodynamic thrust. This buildup of material behind the companion is consistent with the negative gravitational torques over much of this interval. Once periastron is reached, the companion collides with dense material surrounding the core, resulting in a large hydrodynamic drag. After the first few orbits, much of the gas has been cleared from the orbit, and the hydrodynamic torque decreases dramatically.

4.6.3 Orbital Parameters

In Fig. 4.15 we show the binary separation in all runs. We also show the separation smoothed over time, which can be taken as a proxy for the semi-major axis a. This smoothing is accomplished by taking $r_{\rm smoothed}(t)$ to be the average of all $r(t)$ within an interval of 15 days centered on t. Though Fig. 4.15 shows some differences in orbital phase, the semi-major axes are roughly uniform across the five runs. The semi-major axis is directly linked to the orbital energy through

$$\mathcal{E} = -\frac{GM_{\rm c}M_{\rm b}}{2a}, \tag{4.41}$$

which means that the presence of a moving boundary does not significantly alter the energy transfer between the binary and the gas.

However, marked differences exist between the orbital eccentricities, which are shown in Fig. 4.16. Because the potential is not Keplerian, the eccentricity cannot be directly determined from the state of the binary. Instead, the periastron and apastron distances $r_{\rm peri}$

and r_{apo} can be determined by interpolating the maxima and minima of the binary separation. The eccentricity e can then be found using only the the periastron and apastron distances,

$$e = \frac{r_{\mathrm{apo}} - r_{\mathrm{peri}}}{r_{\mathrm{apo}} + r_{\mathrm{peri}}}. \tag{4.42}$$

Though all binaries circularize their orbits over time, larger companions tend to have smaller eccentricities by almost 0.1 in some cases. This is likely due to the higher drag on these companions, which more effectively circularizes the orbits. Furthermore, the eccentricity is related to both the semi-major axis and the angular momentum through

$$L = \frac{M_{\mathrm{c}} M_{\mathrm{b}}}{\sqrt{M_{\mathrm{c}} + M_{\mathrm{b}}}} \sqrt{Ga(1 - e^2)}. \tag{4.43}$$

Therefore, differences in eccentricity indicate that the transfer of angular momentum is altered by the size of the companion. This is substantiated by the variation in hydrodynamic drag seen in section 4.6.1.

4.7 CONCLUSIONS

We find that the hydrodynamic force on the companion peaks near periastron, and that it is linear with respect to the companion radius. The hydrodynamic drag is also in agreement with theoretical estimates of the ram pressure on the companion. Our results show that the gravitational drag – or the azimuthal component of the gravitational force on the companion – can provide either a thrust or a drag, depending on the orbital phase. This result differs from that of Chamandy et al. (2019), who did not find any gravitational thrust. We attribute this discrepancy to differences in orbital eccentricity and argue that eccentric orbits necessarily lead to a thrust.

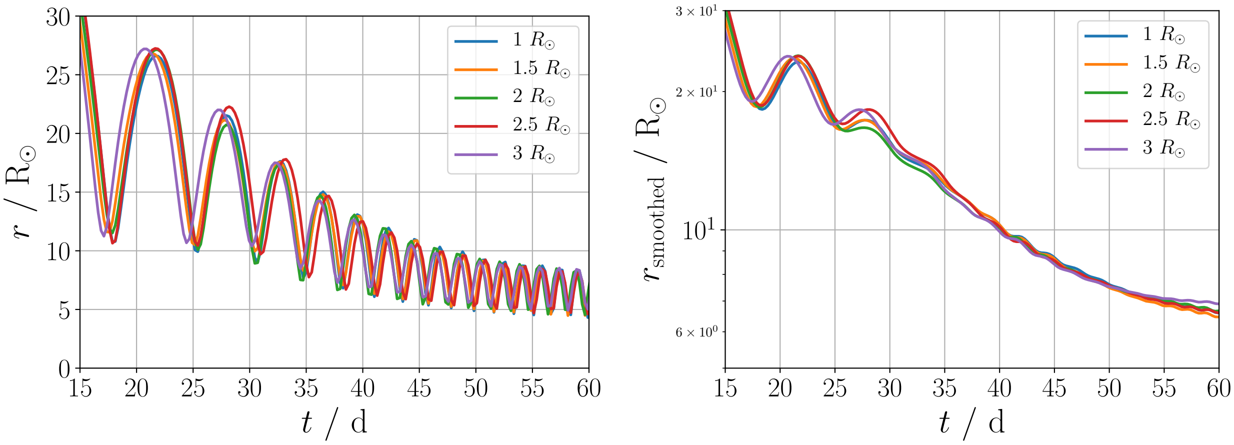

Figure 4.15: *(Left)* Separation between the stellar core and companion in each case. *(Right)* The separations smoothed over time, representing the semi-major axis. Only modest differences are seen, indicating that the semi-major axis – and thus the transfer of energy to the envelope – is independent of companion size.

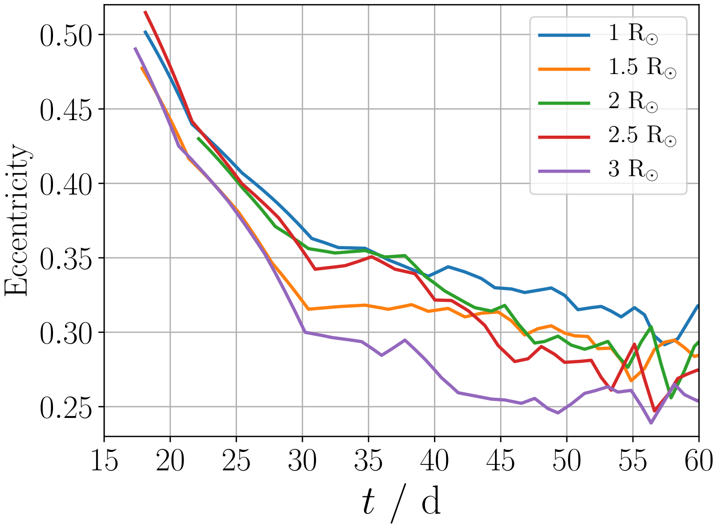

Figure 4.16: Orbital eccentricity in each case, computed using (4.42). Before $t \approx 20$ days the eccentricity cannot be calculated as the companion is still on its initial plunge. Larger companion sizes are shown to decrease the eccentricity, likely due to circularization of the orbit by larger hydrodynamic drag.

We also consider the torques exerted on the binary orbit, which are dominated by gravitational torques. However, hydrodynamic torques can make a significant contribution, particularly following periastron passage. We also find the surprising result that the hydrodynamic torques are negative prior to the first periastron passage. This result is attributed to the buildup of material on the trailing edge of the companion – which likely contributes to the negative gravitational torques observed over much of this interval.

Finally, we investigate the effects of companion size on CEE by observing the orbital parameters. It is found that the semi-major axis of the orbit is largely unaffected, while the eccentricity is lower for systems with a larger companion. The semi-major axis is directly tied to the orbital energy, while the eccentricity is dependent on both the orbital energy and angular momentum. This implies that the transfer of angular momentum is dependent on the size of the boundary, corresponding to the hydrodynamic torques. Furthermore, the differences in eccentricity indicate that the hydrodynamic forces arising from the finite size of the companion have tangible effects on the dynamics of the spiral-in phase for stellar-sized companions. We note that the eccentricity evolution in CEE depends on the stellar density profile as well as the polytropic index (Szölgyén et al., 2022).

Chamandy et al. (2019) note that an additional source of drag is needed in simulations of CEE for the results to match observations. They also find that a quasi-spherical "bulge" of gas forms around the companion of size $r_{\rm b} \approx 2.4$ R$_\odot$. This bulge experiences a ram pressure, which effectively introduces a hydrodynamic drag on the companion, and could account for this additional drag. We find hydrodynamic drag that is of the correct order of magnitude to account for this drag (10^{33} dynes), though it is unclear how the drag will evolve as the system proceeds through the self-regulating phase.

We close by stating that our methodology is suitable only for treating companions with sizes of order $\sim$0.1 $R_\odot$ or greater. Resolving a smaller companion would require a finer mesh, resulting in a range of time-scales that is larger than numerically practical. Therefore, we do not consider white dwarf or neutron star companions. We also have not accounted for stripping of the outer layers of the companion.

4.8 FUTURE DIRECTIONS: WHITE DWARF-NEUTRON STAR MERGERS

Another astrophysical problems to which moving boundaries are applicable is the merger of white dwarfs and neutron stars. Physically, white dwarf-neutron star (WDNS) mergers are qualitatively similar to CEE as the neutron star is much smaller in size than the white dwarf. However, the stellar structure and EOS are quite different than those of a red giant.

Mergers of compact binaries emit large amounts of energy in gravitational waves (GWs) which are detectable by interferometers such as LIGO (Abbott et al., 2008) and VIRGO (Acernese et al., 2006). So far, only mergers involving black holes (BH) and neutron stars (NS) have been detected (Duez, 2010; Hinder, 2010), but we also expect mergers between white dwarfs and neutron stars to occur. In fact, population synthesis studies predict that 2.2×10^6 WDNS binaries exist in our galaxy, and that the space-based Laser Interferometer Space Antenna (LISA) (Heinzel et al., 2006) will be able to detect up to 40 pre-merger binaries within a year of integration (Nelemans et al., 2001; Cooray, 2004).

A catalog of known WDNS binaries and their properties is compiled in (Paschalidis et al., 2009). Nine of the twenty binaries catalogued have a total mass greater than 1.97 $M_\odot$ which is a lower bound on the Tolman-Oppenheimer-Volkoff (TOV) limit on the maximum mass for a cold, degenerate gas (Demorest et al., 2010). Thus, the ultimate fate of a WDNS merger remnant is unclear.

Previous work (Paschalidis et al., 2009) has investigated the products of interactions in WDNS binaries in which the WD fills its Roche lobe. The results fall into one of two categories: stable mass transfer (SMT) onto the NS or unstable mass transfer (UMT) leading to tidal disruption of the WD. In the case of UMT, further interactions such as inspiral and merger occur on the dynamical timescale, unaffected by GW emission, making them a target for 3-D hydrodynamical simulations. UMT may result in the collapse of the NS to form a BH, or the WDNS may experience a merger which forms a Thorne-Zytkow-like object (TZlO) (Thorne & Zytkow, 1977) comprised of the NS at the center of the WD.

The ultimate fate of the binary cannot be determined without full GRHD simulations since in Newtonian gravity we cannot ascertain whether the neutron star will promptly collapse to a black hole, undergo a delayed collapse, or reach an equilibrium state supported against collapse by rotation and degeneracy pressure. Fully general relativistic simulations have been performed on such systems, though they are computationally prohibitive due to the range in time and length scales. For this reason, the WD has been modelled as a "pseudo-white dwarf" (pWD) which uses a six-parameter piecewise polytropic EOS which mimics realistic NS EOSs while, at the same time, scales down the size of the WD (Paschalidis et al., 2011).

An alternative approach is to model the merger using Newtonian gravity and to periodically investigate the immediate vicinity of the NS using GRHD. This allows for the use of an accurate model of the WD structure as well as the investigation of the fate of the NS. Such is the goal of this project: we plan to use 3-D hydrodynamic simulations performed in MANGA to model the global evolution of the merger. At certain time-steps, information about the immiediate vicinity of the NS from the MANGA output will be fed into the Illinois AMR GRHD code described in Etienne et al. (2009) and Etienne et al. (2010) to determine whether the NS undergoes a prompt collapse. This project also offers an opportunity to utilize the moving boundaries module, as the NS can be modeled as a moving boundary using precisely the same implementation as in our CEE simulations as described in section 4.5.

CHAPTER 5

Magnetohydrodynamics

5.1 IDEAL MHD

Magnetic fields are an important factor in many astrophysical processes. A prime example is the magnetorotational instability in accretion disks, which mediates the transport of angular momentum (Balbus & Hawley, 1998). They are also responsible for regulating star formation and launching relativistic outflows, and may have a major influence in core-collapse supernovae (Pakmor et al., 2011).

It is in principle simple to include the magnetic field in the hydrodynamic equations, as it obeys its own conservation law. However, there are several subtleties which must be addressed. Consider first the equation for the time evolution of the magnetic field

$$\frac{\partial \boldsymbol{B}}{\partial t} = \boldsymbol{\nabla} \times (\boldsymbol{v} \times \boldsymbol{B}) + \eta \boldsymbol{\nabla}^2 \boldsymbol{B}. \tag{5.1}$$

Here $\eta = (4\pi\mu\sigma)^{-1}$ is known as the magnetic diffusivity, where μ and σ are the magnetic permeability and electrical conductivity of the fluid (Cowling & Lindsay, 1957). As it stands, this cannot be written in the compact form $\frac{\partial \boldsymbol{\mathcal{U}}}{\partial t} + \boldsymbol{\nabla} \cdot \boldsymbol{\mathcal{F}} = \boldsymbol{\mathcal{S}}$ as in (2.15). However, let us expand the triple product on the right-hand side to obtain

$$\frac{\partial \boldsymbol{B}}{\partial t} = (\boldsymbol{B} \cdot \boldsymbol{\nabla})\boldsymbol{v} - (\boldsymbol{v} \cdot \boldsymbol{\nabla})\boldsymbol{B} + \boldsymbol{v}(\boldsymbol{\nabla} \cdot \boldsymbol{B}) - \boldsymbol{B}(\boldsymbol{\nabla} \cdot \boldsymbol{v}) + \boldsymbol{\nabla} \cdot (\eta \boldsymbol{\nabla} \boldsymbol{B}). \tag{5.2}$$

Recognizing that $\boldsymbol{\nabla} \cdot \boldsymbol{B} = 0$, we see that the first three terms on the right-hand side can be expressed as

$$(\boldsymbol{B} \cdot \boldsymbol{\nabla})\boldsymbol{v} - (\boldsymbol{v} \cdot \boldsymbol{\nabla})\boldsymbol{B} - \boldsymbol{B}(\boldsymbol{\nabla} \cdot \boldsymbol{v}) = \boldsymbol{\nabla} \cdot (\boldsymbol{v}\boldsymbol{B}^T - \boldsymbol{B}\boldsymbol{v}^T). \tag{5.3}$$

Finally, (5.1) can be expressed as

$$\frac{\partial \boldsymbol{B}}{\partial t} = \boldsymbol{\nabla} \cdot (\boldsymbol{v}\boldsymbol{B}^T - \boldsymbol{B}\boldsymbol{v}^T) + \boldsymbol{\nabla} \cdot (\eta \boldsymbol{\nabla} \boldsymbol{B}), \tag{5.4}$$

or

$$\frac{\partial \boldsymbol{B}}{\partial t} + \boldsymbol{\nabla} \cdot (\boldsymbol{B}\boldsymbol{v}^T - \boldsymbol{v}\boldsymbol{B}^T + \eta \boldsymbol{\nabla} \boldsymbol{B}) = 0. \tag{5.5}$$

This is now in the form of (2.15), with the caveat that there is a gradient within the flux function. Fortunately, this issue can be avoided by taking a more conceptual view of (5.1).

The two terms on the right-hand side represent two different physical processes. The first term, $\boldsymbol{\nabla} \times (\boldsymbol{v} \times \boldsymbol{B})$, represents the transport of the field along the flow. In fact, the equation $\partial \boldsymbol{\xi}/\partial t = \boldsymbol{\nabla} \times (\boldsymbol{v} \times \boldsymbol{\xi})$, which has the same form as (5.1) in the case of vanishing η, represents the transport of vorticity along the flow in inviscid fluid dynamics (Chorin & Marsden, 1993). Just as vortex lines are transported by the flow in inviscid fluids, so too are the magnetic field lines transported by the flow when magnetic diffusivity η vanishes. On the other hand, the term $\eta \boldsymbol{\nabla}^2 \boldsymbol{B}$ represents the diffusion of field lines through the fluid. Indeed, $\partial \boldsymbol{B}/\partial t = \eta \boldsymbol{\nabla}^2 \boldsymbol{B}$ has the form of a diffusion equation.

The relative strength of these two terms can be quantified by the magnetic Reynolds number. The standard Reynolds number is the ratio of the importance of inertial forces to viscous forces. Similarly, the magnetic Reynolds number is the ratio of inertial forces to diffusive ones:

$$Re_M = \frac{LV}{\eta}. \tag{5.6}$$

Here L and V are the characteristic length and velocity of the system; for the Sun, $L \approx 10^8$ cm and $V \approx 10^5$ cm/s. The diffusivity η varies from 10^2 cm^2/s in the core of the Sun to 10^8 cm^2/s in the photosphere (Cowling & Lindsay, 1957), though turbulence may raise the effective value of η in the photosphere to 10^{12} cm^2/s (Leighton, 1964). Thus, Re_M ranges from 10^1 to 10^{11}; these values are typical of astrophysical objects. Because Re_M far exceeds unity, one can safely ignore diffusion of the field and set $\eta = 0$ just as one ignores viscosity for $Re \gg 1$. This is known as the "frozen-in approximation" and forms the basis of ideal MHD. The field is said to be "frozen into" the fluid because electrical resistance is negligible, and thus any relative motion of the fluid normal to the field lines will induce a force sufficient to negate the motion.

The magnetic field can be included in the Euler equations by adding (5.5) as a fourth equation and by modifying the momentum and energy equations to account for the magnetic field:

$$\boldsymbol{\mathcal{U}} = (\rho, \rho\boldsymbol{v}, \rho e, \boldsymbol{B}), \tag{5.7}$$

$$\boldsymbol{\mathcal{F}} = (\rho\boldsymbol{v}, \rho\boldsymbol{v}\boldsymbol{v}^T + P\mathbb{I} + \boldsymbol{B}\boldsymbol{B}^T, \rho e\boldsymbol{v} + P\boldsymbol{v} - \boldsymbol{B}(\boldsymbol{v}\cdot\boldsymbol{B}), \boldsymbol{B}\boldsymbol{v}^T - \boldsymbol{v}\boldsymbol{B}^T). \tag{5.8}$$

The source term $\boldsymbol{\mathcal{S}} = (0, -\rho\boldsymbol{\nabla}\Phi, -\rho\boldsymbol{v}\cdot\boldsymbol{\nabla}\Phi, 0)$ is unmodified. As in section 2.4.5, we decompose the flux into a static term and a term due to the mesh motion. For the magnetic field evolution, this decomposition looks like

$$\boldsymbol{\mathcal{F}}_{\mathrm{m}} = (\boldsymbol{B}\boldsymbol{v}^T - \boldsymbol{v}\boldsymbol{B}^T) - \boldsymbol{B}\boldsymbol{w}^T = [\boldsymbol{B}(\boldsymbol{v}-\boldsymbol{w})^T - (\boldsymbol{v}-\boldsymbol{w})\boldsymbol{B}^T] - \boldsymbol{w}\boldsymbol{B}^T. \tag{5.9}$$

The term in brackets is the "static" term which is fed into the HLLD Riemann solver. The term on the far right $-\boldsymbol{w}\boldsymbol{B}^T$ requires some extra care. Rather than than adding it onto the face flux computed from the Riemann solver, it is instead computed via an upwind solver

$$-\boldsymbol{w}\boldsymbol{B}^T = \begin{cases} -\boldsymbol{v}_{\mathrm{face}}(\boldsymbol{B}_{\mathrm{R}} \cdot \hat{\boldsymbol{n}}) & \boldsymbol{v}_{\mathrm{face}} \cdot \hat{\boldsymbol{n}} > 0, \\ -\boldsymbol{v}_{\mathrm{face}}(\boldsymbol{B}_{\mathrm{L}} \cdot \hat{\boldsymbol{n}}) & \boldsymbol{v}_{\mathrm{face}} \cdot \hat{\boldsymbol{n}} < 0, \end{cases} \tag{5.10}$$

where $\hat{\boldsymbol{n}}$ is the outward face normal unit vector. This preserves the upwind quality of the scheme by ensuring that the face flux of the magnetic field due to the mesh motion is determined only by the upwind magnetic field. That is, the field within the cell into which the face is moving. Because of this upwind solver, the half-time-step values of the magnetic field must be computed by the use of a Riemann solver rather than predicted from the gradients. Thus, our MHD implementation is restricted to the van Leer time integration described in section 2.4.9.

Computationally, implementations of the MHD equations are plagued by a ubiquitous problem: the divergence of the magnetic field. Though the equations formally satisfy Gauss's law for magnetism $\boldsymbol{\nabla} \cdot \boldsymbol{B} = 0$, the divergence can become nonzero due to numerical errors. Once they appear, these magnetic monopoles tend to grow quickly and can become significant. There are several standard approaches to tackle this issue:

1. The issue is simply ignored. This approach is valid for only a small sub-set of idealized problems.

2. Errors in $\boldsymbol{\nabla} \cdot \boldsymbol{B}$ are advected at the fastest possible speed to the domain boundaries. This is the approach taken by the Dedner divergence cleaning and Powell eight-wave methods, both of which are discussed below.

3. A damping source term is introduced to exponentially damp magnetic monopoles.

This is also used by the Dedner scheme.

4. The magnetic field is determined from the electric field $\boldsymbol{E}$ using Faraday's induction equation

$$\partial \boldsymbol{B}/\partial t = -\boldsymbol{\nabla} \times \boldsymbol{E} = \boldsymbol{\nabla} \times (\boldsymbol{v} \times \boldsymbol{B}). \tag{5.11}$$

   Here $\boldsymbol{E}$ is determined at the corners of cells, and its circulation is computed about a cell interface to compute the magnetic flux through the face (Mocz et al., 2014). Known as the constrained transport (CT) method, this guarantees $\boldsymbol{\nabla} \cdot \boldsymbol{B} = 0$ to within machine precision and is commonly used in Eulerian grid codes (Evans & Hawley, 1988). However, CT is notoriously difficult to implement on unstructured, moving grids due to the challenges associated with performing an accurate mapping from $\boldsymbol{E}$ to $\boldsymbol{B}$. Mocz et al. (2016) achieved this via a clever exploitation of the Delaunay triangulation, which in AREPO is computed prior to the generation of the Voronoi mesh. However, at the time of writing the method is not compatible with individual time-stepping.

5.2 DIVERGENCE CLEANING

We implement the generalized Lagrange multiplier (GLM) method proposed by Dedner et al. (2002) to ensure that $\boldsymbol{\nabla} \cdot B \approx 0$, in which a variable Ψ related to the divergence of the magnetic field is introduced. The cleaning is then accomplished via a 2-pronged approach: we include a source term in (2.15) to damp this variable exponentially, and add a diffusion term for Ψ to the flux function (5.8), further preventing a non-zero divergence from accumulating in any one location.

Both prongs depend on the physical constant c_h, which was introduced by Dedner et al. (2002) and acts as the advection speed of magnetic divergence. There are no physical constraints on the value chosen for c_h, but it must be chosen globally and must be large enough to prevent an unphysical build-up of divergence. These requirements can be broadly satisfied by choosing c_h to be the largest signal speed present within the simulation at a given time (Pakmor et al., 2011). With the inclusion of MHD, the signal speed is defined as $v_{\text{sig}} = c_s + v_A - \boldsymbol{dv} \cdot \boldsymbol{dR}/dR$, where $\boldsymbol{dv}$ and $\boldsymbol{dR}$ are the differences in fluid velocity and position of two neighboring cells. At each time-step in our simulations, we determine the maximum signal speed among all cells and assign this to $c_h = \max(v_{\text{sig},i})$. Because c_h is an advection speed, its introduction necessitates an additional constraint on Δt. Similar to the Courant time-step, we require that the time-step of cell i satisfy $\Delta t_i < \eta_{\text{CFL}} r_{\text{eff}}/c_h$ where $r_{\text{eff}} = (\frac{3}{4\pi}V)^{1/3}$ is the cell effective radius. This results in a MHD algorithm which is stable but somewhat slow, as a single cell with high signal speed limits the time-step for all cells. Effectively, this means that our multistepping scheme (see section 2.4.8) is partially disabled.

5.2.1 Damping Term

To damp out nonzero values of Ψ, we include a source term which depends on both Ψ and its derivative:

$$\Delta\Psi^{n+1} = -(1 - \exp f)(\Psi^{n+1/2} + \frac{1}{2}\Delta\Psi^{n+1/2}), \tag{5.12}$$

where $n + 1/2$ denotes values at the half-timestep. Here f is defined as

$$f = -\Delta t \sigma c_h / r_{\text{eff}}, \tag{5.13}$$

as in Tricco & Price (2012), where $\sigma = 0.1$ is the damping parameter. We find that this choice of prefactor allows for stable integrations. This differs from Dedner et al. (2002) who used a prefactor proportional to $\Delta t c_h^2/c_p^2$ where a typical choice for c_p is $\sqrt{0.18 c_h}$.

5.2.2 Diffusion Term

At each cell interface, we define

$$\begin{aligned} c_{h,\mathrm{face}} &= \frac{1}{2}(c_{h,\mathrm{L}} + c_{h,\mathrm{R}}), && (5.14)\\ B_\perp^* &= \frac{1}{2}(B_{\perp,\mathrm{R}} + B_{\perp,\mathrm{L}}) - \frac{1}{2c_{h,\mathrm{face}}}(\Psi_\mathrm{R} - \Psi_\mathrm{L}), && (5.15)\\ \Psi^* &= \frac{1}{2}(\Psi_\mathrm{R} + \Psi_\mathrm{L}) - \frac{1}{2}c_{h,\mathrm{face}}(B_{\perp,\mathrm{R}} + B_{\perp,\mathrm{L}}). && (5.16) \end{aligned}$$

Here $B_\perp$ is the component of the field normal to the face. We use the HLLD Riemann solver implemented in Athena. However, for the $B_\perp$ and Ψ fluxes we instead use

$$\begin{aligned} \hat{\boldsymbol{F}}(B_\perp) &= \Psi^*, && (5.17)\\ \hat{\boldsymbol{F}}(\Psi) &= B_\perp^* c_{h,\mathrm{face}}^2. && (5.18) \end{aligned}$$

5.3 POWELL EIGHT-WAVE SCHEME

We have also implemented a Powell eight-wave scheme based on Powell et al. (1999) and adapted for a moving mesh in Pakmor & Springel (2013). This scheme differs from divergence cleaning in that only a diffusion term is used. This diffusion is implemented

Table 5.1: Error in each of our Alfvén wave simulations, computed by taking the L1 norm of the differences between our results and the analytical solution. The solutions converge as a power law with exponent k. The error increases with the grid noise, though $k \approx 1$ in every case.

N_x	$\epsilon_{\rm low}$ $(\times 10^{10})$	$\epsilon_{\rm med}$ $(\times 10^{10})$	$\epsilon_{\rm high}$ $(\times 10^{10})$
8	6.88	7.32	7.84
16	3.44	3.74	4.29
22	2.73	2.96	3.46
32	1.58	1.82	2.15
80	0.603	0.712	0.898
160	0.333	0.366	0.450
k	1.03	1.01	0.965

by including source terms in (2.15) proportional to the divergence of the field:

$$\boldsymbol{\mathcal{S}}_{\rm P} = -(\boldsymbol{\nabla} \cdot \boldsymbol{B}) \begin{pmatrix} 0 \\ \boldsymbol{B} \\ (\boldsymbol{v} \cdot \boldsymbol{B}) \\ \boldsymbol{v} \end{pmatrix} . \tag{5.19}$$

Though this scheme is simpler and less accurate, it offers a substantial increase in performance. This is due to the fact that the Powell eight-wave scheme has no need for the maximum signal speed c_h and does not limit the time-step globally. Rather, though the time-step is still limited by the Alfvén speed, it is determined locally.

5.4 TEST CASES

5.4.1 Circularly-Polarized Alfvén Wave

The MHD equations admit several types of waves: longitudinal sound waves which travel parallel to the field lines, longitudinal magnetosonic waves which travel normal

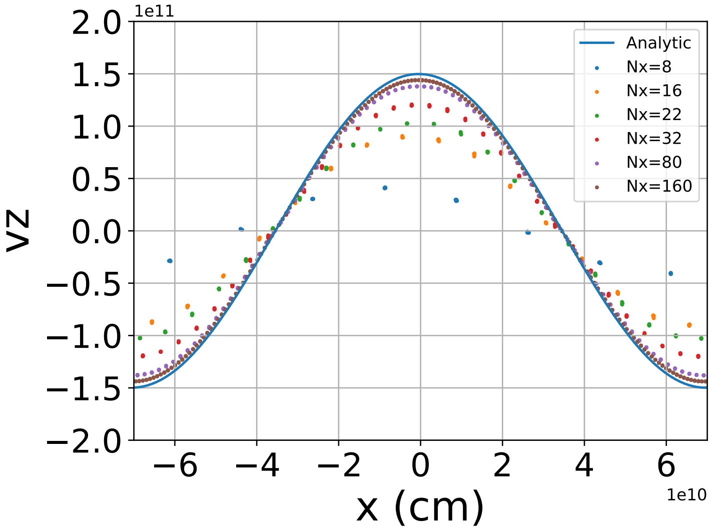

Figure 5.1: The transverse velocity v_z in the Alfvén wave test with grid noise $f = f_{\rm med}$ after one Alfvén crossing time. The global magnetic field and direction of propagation point to the right. The wave is damped proportional to the resolution N_x as a result of the divergence cleaning scheme.

to the field lines, and transverse Alfvén waves which travel parallel to the field lines. The Alfvén wave is an essential test for the interaction between magnetic fields and matter in MHD codes. These waves can be understood by examining the evolution equation (5.1) with vanishing η:

$$\frac{\partial \boldsymbol{B}}{\partial t} = \boldsymbol{\nabla} \times (\boldsymbol{v} \times \boldsymbol{B}). \tag{5.20}$$

We begin with a fluid at rest in a uniform field $\boldsymbol{B}_0$ perturbed by an Alfvén wave with velocity $\boldsymbol{v}_1$ and field $\boldsymbol{B}_1$. Then we can expand the above equation in small quantities:

$$\frac{\partial \boldsymbol{B}_0}{\partial t} + \frac{\partial \boldsymbol{B}_1}{\partial t} = \boldsymbol{\nabla} \times (\boldsymbol{v}_1 \times \boldsymbol{B}_0) + \boldsymbol{\nabla} \times (\boldsymbol{v}_1 \times \boldsymbol{B}_1). \tag{5.21}$$

Because the global field is constant, $\partial \boldsymbol{B}_0/\partial t = 0$. We can also set $\boldsymbol{v}_1 \times \boldsymbol{B}_1 = 0$ since both are small, leaving us with

$$\frac{\partial \boldsymbol{B}_1}{\partial t} = \boldsymbol{\nabla} \times (\boldsymbol{v}_1 \times \boldsymbol{B}_0). \tag{5.22}$$

For Alfvén waves, the wave vector $\boldsymbol{k}$ is parallel to $\boldsymbol{B}_0$ and normal to $\boldsymbol{v}_1$. For a transverse plane wave $\boldsymbol{v}_1(\boldsymbol{r}, t) \propto \exp(i\boldsymbol{k}\cdot\boldsymbol{r} - i\omega t)$ we can simplify the triple product on the right-hand side to $(\boldsymbol{B}_0 \cdot \boldsymbol{\nabla})\boldsymbol{v}_1$. Then

$$\boldsymbol{B}_1 = \int (\boldsymbol{B}_0 \cdot \boldsymbol{\nabla})\boldsymbol{v}_1 dt, \tag{5.23}$$

and we carry out the integration to yield

$$\boldsymbol{B}_1 = -\frac{1}{\omega}(\boldsymbol{B}_0 \cdot \boldsymbol{k})\boldsymbol{v}_1(\boldsymbol{r}, t) = -\frac{k}{\omega} B_0 \boldsymbol{v}_1(\boldsymbol{r}, t). \tag{5.24}$$

Furthermore, just as sound waves travel at speed $c_s = \sqrt{P/\rho}$, we expect MHD waves to travel at a characteristic speed determined by the magnetic pressure $P_{\text{mag}} = B_0^2/4\pi$. This is known as the Alfvén speed

$$v_{\text{A}} = \frac{B_0}{\sqrt{4\pi\rho}}. \tag{5.25}$$

Then $\omega/k = v_{\text{A}}$ and

$$\boldsymbol{B}_1 = -\frac{B_0}{v_{\text{A}}} \boldsymbol{v}_1(\boldsymbol{r}, t) \tag{5.26}$$

is the magnetic field of an Alfvén wave for a given velocity perturbation $\boldsymbol{v}_1(\boldsymbol{r}, t)$.

To simulate an Alfvén wave in MANGA we initialize a tube of gas with length $L_x =$

$2\mathrm{R}_\odot$, density $\rho = 10^{-7}$ g/cm^3, sound speed $c_s = 3.87 \times 10^9$ cm/s, and global magnetic field of strength $B_0 = \sqrt{4\pi} \times 10^5$ G in the x-direction. Perpendicular to this, we also set up transverse velocities and their corresponding magnetic fields according to (5.26)

$$\begin{aligned} \boldsymbol{v}_1 &= (0, ac_s \sin[k_x x], ac_s \cos[k_x x]), & (5.27) \\ \boldsymbol{B} = \boldsymbol{B}_0 - \frac{B_0}{v_\mathrm{A}}\boldsymbol{v}_1 &= (B_0, -B_0 v_{1,y}/v_A, -B_0 v_{1,z}/v_A), & (5.28) \end{aligned}$$

where $a = 0.01$ is an amplitude typically chosen to be much smaller than unity. This wave is circularly polarized, as the transverse components are out of phase. We use an ideal gas equation of state, though the density is uniform.

We use a pseudo-Cartesian mesh, but include some noise in the initial particle positions so that the cells are not exactly cubical. A cubical mesh is undesirable when using a Voronoi tessellation because it leads to degenerate faces and edges. Along the transverse directions we use $N_y = N_z = 8$ cells, while the number of cells along the direction of propagation N_x is an adjustable parameter. The transverse dimensions of the tube are set such that the cells have the same shape regardless of the value of N_x. That is, the condition $L_x/N_x = L_y/N_y = L_z/N_z$ is preserved. We also vary the noise used in our initial conditions. When computing the initial positions of the mesh-generating points, we include a factor proportional to $f(\vec{r}_\mathrm{rand} - 0.5)$ where $\vec{r}_\mathrm{rand}$ is a random vector of real values between 0 and 1. For the factor f we have chosen three values to compare:

$$f_\mathrm{low} = 0.001, \quad f_\mathrm{med} = 0.025, \quad f_\mathrm{high} = 0.1. \tag{5.29}$$

The transverse fluid velocities after one Alfvén crossing time are shown in Fig. 5.1. We find that the divergence cleaning scheme leads to damping in the Alfvén wave, as in Mocz et al. (2016). However, it is clear from Fig. 5.1 that this damping is resolution-dependent. The velocity field of an Alfvén wave has a simple analytical solution obtained by propagating our initial field along $\boldsymbol{B}_0$ at speed v_{A}. For v_z the solution is

$$v_{z,\mathrm{an}} = a c_s \cos[k_x(x - v_A t)]. \tag{5.30}$$

We compute the numerical error using the L1 norm of the deviation of the fluid velocity in our simulation output from the analytical solution:

$$\epsilon = \frac{1}{N}\sum_{i=1}^{N}(v_{z,i} - v_{z,\mathrm{an}}). \tag{5.31}$$

The errors are shown in Table 5.1, in which we see that the data converges to the analytical solution and that the error increases with the grid noise. We also fit the error to a power law of the form $\epsilon \propto N_x^k$ and find that $k \approx 1$ regardless of noise.

5.4.2 Sedov-Taylor Blast Wave

In contrast to the relatively well-behaved Alfvén wave, which deals only with small perturbations, it is important to use test cases involving shocks and strong gradients. These are present in many astrophysical systems, including the common envelope phase we investigate in section 5.5. To this end, we now simulate a Sedov-Taylor blast wave, which is one of the cases used to initially validate MANGA in Chang et al. (2017).

We start with a uniform medium at rest with $\rho = 8 \times 10^{-5}$ g/cm^3 and $c_{s,\mathrm{low}} = 10^6$ cm/s and initialize a small central region with $c_{s,\mathrm{high}} = 10^5 c_{s,\mathrm{low}}$ within radius $R_{\mathrm{c}} = 9 \times 10^{10}$ cm. We also set up a global magnetic field with strength 4.64×10^5 G along the y-z direction. Then the magnetic pressure exceeds the gas pressure by a factor $P_{\mathrm{mag}}/P_{\mathrm{gas}} = 10$. The simulation box is cubic with side length $L = 2 \times 10^{12}$ cm. Unlike the Alfvén wave, we use a pre-computed glass distribution for the initial positions of the $N = 2.6 \times 10^5$ mesh-

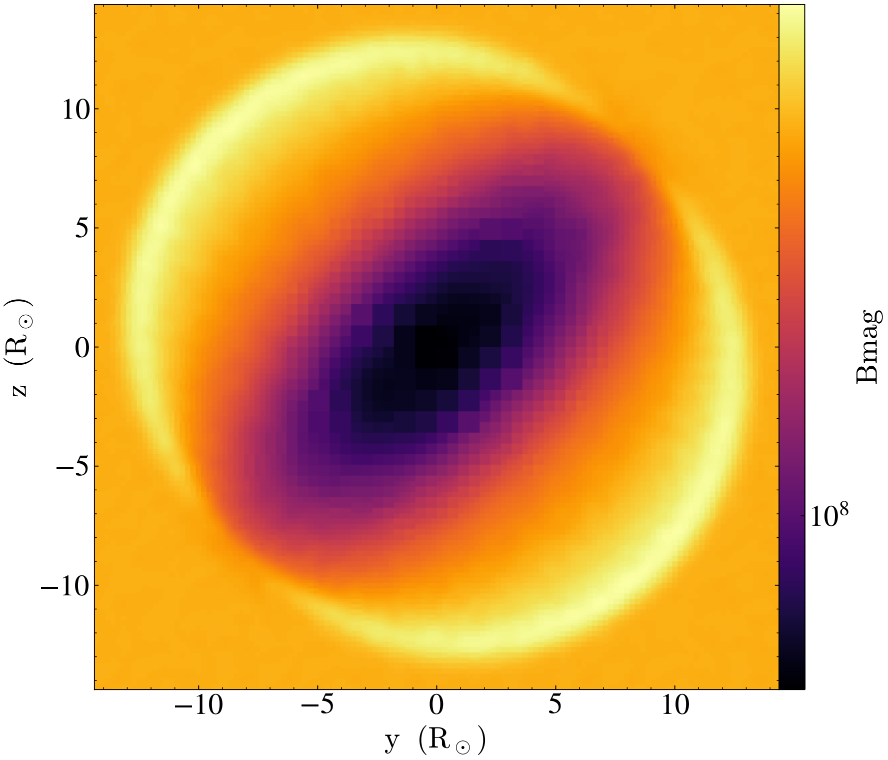

Figure 5.2: The magnetic field strength in a slice through the $x = 0$ plane at $t = 5.38$ hr in the Sedov-Taylor blast wave test. The global field is diagonal along the y-z direction with magnitude 4.64×10^5 G. We see that the blast wave is elongated along the plane normal to the global field as a result of the increase in magnetic pressure.

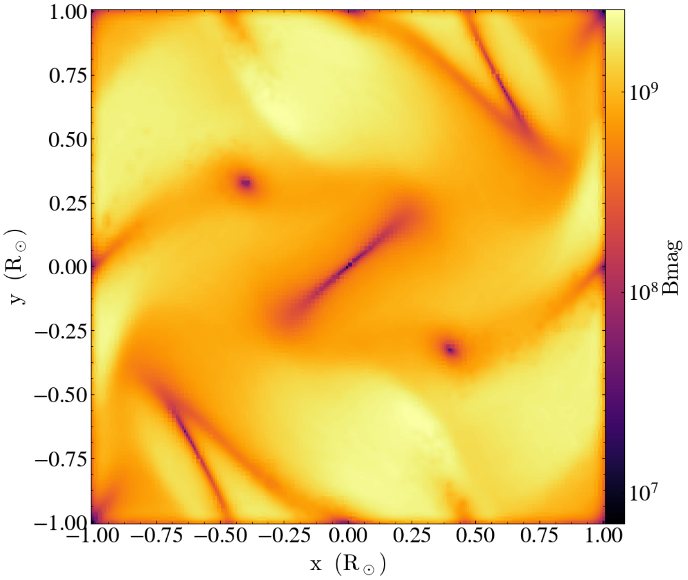

Figure 5.3: A snapshot of the magnetic field magnitude in the Orszag-Tang vortex test. The pattern of interacting shocks shows broad agreement with similar tests performed in AREPO.

generating points.

Fig. 5.2 shows the magnetic field strength on the $x = 0$ plane at $t = 5.38$ hr. We see an asymmetry in the shock: the expansion is markedly larger along the plane perpendicular to the global magnetic field. This expansion is driven by the large magnetic pressure within the bulge. These results show that our module is able to handle strong gradients, and agrees with similar tests performed in several previous studies (for example, Stone et al., 2008; Pakmor et al., 2011).

5.4.3 Orszag-Tang Vortex

As with the Alfvén wave, the Orszag-Tang vortex (Orszag & Tang, 1979) is an important test for the interaction between the magnetic field and matter as it initiates supersonic turbulence which decays over time. It is also an excellent stability test due to the shock interactions as well as the strong gradients present. We initialize $\boldsymbol{B}$ and $\boldsymbol{v}$ as

$$\begin{aligned} \boldsymbol{B} &= (-B_0 \sin[k_x y], B_0 \sin[k_x x], 0), \quad (5.32) \\ \boldsymbol{v} &= (-c_s \sin[k_x y], c_s \sin[k_x x], 0), \quad (5.33) \end{aligned}$$

with uniform density $\rho = 10^{-7}$ g/cm^3 and $c_s = 3.87 \times 10^9$ cm/s. We use $B_0 = \sqrt{\rho c_s^2}$ as a characteristic magnetic field for the problem. Because this is an inherently 2-D problem, we use a thin simulation box of dimensions $(2, 2, 0.02)$ R$_\odot$, with all fluid properties uniform along the z-direction. We use the same glass distribution as for the blast wave with $N = 74000$ particles. The results are shown in Fig. 5.3 and demonstrate agreement with similar results from AREPO (for example, Pakmor et al., 2011; Mocz et al., 2016).

5.5 APPLICATION TO COMMON ENVELOPE EVOLUTION

5.5.1 Simulation Setup

We generate the initial conditions in the same manner as in section 4.5, with several notable exceptions. The star contains 2.7×10^5 particles, while the atmosphere contains 1.5×10^6. Though this simulation does not use a moving boundary, we use the same refinement algorithm as in section 4.5 with $R_\mathrm{b} = 2$ R$_\odot$, as the immediate vicinity of the companion is thought to be important for the generation of magnetic fields. We set the number of particles within a distance of 2 R$_\odot$ of the companion to be 5×10^3, resulting in 2.2×10^4 particles within 2 – 4 R$_\odot$ of the companion.

We also place the companion at the surface of the red giant, meaning that the refinement involves cells which contain stellar material as well as those which only contain vacuum. After the refinement, the new cells are filled with stellar material appropriately by interpolating the stellar profile (after core excision, as described in section 3.1).

We initialize the magnetic field within the giant using the field proposed by Lyutikov (2010), excluding their equatorial toroidal field. This is similar to a dipole field but avoids the problematic large (or infinite) fields at the center of the star. Outside of the star, the field is equivalent to a dipole field, but inside it is given by

$$\boldsymbol{B} = \frac{B_0}{2R_*^2}[3\varpi z \hat{e}_\varpi + (5R_*^2 - 6\varpi^2 - 3z^2)\hat{e}_z]. \tag{5.34}$$

Note this ensures that at the stellar surface $r = R_*$ the field is both continuous and divergence-free. Here B_0 is the field strength at the stellar surface and ϖ is the cylindrical radius. We use $B_0 = \sqrt{4\pi} \times 10^{-6}$ G, which is similar to the field strength in two of the runs performed by Ohlmann et al. (2016b).

We also alter the mesh motion in the vicinity of the companion similar to the alterations near a moving boundary described in section 4.4.1. The mesh-generating points near the companion move with a velocity that grows from the companion velocity $\boldsymbol{v}_{\rm comp}$ for cells near the companion to the fluid velocity $\boldsymbol{v}_i$ for cells far away. This ensures that the immediate vicinity of the companion is fairly well-resolved. Within a spherical shell with radius $R_{\rm sh}$, this takes the form

$$\boldsymbol{v}(\boldsymbol{r}) = \frac{|\boldsymbol{r} - \boldsymbol{r}_{\rm comp}|}{R_{\rm sh}}\boldsymbol{v}_i + \frac{R_{\rm sh} - |\boldsymbol{r} - \boldsymbol{r}_{\rm comp}|}{R_{\rm sh}}\boldsymbol{v}_{\rm comp}. \tag{5.35}$$

Note that this satisfies $\boldsymbol{v}(\boldsymbol{r}_{\rm comp}) = \boldsymbol{v}_{\rm comp}$. For $|\boldsymbol{r} - \boldsymbol{r}_{\rm comp}| > R_{\rm s}$, the velocity is determined as usual by the fluid velocity as well as the corrections described in Chang et al. (2017).

5.5.2 Static Star Relaxation

We first relax a single red giant star without the presence of a companion. We perform this relaxation for both the Lyutikov field described above and a dipole field for the pur-

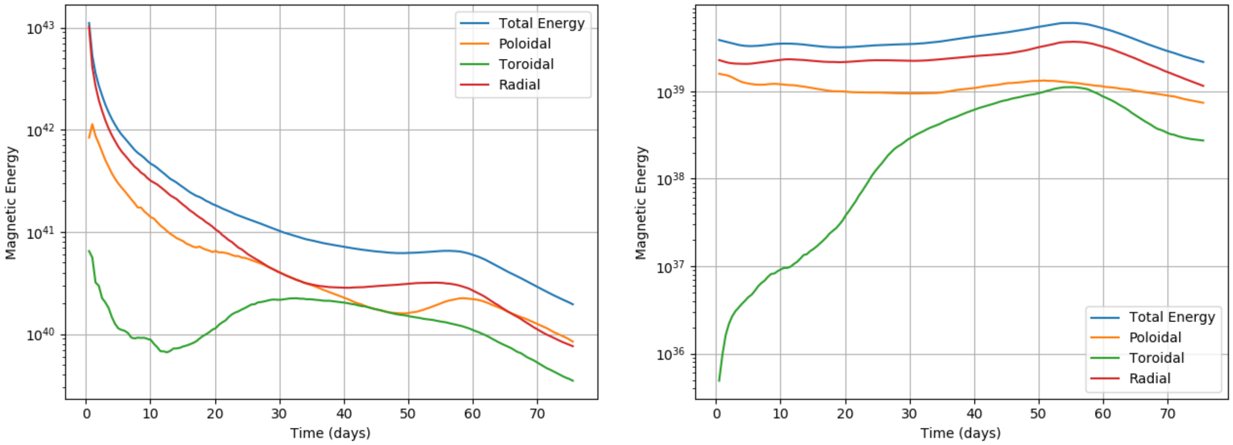

Figure 5.4: Energy in the total magnetic field and in each of its components in a static red giant relaxation using divergence cleaning. The initial field configurations are a dipole field *(left)* and the field proposed by Lyutikov (2010) *(right)*. For the dipole field, a rapid and immediate decrease is seen in the energy due to the divergent field at the stellar center. For the Lyutikov field, the energy shows only small variations with the exception of the toroidal component.

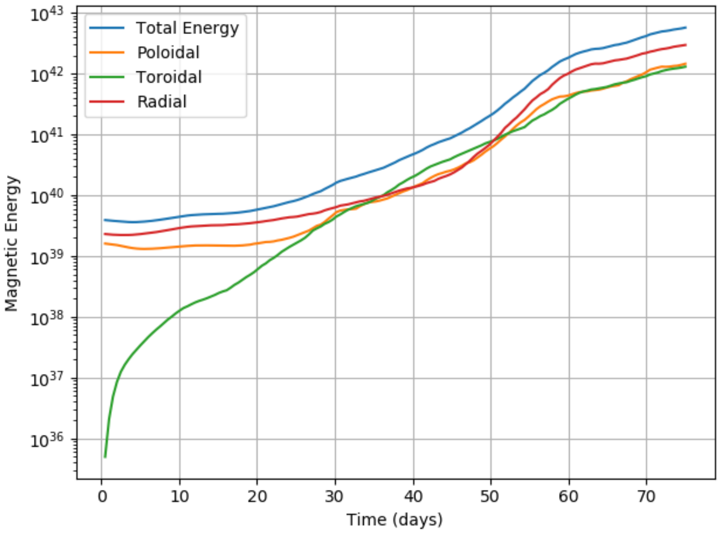

Figure 5.5: Energy in the total magnetic field and in each of its components in a static red giant relaxation using the Powell eight-wave scheme. The initial field configuration is that proposed by Lyutikov (2010). We see a gradual yet concerning rise in the field energy over time.

pose of comparison. For both fields, we set $B_0 = \sqrt{4\pi} \times 10^{-6}$ G. Both stars experience oscillations due to the spurious velocities introduced as a result of discretization errors in the mapping from a 1-D stellar evolution model to a 3-D hydrodynamics simulation. We showed in Chapter 3 that after these oscillations are damped out, the relaxed density profile closely matches the original MESA profile.

We also look at the energy stored in the magnetic field in both cases in Fig. 5.4. For the dipole field, the energy suffers an immediate and dramatic drop as the large field at the stellar center disperses. When the Lyutikov field is used, the magnetic energy stays relatively constant, with variations that can be explained by the stellar oscillations. Significant changes are seen only in the toroidal component of the field, though it remains the weakest component. We show the same relaxation using the Powell eight-wave scheme in Fig. 5.5 for the Lyutikov field. Here we see a consistent rise in the field energy over time, demonstrating that the divergence cleaning produces more accurate results in this case.

5.5.3 Results

We simulate the binary for 33 days and show several density projections in Fig. 5.6 at $t = 1$, 10, 20, 30, 40 and 50 days. As in previous chapters, we see a radial plunge into the envelope, with gas ejected via tidal tails and spiral shocks as orbital energy is transferred to the envelope.

We show the magnetic field energy in the early stages of our simulation in Fig. 5.7. The field is constant for the first two days before a rapid amplification by a factor of $\sim 10^{18}$ over a period of less than two days. Afterward, the field energy gradually increases but stays fairly constant. This amplification closely resembles that found by Ohlmann et al. (2016b). We also show the energy in each component of $\boldsymbol{B}$, revealing that the amplifica-

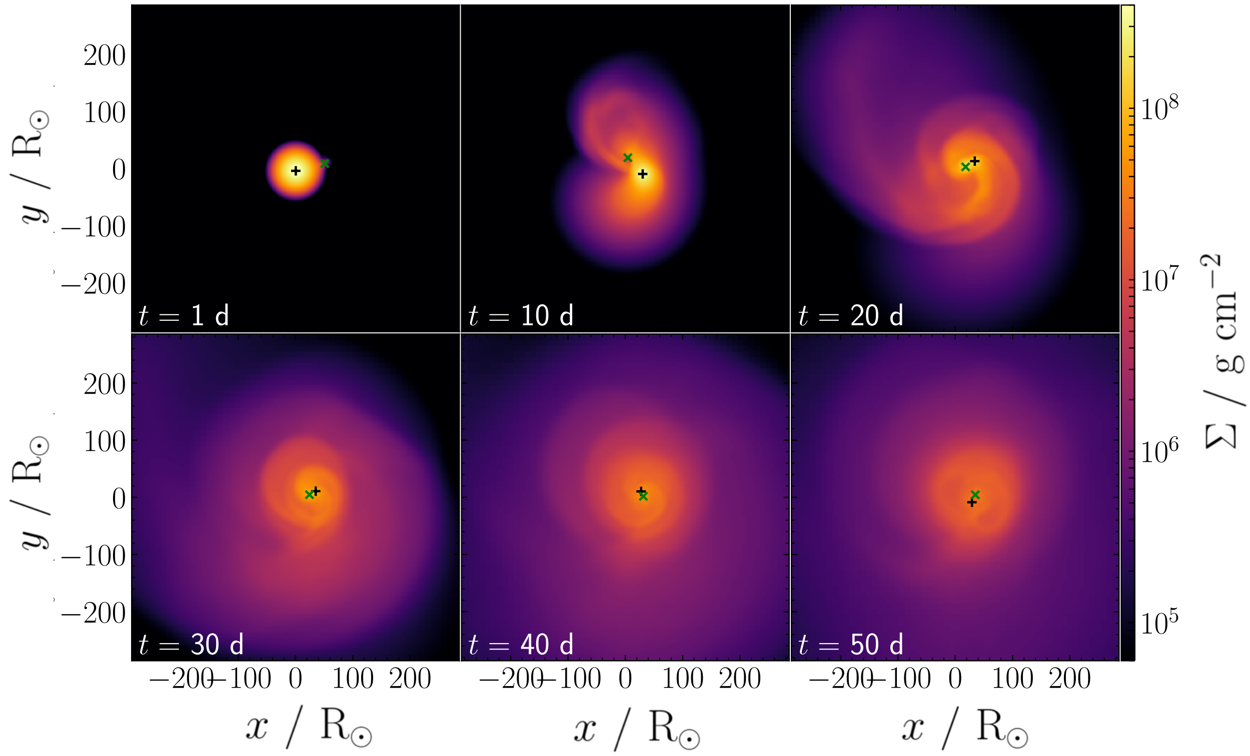

Figure 5.6: Density projections along the z-axis in our CEE simulation with MHD. The $+$ sign marks the red giant core and the $\times$ marks the companion.

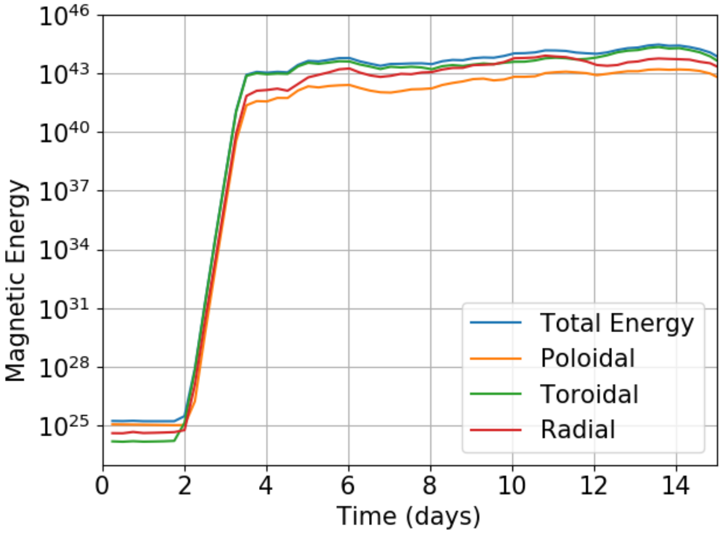

Figure 5.7: The energy in the magnetic field and its spherical components in our CEE simulation. Rapid amplification is seen at the onset of CEE, after which the energies are fairly stable. The majority of the amplification is in the toroidal component of the field.

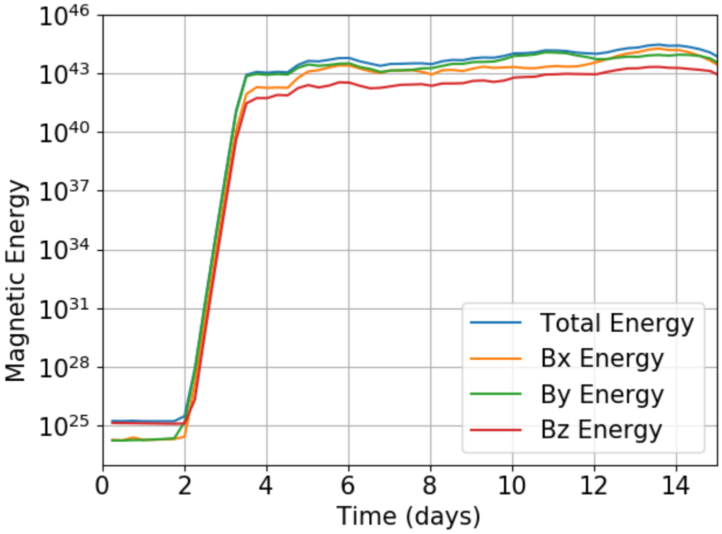

Figure 5.8: The energy in the magnetic field and its components along Cartesian axes in our CEE simulation. The x- and y- components dominate the z-component, indicating that the field is primarily in the orbital plane.

tion is largest by far in the toroidal component of the field. This is consistent with the findings of Ondratschek et al. (2021) who showed that toroidal fields within the envelope are instrumental in the formation of planetary nebulae.

We again show the magnetic field energy and its Cartesian components in Fig. 5.8. Here we see that the x- and y- components of $\boldsymbol{B}$, initially lesser than the z-component due to the initial conditions, dominate after amplification. Their relative strengths change over the course of the simulation due to the non-axisymmetry of the ejecta.

5.6 CONCLUSIONS

We have laid out the principles of ideal MHD and their inclusion into MANGA through modification of the Euler equations and face fluxes. We enfore the divergence constraint $\boldsymbol{\nabla} \cdot \boldsymbol{B} = 0$ through the divergence cleaning scheme of Dedner et al. (2002), which both damps and diffuses magnetic monopoles to ensure that divergence errors remain small. This scheme is found to be stable and to produce accurate results for standard MHD tests including a circularly-polarized Alfvén wave, a magnetic Sedov-Taylor blast wave, and an Orszag-Tang vortex. In particular, the Alfvén wave is shown to converge to the analytic solution. However, the divergence cleaning scheme introduces a global limit on the time-step, which limits performance. We also implement the Powell eight-wave scheme (Powell et al., 1999) for the purposes of comparison.

Before diving into CEE, we first investigate the magnetic field of a static star and find that the Lyutikov field combined with the divergence cleaning scheme yield a stable field. In contrast, the Powell scheme leads to steady growth of the field due to the lack of a damping term, while the dipole field is problematic due to its excessively large values near the origin. We thus initialize a CEE simulation using the Lyutikov field and divergence cleaning scheme. We find a rapid amplification of the field at the onset of CEE, with fairly stable fields before and after. This is consistent with the results of Ohlmann et al. (2016b), who used an initial dipole field as well as the Powell eight-wave scheme. The amplification is dominated by the toroidal field, which is thought to be responsible for the formation of planetary nebulae due to the magnetic pressure it provides within the envelope.

5.7 FUTURE DIRECTIONS: TIDAL DISRUPTION EVENTS

When a star enters the tidal radius of a supermassive black hole (SMBH), the self-gravity of the star is overwhelmed by tidal forces and the star is ripped apart in what is known as a tidal disruption event (TDE). A portion of the stellar material is bound to the SMBH and forms and accretion disk, while the remainder is unbound and escapes to infinity. The accretion rate onto the SMBH peaks at super-Eddington values, resulting in a luminous event which peaks in the UV and X-rays. Theoretical models of such events correspond to X-ray transients observed in recent decades (Komossa, 2015), which can be used to probe several areas of astrophysics such as accretion physics (van Velzen, 2018) and stellar dynamics in galactic cores (Stone et al., 2020).

Spaulding & Chang (2020) used MANGA to investigate TDEs and the effect of the impact parameter β on energy distribution, fallback rate onto the SMBH, and the time of peak luminosity. Here a 1 M$_\odot$ zero-age main sequence (ZAMS) star is disrupted by a 10^6 M$_\odot$ SMBH with varying β. They found that the spread of energy and the peak luminosity time are both directly related to the impact parameter. In particular, they found that the spread in energy scales as $\beta^{1/2}$ for $2 < \beta < 10$ and levels off for $\beta > 10$. MANGA has also been used to study the radio emission from TDEs due to shocking of the ISM by unbound tidal debris (Spaulding & Chang, in preparation). Simulated events were found to have peak radio fluxes and frequencies consistent with observations of

TDEs with non-relativistic outflows (as opposed to TDEs whose emission is powered by relativistic jets).

Currently, the MHD implementation discussed in this chapter is being used to conduct a follow-up study in which the effects of magnetic fields on energy spread and fallback rate. Besides being an interesting study in its own right, the results of these simulations will be used by a group at the University of Virginia to study the magnetic fields in the accretion disk formed as a result of the TDE. This study will use the AMR code Athena++, which can take advantage of the constrained transport formulation of MHD to evolve the magnetic field with zero divergence (White et al., 2016).

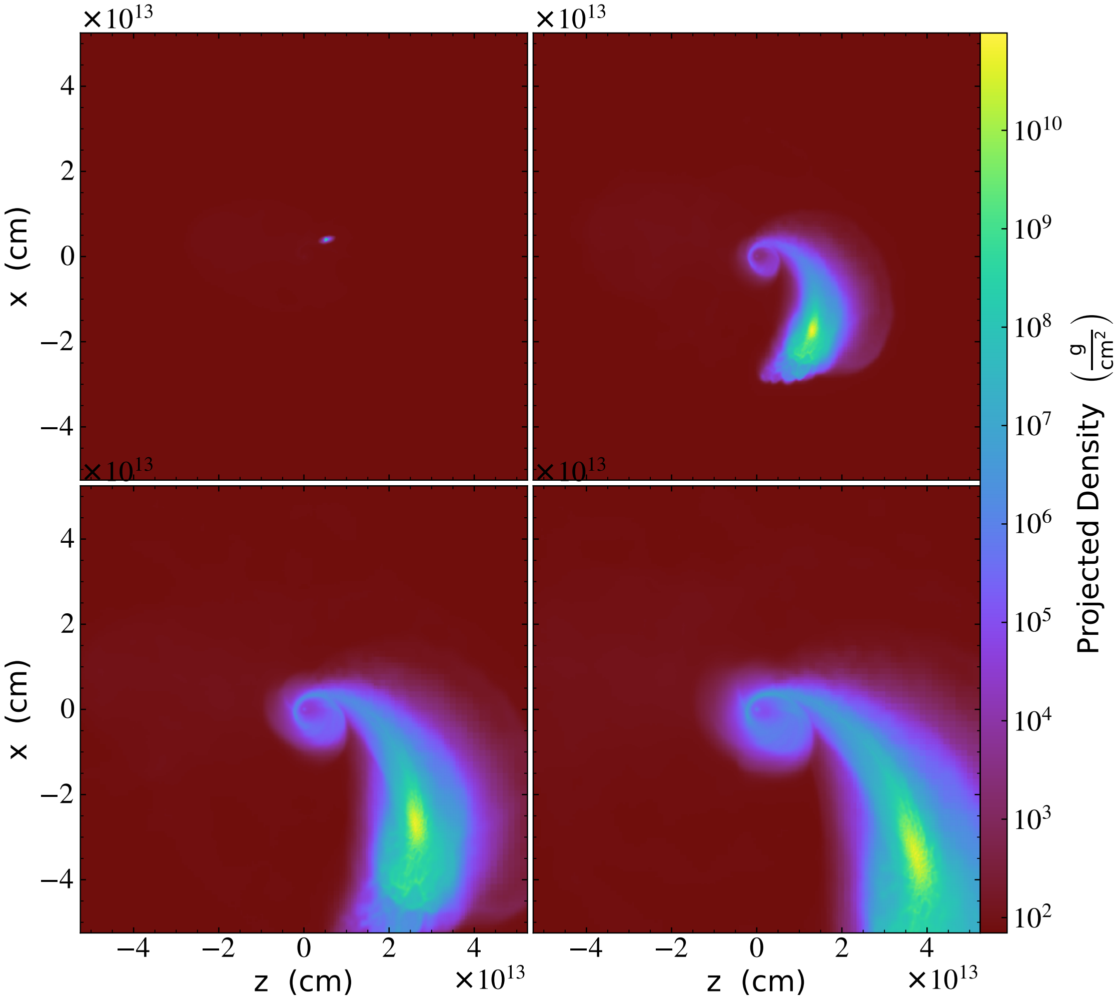

Figure 5.9: Tidal disruption of a $1\ \mathrm{M}_{\odot}$ ZAMS star by a $10^6\ \mathrm{M}_{\odot}$ SMBH with $\beta = 4$ in Spaulding & Chang (2020). Each frame is separated by 1.8 hours.

LIST OF JOURNALS

ApJ . .	The Astrophysical Journal
ApJS .	The Astrophysical Journal Supplement
ARAA	Annual Review of Astronomy and Astrophysics
A&A .	Astronomy & Astrophysics
A&ARv	The Astronomy and Astrophysics Review
MNRAS	Monthly Notices of the Royal Astronomical Society

BIBLIOGRAPHY

Abbott, B., Abbott, R., Adhikari, R., Agresti, J., Ajith, P., Allen, B., Amin, R., Anderson, S. B., Anderson, W. G., Arain, M., Araya, M., Armandula, H., Ashley, M., Aston, S., Aufmuth, P., Aulbert, C., Babak, S., Ballmer, S., Bantilan, H., Barish, B. C., Barker, C., Barker, D., Barr, B., Barriga, P., Barton, M. A., Bayer, K., Belczynski, K., Betzwieser, J., Beyersdorf, P. T., Bhawal, B., Bilenko, I. A., Billingsley, G., Biswas, R., Black, E., Blackburn, K., Blackburn, L., Blair, D., Bland, B., Bogenstahl, J., Bogue, L., Bork, R., Boschi, V., Bose, S., Brady, P. R., Braginsky, V. B., Brau, J. E., Brinkmann, M., Brooks, A., Brown, D. A., Bullington, A., Bunkowski, A., Buonanno, A., Burmeister, O., Busby, D., Butler, W. E., Byer, R. L., Cadonati, L., Cagnoli, G., Camp, J. B., Cannizzo, J., Cannon, K., Cantley, C. A., Cao, J., Cardenas, L., Carter, K., Casey, M. M., Castaldi, G., Cepeda, C., Chalkey, E., Charlton, P., Chatterji, S., Chelkowski, S., Chen, Y., Chiadini, F., Chin, D., Chin, E., Chow, J., Christensen, N., Clark, J., Cochrane, P., Cokelaer, T., Colacino, C. N., Coldwell, R., Conte, R., Cook, D., Corbitt, T., Coward, D., Coyne, D., Creighton, J. D. E., Creighton, T. D., Croce, R. P., Crooks, D. R. M., Cruise, A. M., Cumming, A., Dalrymple, J., D'Ambrosio, E., Danzmann, K., Davies, G., Debra, D., Degallaix, J., Degree, M., Demma, T., Dergachev, V., Desai, S., Desalvo, R., Dhurandhar, S., Díaz, M., Dickson, J., di Credico, A., Diederichs, G., Dietz, A., Doomes, E. E., Drever, R. W. P., Dumas, J. C., Dupuis, R. J., Dwyer, J. G., Ehrens, P., Espinoza, E., Etzel, T., Evans, M., Evans, T., Fairhurst, S., Fan, Y., Fazi, D., Fejer, M. M., Finn, L. S., Fiumara, V., Fotopoulos, N., Franzen, A., Franzen, K. Y., Freise, A., Frey, R., Fricke, T., Fritschel, P., Frolov, V. V., Fyffe, M., Galdi, V., Ganezer, K. S., Garofoli, J., Gholami, I., Giaime, J. A., Giampanis, S., Giardina, K. D., Goda, K., Goetz, E., Goggin, L., González, G., Gossler, S., Grant, A., Gras, S., Gray, C., Gray, M., Greenhalgh, J., Gretarsson, A. M., Grosso, R., Grote, H., Grunewald, S., Guenther, M., Gustafson, R., Hage, B., Hammer, D., Hanna, C., Hanson, J., Harms, J., Harry, G., Harstad, E., Hayler, T., Heefner, J., Heng, I. S., Heptonstall, A., Heurs, M., Hewitson, M., Hild, S., Hirose, E., Hoak, D., Hosken, D., Hough, J., Howell, E., Hoyland, D., Huttner, S. H., Ingram, D., Innerhofer, E., Ito, M., Itoh, Y., Ivanov, A., Jackrel, D., Johnson, B., Johnson, W. W., Jones, D. I., Jones, G., Jones, R., Ju, L., Kalmus, P., Kalogera, V., Kasprzyk, D., Katsavounidis, E., Kawabe, K., Kawamura, S., Kawazoe, F., Kells, W., Keppel, D. G., Khalili, F. Y., Kim, C., King, P., Kissel, J. S., Klimenko, S., Kokeyama, K., Kondrashov, V., Kopparapu, R. K., Kozak, D., Krishnan, B., Kwee, P., Lam, P. K., Landry, M., Lantz, B., Lazzarini, A., Lee, B., Lei, M., Leiner, J., Leonhardt, V., Leonor, I., Libbrecht, K., Lindquist, P., Lockerbie, N. A., Longo, M., Lormand, M., Lubiński, M., Lück, H., Machenschalk, B., Macinnis, M., Mageswaran, M., Mailand, K., Malec, M., Mandic, V., Marano, S., Márka, S., Markowitz, J., Maros, E., Martin, I., Marx, J. N., Mason, K., Matone, L., Matta, V., Mavalvala, N., McCarthy, R., McClelland, D. E., McGuire, S. C., McHugh, M., McKenzie, K., McNabb, J. W. C., McWilliams, S., Meier, T., Melissinos, A., Mendell, G., Mercer, R. A., Meshkov, S., Messaritaki, E., Messenger, C. J., Meyers, D., Mikhailov, E., Mitra, S., Mitrofanov, V. P., Mitselmakher, G., Mittleman, R., Miyakawa, O., Mohanty, S., Moreno, G., Mossavi, K., Mowlowry, C., Moylan, A., Mudge, D., Mueller, G., Mukherjee, S., Müller-Ebhardt, H., Munch, J., Murray, P., Myers, E., Myers, J., Nash, T., Newton, G., Nishizawa, A., Nocera, F., Numata, K., O'Reilly, B., O'Shaughnessy, R., Ottaway, D. J., Overmier, H., Owen, B. J., Pan, Y., Papa, M. A., Parameshwaraiah, V., Parameswariah, C., Patel, P., Pedraza, M., Penn, S., Pierro, V., Pinto, I. M., Pitkin, M., Pletsch, H., Plissi, M. V., Postiglione, F., Prix, R., Quetschke, V., Raab, F., Rabeling, D., Radkins, H., Rahkola, R., Rainer, N., Rakhmanov, M., Rawlins, K., Ray-Majumder, S., Re, V., Regimbau, T., Rehbein, H., Reid, S., Reitze, D. H., Ribichini, L., Riesen, R., Riles, K., Rivera, B., Robertson, N. A., Robinson, C., Robinson, E. L., Roddy, S., Rodriguez, A., Rogan, A. M., Rollins, J., Romano, J. D., Romie, J., Route, R., Rowan, S., Rüdiger, A., Ruet, L., Russell, P., Ryan, K., Sakata, S., Samidi, M., de La Jordana, L. S., Sandberg, V., Sanders, G. H., Sannibale, V., Saraf, S., Sarin, P., Sathyaprakash, B. S., Sato, S., Saulson, P. R., Savage, R., Savov, P., Sazonov, A., Schediwy, S., Schilling, R., Schnabel, R., Schofield, R., Schutz, B. F., Schwinberg, P., Scott, S. M., Searle, A. C., Sears, B., Seifert, F., Sellers, D., Sengupta, A. S., Shawhan, P., Shoemaker, D. H., Sibley, A., Sidles, J. A., Siemens, X., Sigg, D., Sinha, S., Sintes, A. M., Slagmolen, B. J. J., Slutsky, J., Smith, J. R., Smith, M. R., Somiya, K., Strain, K. A., Strom, D. M., Stuver, A., Summerscales, T. Z., Sun, K. X., Sung, M., Sutton, P. J., Takahashi, H., Tanner, D. B., Tarallo, M., Taylor, R., Taylor, R., Thacker, J., Thorne, K. A., Thorne, K. S., Thüring, A., Tokmakov, K. V., Torres, C., Torrie, C., Traylor, G., Trias, M., Tyler, W., Ugolini, D., Ungarelli, C., Urbanek, K., Vahlbruch, H., Vallisneri, M., van den Broeck, C., van Putten, M., Varvella, M., Vass, S., Vecchio, A., Veitch, J., Veitch, P., Villar, A., Vorvick, C., Vyachanin, S. P., Waldman, S. J., Wallace, L., Ward, H., Ward, R., Watts, K., Webber, D., Weidner, A., Weinert, M., Weinstein, A., Weiss, R., Wen, S., Wette, K., Whelan, J. T., Whitbeck, D. M., Whitcomb, S. E., Whiting, B. F., Wiley, S., Wilkinson, C., Willems, P. A., Williams, L., Willke, B., Wilmut, I., Winkler, W., Wipf, C. C., Wise, S., Wiseman, A. G., Woan, G., Woods, D., Wooley, R., Worden, J., Wu, W., Yakushin, I., Yamamoto, H., Yan, Z., Yoshida, S., Yunes, N., Zanolin, M., Zhang, J., Zhang, L., Zhao, C., Zotov, N., Zucker, M., Zur Mühlen, H., & Zweizig, J. (2008). Search for gravitational waves from binary inspirals in S3 and S4 LIGO data. Phys. Rev. D, 77(6), 062002.

Abbott, B. P., Abbott, R., Abbott, T. D., Abernathy, M. R., Acernese, F., Ackley, K., Adams, C., Adams, T., Addesso, P., Adhikari, R. X., & et al. (2016). Observation of Gravitational Waves from a Binary Black Hole Merger. Physical Review Letters, 116(6), 061102.

Abbott, B. P., Abbott, R., Abbott, T. D., Abraham, S., Acernese, F., Ackley, K., Adams, C., Adhikari, R. X., Adya, V. B., Affeldt, C., & et al. (2019). GWTC-1: A Gravitational-Wave Transient Catalog of Compact Binary Mergers Observed by LIGO and Virgo during the First and Second Observing Runs. Physical Review X, 9(3), 031040.

Acernese, F., Amico, P., Alshourbagy, M., Antonucci, F., Aoudia, S., Avino, S., Babusci, D., Ballardin, G., Barone, F., Barsotti, L., Barsuglia, M., Beauville, F., Bigotta, S., Birindelli, S., Bizouard, M. A., Boccara, C., Bondu, F., Bosi, L., Bradaschia, C., Braccini, S., Brillet, A., Brisson, V., Brocco, L., Buskulic, D., Calloni, E., Campagna, E., Cavalier, F., Cavalieri, R., Cella, G., Cesarini, E., Chassande-Mottin, E., Corda, C., Cottone, F., Clapson, A. C., Cleva, F., Coulon, J. P., Cuoco, E., Dari, A., Dattilo, V., Davier, M., De Rosa, R., Di Fiore, L., Di Virgilio, A., Dujardin, B., Eleuteri, A., Enard, D., Ferrante, I., Fidecaro, F., Fiori, I., Flaminio, R., Fournier, J. D., Francois, O., Frasca, S., Frasconi, F., Freise, A., Gammaitoni, L., Garufi, F., Gennai, A., Giazotto, A., Giordano, G., Giordano, L., Gouaty, R., Grosjean, D., Guidi, G., Hebri, S., Heitmann, H., Hello, P., Holloway, L., Karkar, S., Kreckelbergh, S., La Penna, P., Laval, M., Leroy, N., Letendre, N., Lorenzini, M., Loriette, V., Loupias, M., Losurdo, G., Mackowski, J. M., Majorana, E., Man, C. N., Mantovani, M., Marchesoni, F., Marion, F., Marque, J., Martelli, F., Masserot, A., Mazzoni, M., Milano, L., Moins, C., Moreau, J., Morgado, N., Mours, B., Pai, A., Palomba, C., Paoletti, F., Pardi, S., Pasqualetti, A., Passaquieti, R., Passuello, D., Perniola, B., Piergiovanni, F., Pinard, L., Poggiani, R., Punturo, M., Puppo, P., Qipiani, K., Rapagnani, P., Reita, V., Remillieux, A., Ricci, F., Ricciardi, I., Ruggi, P., Russo, G., Solimeno, S., Spallicci, A., Stanga, R., Taddei, R., Tonelli, M., Toncelli, A., Tournefier, E., Travasso, F., Vajente, G., Verkindt, D., Vetrano, F., Viceré, A., Vinet, J. Y., Vocca, H., Yvert, M., & Zhang, Z. (2006). The Virgo status. Classical and Quantum Gravity, 23(19), S635–S642.

Agertz, O., Moore, B., Stadel, J., Potter, D., Miniati, F., Read, J., Mayer, L., Gawryszczak, A., Kravtsov, A., Nordlund, Å., Pearce, F., Quilis, V., Rudd, D., Springel, V., Stone, J., Tasker, E., Teyssier, R., Wadsley, J., & Walder, R. (2007). Fundamental differences between SPH and grid methods. MNRAS, 380, 963–978.

Antonini, F., & Rasio, F. A. (2016). Merging Black Hole Binaries in Galactic Nuclei: Implications for Advanced-LIGO Detections. ApJ, 831, 187.

Balbus, S. A., & Hawley, J. F. (1998). Instability, turbulence, and enhanced transport in accretion disks. Reviews of Modern Physics, 70(1), 1–53.

Balsara, D. S. (1995). von Neumann stability analysis of smooth particle hydrodynamics–suggestions for optimal algorithms. Journal of Computational Physics, 121, 357–372.

Barnes, J., & Hut, P. (1986). A hierarchical O(N log N) force-calculation algorithm. Nature, 324, 446–449.

Belczynski, K., Holz, D. E., Bulik, T., & O'Shaughnessy, R. (2016). The first gravitational-wave source from the isolated evolution of two stars in the 40-100 solar mass range. Nature, 534, 512–515.

Bond, H. E. (2000). Binarity of Central Stars of Planetary Nebulae. In J. H. Kastner, N. Soker, & S. Rappaport (Eds.) Asymmetrical Planetary Nebulae II: From Origins to Microstructures, vol. 199 of Astronomical Society of the Pacific Conference Series, (p. 115).

Bond, H. E., Henden, A., Levay, Z. G., Panagia, N., Sparks, W. B., Starrfield, S., Wagner, R. M., Corradi, R. L. M., & Munari, U. (2003). An energetic stellar outburst accompanied by circumstellar light echoes. Nature, 422, 405–408.

Bowen, G. H. (1988). Dynamical Modeling of Long-Period Variable Star Atmospheres. ApJ, 329, 299.

Bryan, G. L., Norman, M. L., O'Shea, B. W., Abel, T., Wise, J. H., Turk, M. J., Reynolds, D. R., Collins, D. C., Wang, P., Skillman, S. W., Smith, B., Harkness, R. P., Bordner, J., Kim, J.-h., Kuhlen, M., Xu, H., Goldbaum, N., Hummels, C., Kritsuk, A. G., Tasker, E., Skory, S., Simpson, C. M., Hahn, O., Oishi, J. S., So, G. C., Zhao, F., Cen, R., Li, Y., & The Enzo Collaboration (2014). ENZO: An Adaptive Mesh Refinement Code for Astrophysics. ApJS, 211, 19.

Chamandy, L., Blackman, E. G., Frank, A., Carroll-Nellenback, J., Zou, Y., & Tu, Y. (2019). How drag force evolves in global common envelope simulations. MNRAS, 490(3), 3727–3739.

Chamandy, L., Frank, A., Blackman, E. G., Carroll- Nellenback, J., Liu, B., Tu, Y., Nordhaus, J., Chen, Z., & Peng, B. (2018). Accretion in common envelope evolution. MNRAS, (p. 1849).

Chang, P., Davis, S. W., & Jiang, Y.-F. (2020). Time-dependent radiation hydrodynamics on a moving mesh. MNRAS, 493(4), 5397–5407.

Chang, P., & Etienne, Z. B. (2020). General relativistic hydrodynamics on a moving-mesh I: static space-times. MNRAS, 496(1), 206–214.

Chang, P., Wadsley, J., & Quinn, T. (2017). A Moving Mesh Hydrodynamics Solver for ChaNGa. accepted to MNRAS.

Chatterjee, S., Rodriguez, C. L., Kalogera, V., & Rasio, F. A. (2017). Dynamical Formation of Low-mass Merging Black Hole Binaries like GW151226. ApJ, 836, L26.

Chen, Z., Ivanova, N., & Carroll-Nellenback, J. (2020). A 3D Radiation Hydrodynamic AGB Binary Model. ApJ, 892(2), 110.

Chorin, A. J., & Marsden, J. E. (1993). A Mathematical Introduction to Fluid Mechanics.

Cooray, A. (2004). Gravitational-wave background of neutron star-white dwarf binaries. MNRAS, 354(1), 25–30.

Cowling, T. G., & Lindsay, R. B. (1957). Magnetohydrodynamics. Physics Today, 10(9), 40.

Darwin, G. H. (1879). The Determination of the Secular Effects of Tidal Friction by a Graphical Method. Proceedings of the Royal Society of London Series I, 29, 168–181.

De, S., MacLeod, M., Everson, R. W., Antoni, A., Mandel, I., & Ramirez-Ruiz, E. (2020). Common Envelope Wind Tunnel: The Effects of Binary Mass Ratio and Implications for the Accretion-driven Growth of LIGO Binary Black Holes. ApJ, 897(2), 130.

de Kool, M. (1987). Models of interacting binary stars. Ph.D. thesis, University of Amsterdam.

de Kool, M. (1990). Common Envelope Evolution and Double Cores of Planetary Nebulae. ApJ, 358, 189.

de Mink, S. E., & Mandel, I. (2016). The chemically homogeneous evolutionary channel for binary black hole mergers: rates and properties of gravitational-wave events detectable by advanced LIGO. MNRAS, 460, 3545–3553.

Dedner, A., Kemm, F., Kröner, D., Munz, C. D., Schnitzer, T., & Wesenberg, M. (2002). Hyperbolic Divergence Cleaning for the MHD Equations. Journal of Computational Physics, 175(2), 645–673.

Demorest, P. B., Pennucci, T., Ransom, S. M., Roberts, M. S. E., & Hessels, J. W. T. (2010). A two-solar-mass neutron star measured using Shapiro delay. Nature, 467(7319), 1081–1083.

Dewi, J. D. M., & Tauris, T. M. (2000). On the energy equation and efficiency parameter of the common envelope evolution. A&A, 360, 1043–1051.

Dewi, J. D. M., & Tauris, T. M. (2001). On the λ-Parameter of the Common Envelope Evolution. In P. Podsiadlowski, S. Rappaport, A. R. King, F. D'Antona, & L. Burderi (Eds.) Evolution of Binary and Multiple Star Systems, vol. 229 of Astronomical Society of the Pacific Conference Series, (p. 255).

Dolag, K., Borgani, S., Schindler, S., Diaferio, A., & Bykov, A. M. (2008). Simulation Techniques for Cosmological Simulations. , 134(1-4), 229–268.

Donea, J., Huerta, A., Ponthot, J.-P., & Rodríguez-Ferran, A. (2004). Arbitrary Lagrangian Eulerian Methods. John Wiley & Sons, Ltd.

Duez, M. D. (2010). Numerical relativity confronts compact neutron star binaries: a review and status report. Classical and Quantum Gravity, 27(11), 114002.

Duffell, P. C., & MacFadyen, A. I. (2011). TESS: A Relativistic Hydrodynamics Code on a Moving Voronoi Mesh. ApJS, 197, 15.

Einfeldt, B. (1988). On Godunov-Type Methods for Gas Dynamics. SIAM Journal on Numerical Analysis, 25(2), 294–318.

Etienne, Z. B., Liu, Y. T., & Shapiro, S. L. (2010). Relativistic magnetohydrodynamics in dynamical spacetimes: A new adaptive mesh refinement implementation. Phys. Rev. D, 82(8), 084031.

Etienne, Z. B., Liu, Y. T., Shapiro, S. L., & Baumgarte, T. W. (2009). General relativistic simulations of black-hole-neutron-star mergers: Effects of black-hole spin. Phys. Rev. D, 79(4), 044024.

Evans, C. R., & Hawley, J. F. (1988). Simulation of Magnetohydrodynamic Flows: A Constrained Transport Model. ApJ, 332, 659.

Fryer, C. L., Mazzali, P. A., Prochaska, J., Cappellaro, E., Panaitescu, A., Berger, E., van Putten, M., van den Heuvel, E. P. J., Young, P., Hungerford, A., Rockefeller, G., Yoon, S.-C., Podsiadlowski, P., Nomoto, K., Chevalier, R., Schmidt, B., & Kulkarni, S. (2007). Constraints on Type Ib/c Supernovae and Gamma-Ray Burst Progenitors. PASP, 119(861), 1211–1232.

Fryer, C. L., Woosley, S. E., & Hartmann, D. H. (1999). Formation Rates of Black Hole Accretion Disk Gamma-Ray Bursts. ApJ, 526(1), 152–177.

Fryxell, B., Olson, K., Ricker, P., Timmes, F. X., Zingale, M., Lamb, D. Q., MacNeice, P., Rosner, R., Truran, J. W., & Tufo, H. (2000). FLASH: An Adaptive Mesh Hydrodynamics Code for Modeling Astrophysical Thermonuclear Flashes. ApJS, 131, 273–334.

Gaburov, E., Johansen, A., & Levin, Y. (2012). Magnetically Levitating Accretion Disks around Supermassive Black Holes. ApJ, 758, 103.

Gammie, C. F., McKinney, J. C., & Tóth, G. (2003). HARM: A Numerical Scheme for General Relativistic Magnetohydrodynamics. ApJ, 589(1), 444–457.

Giacobbo, N., & Mapelli, M. (2018). The progenitors of compact-object binaries: impact of metallicity, common envelope and natal kicks. MNRAS, 480, 2011–2030.

Gianninas, A., Dufour, P., Kilic, M., Brown, W. R., Bergeron, P., & Hermes, J. J. (2014). Precise Atmospheric Parameters for the Shortest-period Binary White Dwarfs: Gravitational Waves, Metals, and Pulsations. ApJ, 794, 35.

Gingold, R. A., & Monaghan, J. J. (1977). Smoothed particle hydrodynamics: theory and application to non-spherical stars. MNRAS, 181, 375–389.

Glanz, H., & Perets, H. B. (2018). Efficient common-envelope ejection through dust-driven winds. MNRAS, 478, L12–L17.

Gnedin, N. Y. (1995). Softened Lagrangian hydrodynamics for cosmology. ApJS, 97, 231–257.

González, M., Audit, E., & Huynh, P. (2007). HERACLES: a three-dimensional radiation hydrodynamics code. A&A, 464(2), 429–435.

Grichener, A., Sabach, E., & Soker, N. (2018). The limited role of recombination energy in common envelope removal. MNRAS, 478, 1818–1824.

Guillochon, J., & Ramirez-Ruiz, E. (2013). Hydrodynamical Simulations to Determine the Feeding Rate of Black Holes by the Tidal Disruption of Stars: The Importance of the Impact Parameter and Stellar Structure. ApJ, 767, 25.

Han, Z., Podsiadlowski, P., & Eggleton, P. P. (1995). The formation of bipolar planetary nebulae and close white dwarf binaries. MNRAS, 272(4), 800–820.

Han, Z., Podsiadlowski, P., Maxted, P. F. L., Marsh, T. R., & Ivanova, N. (2002). The origin of subdwarf B stars - I. The formation channels. MNRAS, 336(2), 449–466.

Harten, A., Lax, P. D., & Leer, B. v. (1983). On upstream differencing and godunov-type schemes for hyperbolic conservation laws. SIAM Review, 25(1), 35–61.

Hedayat, M., & Borazjani, I. (2019). A parallel dynamic overset grid framework for immersed boundary methods. arXiv e-prints, (p. arXiv:1910.09315).

Heinzel, G., Braxmaier, C., Danzmann, K., Gath, P., Hough, J., Jennrich, O., Johann, U., Rüdiger, A., Sallusti, M., & Schulte, H. (2006). LISA interferometry: recent developments. Classical and Quantum Gravity, 23(8), S119–S124.

Hernquist, L., & Katz, N. (1989). TREESPH: A Unification of SPH with the Hierarchical Tree Method. ApJS, 70, 419.

Hinder, I. (2010). The current status of binary black hole simulations in numerical relativity. Classical and Quantum Gravity, 27(11), 114004.

Hockney, R. W., & Eastwood, J. W. (1981). Computer Simulation Using Particles.

Hoyle, F., & Lyttleton, R. A. (1939). The effect of interstellar matter on climatic variation. Proceedings of the Cambridge Philosophical Society, 35(3), 405.

Iaconi, R., De Marco, O., Passy, J.-C., & Staff, J. (2018). The effect of binding energy and resolution in simulations of the common envelope binary interaction. MNRAS, 477(2), 2349–2365.

Iben, J., I., & Tutukov, A. V. (1984). Supernovae of type I as end products of the evolution of binaries with components of moderate initial mass. ApJS, 54, 335–372.

Iben, J., Icko, & Livio, M. (1993). Common Envelopes in Binary Star Evolution. PASP, 105, 1373.

Ivanova, N. (2002). Slow mergers of massive stars. Ph.D. thesis, University of Oxford, UK.

Ivanova, N. (2011). Common Envelope: The Progress and the Pitfalls. In L. Schmidtobreick, M. R. Schreiber, & C. Tappert (Eds.) Evolution of Compact Binaries, vol. 447 of Astronomical Society of the Pacific Conference Series, (p. 91).

Ivanova, N. (2017). Common envelope: progress and transients. ArXiv e-prints.

Ivanova, N. (2018). On the Use of Hydrogen Recombination Energy during Common Envelope Events. ApJ, 858, L24.

Ivanova, N., Justham, S., Chen, X., De Marco, O., Fryer, C. L., Gaburov, E., Ge, H., Glebbeek, E., Han, Z., Li, X.-D., Lu, G., Marsh, T., Podsiadlowski, P., Potter, A., Soker, N., Taam, R., Tauris, T. M., van den Heuvel, E. P. J., & Webbink, R. F. (2013). Common envelope evolution: where we stand and how we can move forward. A&A Rev., 21, 59.

Ivanova, N., Podsiadlowski, P., & Spruit, H. (2002). Hydrodynamical simulations of the stream-core interaction in the slow merger of massive stars. MNRAS, 334(4), 819–832.

Jetley, P., Gioachin, F., Mendes, C., Kale, L. V., & Quinn, T. R. (2008). "massively parallel cosmological simulations with changa". Proceedings of IEEE International Parallel and Distributed Processing Symposium.

Jetley, P., Wesolowski, F., Gioachin, F., Kale, L. V., & Quinn, T. R. (2010). "scaling hierarchical n-body simulations on gpu clusters". Proceedings of the 2010 ACM/IEEE International Conference for High Performance Computing.

Jiang, Y.-F. (2021). An Implicit Finite Volume Scheme to Solve the Time-dependent Radiation Transport Equation Based on Discrete Ordinates. ApJS, 253(2), 49.

Jiang, Y.-F., Stone, J. M., & Davis, S. W. (2014). An Algorithm for Radiation Magnetohydrodynamics Based on Solving the Time-dependent Transfer Equation. ApJS, 213(1), 7.

Kale, L. V., & Krishnan, S. (1996). Charm++: Parallel Programming with Message-Driven Objects. In G. V. Wilson, & P. Lu (Eds.) Parallel Programming using C++, (pp. 175–213). MIT Press.

Kannan, R., Vogelsberger, M., Marinacci, F., McKinnon, R., Pakmor, R., & Springel, V. (2019). AREPO-RT: radiation hydrodynamics on a moving mesh. MNRAS, 485(1), 117–149.

Kasliwal, M. M. (2013). Systematically Bridging the Gap between Novae and Supernovae. In R. Di Stefano, M. Orio, & M. Moe (Eds.) Binary Paths to Type Ia Supernovae Explosions, vol. 281 of IAU Symposium, (pp. 9–16).

Kasliwal, M. M., Kulkarni, S. R., Arcavi, I., Quimby, R. M., Ofek, E. O., Nugent, P., Jacobsen, J., Gal-Yam, A., Green, Y., Yaron, O., Fox, D. B., Howell, J. L., Cenko, S. B., Kleiser, I., Bloom, J. S., Miller, A., Li, W., Filippenko, A. V., Starr, D., Poznanski, D., Law, N. M., Helou, G., Frail, D. A., Neill, J. D., Forster, K., Martin, D. C., Tendulkar, S. P., Gehrels, N., Kennea, J., Sullivan, M., Bildsten, L., Dekany, R., Rahmer, G., Hale, D., Smith, R., Zolkower, J., Velur, V., Walters, R., Henning, J., Bui, K., McKenna, D., & Blake, C. (2011). PTF 10fqs: A Luminous Red Nova in the Spiral Galaxy Messier 99. ApJ, 730, 134.

Kerzendorf, W. E., & Sim, S. A. (2014). A spectral synthesis code for rapid modelling of supernovae. MNRAS, 440(1), 387–404.

Komossa, S. (2015). Tidal disruption of stars by supermassive black holes: Status of observations. Journal of High Energy Astrophysics, 7, 148–157.

Kruckow, M. U., Tauris, T. M., Langer, N., Szécsi, D., Marchant, P., & Podsiadlowski, P. (2016). Common-envelope ejection in massive binary stars. Implications for the progenitors of GW150914 and GW151226. A&A, 596, A58.

Kulkarni, S. R., Ofek, E. O., Rau, A., Cenko, S. B., Soderberg, A. M., Fox, D. B., Gal-Yam, A., Capak, P. L., Moon, D. S., Li, W., Filippenko, A. V., Egami, E., Kartaltepe, J., & Sanders, D. B. (2007). An unusually brilliant transient in the galaxy M85. Nature, 447, 458–460.

Law-Smith, J. A. P., Everson, R. W., Ramirez-Ruiz, E., de Mink, S. E., van Son, L. A. C., Götberg, Y., Zellmann, S., Vigna-Gómez, A., Renzo, M., Wu, S., Schrøder, S. L., Foley, R. J., & Hutchinson-Smith, T. (2020). Successful Common Envelope Ejection and Binary Neutron Star Formation in 3D Hydrodynamics. arXiv e-prints, (p. arXiv:2011.06630).

Leighton, R. B. (1964). Transport of Magnetic Fields on the Sun. ApJ, 140, 1547.

Livio, M., & Soker, N. (1988). The common envelope phase in the evolution of binary stars. ApJ, 329, 764–779.

López-Cámara, D., De Colle, F., & Moreno Méndez, E. (2018). Self-regulating jets during the Common Envelope phase. ArXiv e-prints, (p. arXiv:1806.11115).

Lucy, L. B. (1967). Formation of Planetary Nebulae. AJ, 72, 813.

Lyutikov, M. (2010). Structure of magnetic fields in non-convective stars. MNRAS, 402(1), 345–352.

MacLeod, M., Antoni, A., Murguia-Berthier, A., Macias, P., & Ramirez-Ruiz, E. (2017a). Common Envelope Wind Tunnel: Coefficients of Drag and Accretion in a Simplified Context for Studying Flows around Objects Embedded within Stellar Envelopes. ApJ, 838(1), 56.

MacLeod, M., Macias, P., Ramirez-Ruiz, E., Grindlay, J., Batta, A., & Montes, G. (2017b). Lessons from the Onset of a Common Envelope Episode: the Remarkable M31 2015 Luminous Red Nova Outburst. ApJ, 835, 282.

MacLeod, M., Ostriker, E. C., & Stone, J. M. (2018). Runaway Coalescence at the Onset of Common Envelope Episodes. ApJ, 863, 5.

MacLeod, M., & Ramirez-Ruiz, E. (2015a). Asymmetric Accretion Flows within a Common Envelope. ApJ, 803(1), 41.

MacLeod, M., & Ramirez-Ruiz, E. (2015b). On the Accretion-fed Growth of Neutron Stars during Common Envelope. ApJ, 798, L19.

Mandel, I., & Farmer, A. (2018). Merging stellar-mass binary black holes. arXiv e-prints, (p. arXiv:1806.05820).

Marchant, P., Langer, N., Podsiadlowski, P., Tauris, T. M., & Moriya, T. J. (2016). A new route towards merging massive black holes. A&A, 588, A50.

Matsumoto, T., & Metzger, B. D. (2022). Light Curve Model for Luminous Red Novae and Inferences about the Ejecta of Stellar Mergers. arXiv e-prints, (p. arXiv:2202.10478).

Menon, H., Wesolowski, L., Zheng, G., Jetley, P., Kale, L., Quinn, T., & Governato, F. (2015). Adaptive techniques for clustered N-body cosmological simulations. Computational Astrophysics and Cosmology, 2, 1.

Meyer, F., & Meyer-Hofmeister, E. (1979). Formation of cataclysmic binaries through common envelope evolution. A&A, 78, 167–176.

Meyer, R. F. (1957). The impact of a shock wave on a movable wall. Journal of Fluid Mechanics, 3, 309–323.

Mocz, P., Pakmor, R., Springel, V., Vogelsberger, M., Marinacci, F., & Hernquist, L. (2016). A moving mesh unstaggered constrained transport scheme for magnetohydrodynamics. MNRAS, 463, 477–488.

Mocz, P., Vogelsberger, M., & Hernquist, L. (2014). A constrained transport scheme for MHD on unstructured static and moving meshes. MNRAS, 442, 43–55.

Monaghan, J. J. (1985). Particle methods for hydrodynamics. Computer Physics Reports, 3(2), 71–124.

Monaghan, J. J. (1992). Smoothed particle hydrodynamics. ARAA, 30, 543–574.

Monaghan, J. J. (1997). SPH and Riemann Solvers. Journal of Computational Physics, 136(2), 298–307.

Monaghan, J. J., & Gingold, R. A. (1983). Shock Simulation by the Particle Method SPH. Journal of Computational Physics, 52(2), 374–389.

Moreno Méndez, E., López-Cámara, D., & De Colle, F. (2017). Dynamics of jets during the common-envelope phase. MNRAS, 470, 2929–2937.

Nandez, J. L. A., & Ivanova, N. (2016). Common envelope events with low-mass giants: understanding the energy budget. MNRAS, 460, 3992–4002.

Nandez, J. L. A., Ivanova, N., & Lombardi, J. C. (2015). Recombination energy in double white dwarf formation. MNRAS, 450, L39–L43.

Nelemans, G., & Tout, C. A. (2005). Reconstructing the evolution of white dwarf binaries: further evidence for an alternative algorithm for the outcome of the common-envelope phase in close binaries. MNRAS, 356, 753–764.

Nelemans, G., Verbunt, F., Yungelson, L. R., & Portegies Zwart, S. F. (2000). Reconstructing the evolution of double helium white dwarfs: envelope loss without spiral-in. A&A, 360, 1011–1018.

Nelemans, G., Yungelson, L. R., & Portegies Zwart, S. F. (2001). The gravitational wave signal from the Galactic disk population of binaries containing two compact objects. A&A, 375, 890–898.

Ohlmann, S. T., Röpke, F. K., Pakmor, R., & Springel, V. (2016a). Hydrodynamic Moving-mesh Simulations of the Common Envelope Phase in Binary Stellar Systems. ApJ, 816, L9.

Ohlmann, S. T., Röpke, F. K., Pakmor, R., Springel, V., & Müller, E. (2016b). Magnetic field amplification during the common envelope phase. MNRAS, 462(1), L121–L125.

Okabe, A., Boots, B., & Sugihara, K. (1992). Spatial tessellations. Concepts and Applications of Voronoi

Ondratschek, P. A., Roepke, F. K., Schneider, F. R. N., Fendt, C., Sand, C., Ohlmann, S. T., Pakmor, R., & Springel, V. (2021). Bipolar planetary nebulae from common envelope evolution of binary stars. arXiv e-prints, (p. arXiv:2110.13177).

Orszag, S. A., & Tang, C. M. (1979). Small-scale structure of two-dimensional magnetohydrodynamic turbulence. Journal of Fluid Mechanics, 90, 129–143.

Paczyński, B., & Ziółkowski, J. (1968). On the Origin of Planetary Nebulae and Mira Variables. , 18, 255.

Pakmor, R., Bauer, A., & Springel, V. (2011). Magnetohydrodynamics on an unstructured moving grid. MNRAS, 418, 1392–1401.

Pakmor, R., & Springel, V. (2013). Simulations of magnetic fields in isolated disc galaxies. MNRAS, 432(1), 176–193.

Pakmor, R., Springel, V., Bauer, A., Mocz, P., Munoz, D. J., Ohlmann, S. T., Schaal, K., & Zhu, C. (2016). Improving the convergence properties of the moving-mesh code AREPO. MNRAS, 455, 1134–1143.

Papish, O., Soker, N., & Bukay, I. (2015). Ejecting the envelope of red supergiant stars with jets launched by an inspiralling neutron star. MNRAS, 449, 288–295.

Paschalidis, V., Liu, Y. T., Etienne, Z., & Shapiro, S. L. (2011). Merger of binary white dwarf-neutron stars: Simulations in full general relativity. Phys. Rev. D, 84(10), 104032.

Paschalidis, V., MacLeod, M., Baumgarte, T. W., & Shapiro, S. L. (2009). Merger of white dwarf-neutron star binaries: Prelude to hydrodynamic simulations in general relativity. Phys. Rev. D, 80(2), 024006.

Passy, J.-C., De Marco, O., Fryer, C. L., Herwig, F., Diehl, S., Oishi, J. S., Mac Low, M.-M., Bryan, G. L., & Rockefeller, G. (2012). Simulating the Common Envelope Phase of a Red Giant Using Smoothed-particle Hydrodynamics and Uniform-grid Codes. ApJ, 744, 52.

Paxton, B., Bildsten, L., Dotter, A., Herwig, F., Lesaffre, P., & Timmes, F. (2011). Modules for Experiments in Stellar Astrophysics (MESA). ApJS, 192, 3.

Paxton, B., Cantiello, M., Arras, P., Bildsten, L., Brown, E. F., Dotter, A., Mankovich, C., Montgomery, M. H., Stello, D., Timmes, F. X., & Townsend, R. (2013). Modules for Experiments in Stellar Astrophysics (MESA): Planets, Oscillations, Rotation, and Massive Stars. ApJS, 208, 4.

Paxton, B., Marchant, P., Schwab, J., Bauer, E. B., Bildsten, L., Cantiello, M., Dessart, L., Farmer, R., Hu, H., Langer, N., Townsend, R. H. D., Townsley, D. M., & Timmes, F. X. (2015). Modules for Experiments in Stellar Astrophysics (MESA): Binaries, Pulsations, and Explosions. ApJS, 220, 15.

Paxton, B., Schwab, J., Bauer, E. B., Bildsten, L., Blinnikov, S., Duffell, P., Farmer, R., Goldberg, J. A., Marchant, P., Sorokina, E., Thoul, A., Townsend, R. H. D., & Timmes, F. X. (2018). Modules for Experiments in Stellar Astrophysics (MESA): Convective Boundaries, Element Diffusion, and Massive Star Explosions. ApJS, 234(2), 34.

Paxton, B., Smolec, R., Schwab, J., Gautschy, A., Bildsten, L., Cantiello, M., Dotter, A., Farmer, R., Goldberg, J. A., Jermyn, A. S., Kanbur, S. M., Marchant, P., Thoul, A., Townsend, R. H. D., Wolf, W. M., Zhang, M., & Timmes, F. X. (2019). Modules for

Experiments in Stellar Astrophysics (MESA): Pulsating Variable Stars, Rotation, Convective Boundaries, and Energy Conservation. ApJS, 243(1), 10.

Pearce, F. R., & Couchman, H. M. P. (1997). Hydra: a parallel adaptive grid code. New Ast., 2(5), 411–427.

Pen, U.-L. (1998). A High-Resolution Adaptive Moving Mesh Hydrodynamic Algorithm. ApJS, 115, 19–34.

Podsiadlowski, P., Ivanova, N., Justham, S., & Rappaport, S. (2010). Explosive common-envelope ejection: implications for gamma-ray bursts and low-mass black-hole binaries. MNRAS, 406(2), 840–847.

Podsiadlowski, P., Rappaport, S., & Pfahl, E. D. (2002). Evolutionary Sequences for Low- and Intermediate-Mass X-Ray Binaries. ApJ, 565(2), 1107–1133.

Powell, K. G., Roe, P. L., Linde, T. J., Gombosi, T. I., & De Zeeuw, D. L. (1999). A Solution-Adaptive Upwind Scheme for Ideal Magnetohydrodynamics. Journal of Computational Physics, 154(2), 284–309.

Prust, L. J. (2020). Moving and reactive boundary conditions in moving-mesh hydrodynamics. MNRAS, 494(4), 4616–4626.

Prust, L. J., & Chang, P. (2019). Common envelope evolution on a moving mesh. MNRAS, 486(4), 5809–5818.

Rasio, F. A., & Livio, M. (1996). On the Formation and Evolution of Common Envelope Systems. ApJ, 471, 366.

Retter, A., & Marom, A. (2003). A model of an expanding giant that swallowed planets for the eruption of V838 Monocerotis. MNRAS, 345(2), L25–L28.

Ricker, P. M., & Taam, R. E. (2012). An AMR Study of the Common-envelope Phase of Binary Evolution. ApJ, 746, 74.

Rodriguez, C. L., Haster, C.-J., Chatterjee, S., Kalogera, V., & Rasio, F. A. (2016). Dynamical Formation of the GW150914 Binary Black Hole. ApJ, 824, L8.

Rosswog, S. (2009). Astrophysical smooth particle hydrodynamics. , 53(4-6), 78–104.

Rosswog, S., & Price, D. (2007). MAGMA: a three-dimensional, Lagrangian magnetohydrodynamics code for merger applications. MNRAS, 379(3), 915–931.

Roxburgh, I. W. (1967). Origin of Planetary Nebulae. Nature, 215(5103), 838.

Rycroft, C. H. (2009). VORO++: A three-dimensional Voronoi cell library in C++. Chaos, 19(4), 041111.

Sabach, E., Hillel, S., Schreier, R., & Soker, N. (2017). Energy transport by convection in the common envelope evolution. *MNRAS*, *472*, 4361–4367.

Saitoh, T. R., & Makino, J. (2009). A Necessary Condition for Individual Time Steps in SPH Simulations. *ApJ*, *697*, L99–L102.

Sandquist, E. L., Taam, R. E., & Burkert, A. (2000). On the Formation of Helium Double Degenerate Stars and Pre-Cataclysmic Variables. *ApJ*, *533*, 984–997.

Sandquist, E. L., Taam, R. E., Chen, X., Bodenheimer, P., & Burkert, A. (1998). Double Core Evolution. X. Through the Envelope Ejection Phase. *ApJ*, *500*, 909–922.

Schoenberg, I. (1969). Cardinal interpolation and spline functions. *Journal of Approximation Theory*, *2*(2), 167–206.

Shiber, S., & Soker, N. (2018). Simulating a binary system that experiences the grazing envelope evolution. *MNRAS*, *477*, 2584–2598.

Soker, N. (1994). Influence of wide binaries on the structures of planetary nebulae. *MNRAS*, *270*, 774–780.

Soker, N. (1996). What Planetary Nebulae Can Tell Us about Planetary Systems. *ApJ*, *460*, L53.

Soker, N. (2017). Energizing the last phase of common envelope removal. *ArXiv e-prints*.

Soker, N., Grichener, A., & Sabach, E. (2018). Radiating the hydrogen recombination energy during common envelope evolution. *ArXiv e-prints*, (p. arXiv:1805.08543).

Spaulding, A., & Chang, P. (2020). The Effect of Impact Parameter on Tidal Disruption Events. *arXiv e-prints*, (p. arXiv:2010.07318).

Springel, V. (2010a). E pur si muove: Galilean-invariant cosmological hydrodynamical simulations on a moving mesh. *MNRAS*, *401*, 791–851.

Springel, V. (2010b). Smoothed Particle Hydrodynamics in Astrophysics. *ARAA*, *48*, 391–430.

Springel, V., Yoshida, N., & White, S. D. M. (2001). GADGET: a code for collisionless and gasdynamical cosmological simulations. *New Ast.*, *6*(2), 79–117.

Stadel, J. G. (2001). *Cosmological N-body simulations and their analysis*. Ph.D. thesis, UNIVERSITY OF WASHINGTON.

Steinberg, E., Yalinewich, A., & Sari, R. (2016). Grid noise in moving mesh codes: fixing the volume inconsistency problem. *MNRAS*, *459*, 1596–1601.

Stone, J. M., Gardiner, T. A., Teuben, P., Hawley, J. F., & Simon, J. B. (2008). Athena: A New Code for Astrophysical MHD. *ApJS*, *178*, 137–177.

Stone, N. C., Vasiliev, E., Kesden, M., Rossi, E. M., Perets, H. B., & Amaro-Seoane, P. (2020). Rates of Stellar Tidal Disruption. , *216*(3), 35.

Szölgyén, Á., MacLeod, M., & Loeb, A. (2022). Eccentricity Evolution in Gaseous Dynamical Friction. *arXiv e-prints*, (p. arXiv:2203.01334).

Tauris, T. M., & Dewi, J. D. M. (2001). Research Note On the binding energy parameter of common envelope evolution. Dependency on the definition of the stellar core boundary during spiral-in. *A&A*, *369*, 170–173.

Taylor, G. (1950). The Formation of a Blast Wave by a Very Intense Explosion. I. Theoretical Discussion. *Proceedings of the Royal Society of London Series A*, *201*(1065), 159–174.

Terman, J. L., Taam, R. E., & Hernquist, L. (1994). Double-core evolution. 5: Three-dimensional effects in the merger of a red giant with a dwarf companion. *ApJ*, *422*, 729–736.

Terman, J. L., Taam, R. E., & Hernquist, L. (1995). Double core evolution. 7: The infall of a neutron star through the envelope of its massive star companion. *ApJ*, *445*, 367–376.

Teyssier, R. (2002). Cosmological hydrodynamics with adaptive mesh refinement. A new high resolution code called RAMSES. *A&A*, *385*, 337–364.

Thompson, T. A., Prieto, J. L., Stanek, K. Z., Kistler, M. D., Beacom, J. F., & Kochanek, C. S. (2009). A New Class of Luminous Transients and a First Census of their Massive Stellar Progenitors. *ApJ*, *705*(2), 1364–1384.

Thorne, K. S., & Zytkow, A. N. (1977). Stars with degenerate neutron cores. I. Structure of equilibrium models. *ApJ*, *212*, 832–858.

Toro, E. (2009). *Riemann Solvers and Numerical Methods for Fluid Dynamics: A Practical Introduction*. Springer Berlin Heidelberg.

Toro, E. F., Spruce, M., & Speares, W. (1994). Restoration of the contact surface in the HLL-Riemann solver. *Shock Waves*, *4*(1), 25–34.

Toyouchi, D., Hosokawa, T., Sugimura, K., Nakatani, R., & Kuiper, R. (2019). Super-Eddington accretion of dusty gas on to seed black holes: metallicity-dependent efficiency of mass growth. *MNRAS*, *483*(2), 2031–2043.

Tricco, T. S., & Price, D. J. (2012). Constrained hyperbolic divergence cleaning for smoothed particle magnetohydrodynamics. *Journal of Computational Physics*, *231*(21), 7214–7236.

Turk, M. J., Smith, B. D., Oishi, J. S., Skory, S., Skillman, S. W., Abel, T., & Norman, M. L. (2011). yt: A Multi-code Analysis Toolkit for Astrophysical Simulation Data. The Astrophysical Journal Supplement Series, 192, 9.

Tylenda, R., Hajduk, M., Kamiński, T., Udalski, A., Soszyński, I., Szymański, M. K., Kubiak, M., Pietrzyński, G., Poleski, R., Wyrzykowski, Ł., & Ulaczyk, K. (2011). V1309 Scorpii: merger of a contact binary. A&A, 528, A114.

van den Heuvel, E. P. J. (1976). Late Stages of Close Binary Systems. In P. Eggleton, S. Mitton, & J. Whelan (Eds.) Structure and Evolution of Close Binary Systems, vol. 73, (p. 35).

van Velzen, S. (2018). On the Mass and Luminosity Functions of Tidal Disruption Flares: Rate Suppression due to Black Hole Event Horizons. ApJ, 852(2), 72.

Wadsley, J. W., Stadel, J., & Quinn, T. (2004a). Gasoline: a flexible, parallel implementation of TreeSPH. New Ast., 9, 137–158.

Wadsley, J. W., Stadel, J., & Quinn, T. (2004b). Gasoline: a flexible, parallel implementation of TreeSPH. New Ast., 9, 137–158.

Wan, Y., & Zhong, C. (2019). An ALE-type discrete unified gas kinetic scheme for low-speed continuum and rarefied flow simulations with moving boundaries. arXiv e-prints, (p. arXiv:1906.01813).

Webbink, R. F. (1984). Double white dwarfs as progenitors of R Coronae Borealis stars and Type I supernovae. ApJ, 277, 355–360.

Webbink, R. F. (2008). Common Envelope Evolution Redux. In E. F. Milone, D. A. Leahy, & D. W. Hobill (Eds.) Astrophysics and Space Science Library, vol. 352 of Astrophysics and Space Science Library, (p. 233).

Wetzstein, M., Nelson, A. F., Naab, T., & Burkert, A. (2009). Vine—A Numerical Code for Simulating Astrophysical Systems Using Particles. I. Description of the Physics and the Numerical Methods. ApJS, 184(2), 298–325.

White, C. J., Stone, J. M., & Gammie, C. F. (2016). An Extension of the Athena++ Code Framework for GRMHD Based on Advanced Riemann Solvers and Staggered-mesh Constrained Transport. ApJS, 225(2), 22.

Whitehurst, R. (1995). A free Lagrange method for gas dynamics. MNRAS, 277, 655–680.

Yalinewich, A., Steinberg, E., & Sari, R. (2015). RICH: Open-source Hydrodynamic Simulation on a Moving Voronoi Mesh. ApJS, 216, 35.

Yarza, R., Razo Lopez, N., Murguia-Berthier, A., Everson, R. W., Antoni, A., MacLeod, M., Soares-Furtado, M., Lee, D., & Ramirez-Ruiz, E. (2022). Hydrodynamics and survivability during post-main-sequence planetary engulfment. arXiv e-prints, (p. arXiv:2203.11227).

Zhu, C., Chang, P., van Kerkwijk, M. H., & Wadsley, J. (2013). A Parameter-space Study of Carbon-Oxygen White Dwarf Mergers. ApJ, 767, 164.

Zorotovic, M., Schreiber, M. R., Gänsicke, B. T., & Nebot Gómez-Morán, A. (2010). Post-common-envelope binaries from SDSS. IX: Constraining the common-envelope efficiency. A&A, 520, A86.